NASA CONTRACTOR REPORT

NASA CR-2180

NASA CR-2180

WIND TUNNEL SIMULATION OF FULL SCALE VORTICES

by James B. Rorke and Robert C. Moffitt

Prepared by
SIKORSKY AIRCRAFT DIVISION
UNITED AIRCRAFT CORPORATION
Stratford, Conn. 06602
for Langley Research Center

NATIONAL AERONAUTICS AND SPACE ADMINISTRATION • WASHINGTON, D. C. • MARCH 1973

1. Report No.	2. Government Accession No.	3. Recipient's Catalog No.
NASA CR-2180		

4. Title and Subtitle	5. Report Date
WIND TUNNEL SIMULATION OF FULL SCALE VORTICES	March 1973
	6. Performing Organization Code

7. Author(s)	8. Performing Organization Report No.
James B. Rorke and Robert C. Moffitt	

9. Performing Organization Name and Address	10. Work Unit No.
Sikorsky Aircraft Division of United Aircraft Corporation Stratford, CT 06602	11. Contract or Grant No. NAS1-10446

12. Sponsoring Agency Name and Address	13. Type of Report and Period Covered
National Aeronautics and Space Administration Washington, D.C. 20546	Contractor Report
	14. Sponsoring Agency Code

15. Supplementary Notes

16. Abstract

An experimental investigation has been conducted to determine the important scaling parameters for the flow in the core region of a vortex generated by a rectangular wing tip. The effect of an unconvnetional planform, the ogee tip, on the tip vortex is also determined. For rectangular planform wings, the measured vortex core diameter to chord ratios, peak tangential velocity ratios, and axial velocity ratios are shown to be functions only of wing lift coefficient and elapsed time from vortex formation, and appear to be independent of both Mach number and Reynolds number. The peak tangential velocities in the diffuse vortex generated by the ogee tip are only 25 percent of those in the vortex generated by the rectangular wing.

17. Key Words (Suggested by Author(s))	18. Distribution Statement
Tip vortex Tip shape Vortex scaling Vortex flow	Unclassified - Unlimited

19. Security Classif. (of this report)	20. Security Classif. (of this page)	21. No. of Pages	22. Price*
Unclassified	Unclassified	114	$3.00

*For sale by the National Technical Information Service, Springfield, Virginia 22151

TABLE OF CONTENTS

WIND TUNNEL SIMULATION OF FULL SCALE VORTICES

By James B. Rorke, and Robert C. Moffitt
Sikorsky Aircraft Division
United Aircraft Corporation
Stratford, Connecticut

SUMMARY

An experimental investigation has been conducted to determine the important scaling parameters for the flow in the core region of a vortex generated by a rectangular wing tip. The effect of an unconventional planform, the ogee tip, on the tip vortex is also determined. Data were measured for wing pitch angles of 6 and 9 degrees at Mach numbers of 0.2, 0.5 and 0.6 for Reynolds numbers ranging from 4.4×10^5 to 7.0×10^6 using a triaxial hot wire probe. The probe was located at 2 and 5 chordlengths downstream from the trailing edge of the 10.8 cm (4.25 inch) and 66.1 cm (26.0 inch) chord wings. For rectangular planform wings, the measured vortex core diameter to chord ratios, peak tangential velocity ratios, and axial velocity ratios are shown to be functions only of wing lift coefficient and elapsed time from vortex formation, and appear to be independent of both Mach number and Reynolds number. The peak tangential velocities in the diffuse vortex generated by the ogee tip are only 25 percent of those in the vortex generated by the rectangular wing.

INTRODUCTION

The importance of the vortex system in the near wake of a rotor or propeller to the performance, dynamics, and acoustic characteristics of that rotor or propeller is well established.

In hover, the close proximity of the tip vortex trailing from the preceding rotor blade causes extremely high local induced angles of attack near the tip of subsequent blades on the rotor, resulting in significant reductions in rotor efficiency [1,2,3]. In forward flight, both rotor performance and airloads are significantly affected by blade-vortex interactions. Trailing tip vortices often impinge directly on the rotor blades causing high vibratory loads[4]. The vortex system also has a large effect on the perceived noise level of the rotor system. Local flow separation, resulting from the large angle of attack changes which occur when a blade intercepts a trailing vortex filament, has been identified as a large contributor to the overall noise level of current generation helicopter rotors. The large angle of attack fluctuations which are necessary to induce blade slap can, among other things, result from a blade operating in the flow field of the trailing vortex if the distance separating the blade and the vortex core is not steady with time[5].

Analytic methods, which have been developed to account for the effect of the trailing vortex on hover performance[1,2,3], forward flight performance[6,7], blade airloads[6,7], and perceived noise levels[5], all require a definition of the flow field within the core of the vortex. In most methods, contact between the vortex core and the blade or between the cores of two vortices occurs regularly. Lack of an accurate model of the vortex has been an important obstacle to the accuracy and usefulness of many of these analyses.

Trailing tip vortices of fixed wing aircraft have received increased attention with the entering of jumbo jets into commercial service. The turbulence created by the vorticity in the wakes of these large jets represents a severe hazard in the air corridors surrounding large airports. An accurate model of the vortex is a prerequisite to an effective solution of this problem.

A large quantity of experimental data defining the structure of trailing vortices has been obtained at low Mach numbers and Reynolds numbers. Generally, these investigations have focused on Mach numbers below 0.2 and Reynolds numbers less than 5 million. Full scale rotors normally encounter tip Mach numbers above 0.5 and Reynolds numbers in excess of 10 million. The existing small scale, low Mach number data could not be confidently extrapolated to full scale operating conditions without further experimentation to determine vortex structure trends with Mach number and Reynolds number.

The present experimental program was conducted for two basic reasons: to measure the flow field in the core of a vortex at Mach and Reynolds numbers comparable to those at the tip of a full scale helicopter main rotor blade; and to determine the degree of applicability of the large quantity of previously acquired small scale vortex flow field data to the full scale situation. The test program was conducted during the summer of 1971 in the 8-foot octagonal wind tunnel at the United Aircraft Research Laboratories, East Hartford, Connecticut. Models with chords of 10.8 and 66.1 centimeters (4.25 and 26.0 inches) were tested at Mach numbers from 0.20 to 0.60, yielding Reynolds number and Mach number ranges which span the gap between previously available data and the operating conditions at the tip of a full scale rotor blade. Velocity distributions through the core of the vortex were measured using a triaxial hot wire probe at downstream locations of 2 and 5 chordlengths from the model trailing edge. Data were also measured for the ogee tip, a wing tip designed to reduce the high tangential velocities generally found in the core of a trailing vortex.

SYMBOLS

A mean axial velocity parameter, $\int_{-.2c}^{.2c} v_z \, dr / .4c(\bar{v}_z)$ $(r = \pm .5c)$

b semispan, meters

C velocity signal scale factor, meters/volt-sec.

C_D drag coefficient, $D/q_\infty S$

C_L	lift coefficient, $L/q_\infty S$
C_{pu}	upper surface pressure coefficient, $(p_s - p_\infty) / q_\infty$
c	chord, meters
D	drag force, newtons
d_o	diameter of vortex core, meters
h	hot wire overheat ratio, R_W/R_E
I	electrical heating current supplied to wire, amps
$\vec{i}, \vec{j}, \vec{k}$	wind tunnel cartesian coordinate system unit vectors
$\vec{i}', \vec{j}', \vec{k}'$	probe cartesian coordinate system unit vectors
L	lift force, newtons
M	Mach number
p_s	local static pressure, newtons/meter^2
p_∞	free stream static pressure, newtons/meters^2
q_∞	free stream dynamic pressure, newtons/meters^2
R_E	equilibrium wire resistance, ohms
R_W	heated wire resistance, ohms
R_N	Reynolds number, vc/ν
R_O	wire resistance at melting point of ice, ohms
r	radial distance from center of vortex, meters
S	projected wing lifting area, meters^2
T_o	stagnation temperature, deg Kelvin
t	elapsed time from vortex formation at the wing quarter chord, $(Z + .75c) / v_\infty$, sec
V_x, V_y, V_z	voltage output from x, y, and z wire linearizers respectively, volts
v	velocities, general, meters/sec

v_X velocity component in X direction (normal to wing) in wind tunnel rectangular cartesian coordinate system, meters/sec

v_Y velocity component in Y direction (spanwise) in wind tunnel rectangular cartesian coordinate system, meters/sec

v_Z axial velocity component in wind tunnel rectangular cartesian coordinate system, meters/sec

$(\bar{v}_Z)_{(r=\pm .5c)}$ average of axial velocities measured at.5c from the center of the vortex on each side of the core.

v_x, v_y, v_z velocity component parallel to probe x, y and z wire respectively, meters/sec

v_θ tangential velocity, meters/sec

v_∞ free stream velocity, meters/sec

v_{uX}, v_{uY}, v_{uZ} uncorrected velocity component in X, Y, and Z direction respectively in wind tunnel coordinate system, meters/sec

v_{nx}, v_{ny}, v_{nz} velocity component normal to probe x, y, and z wire respectively, meters/sec

v_{ux}, v_{uy}, v_{uz} uncorrected velocity component in x, y, and z direction respectively, in probe coordinate system, meters/sec

$v_{unx}, v_{uny}, v_{unz}$ uncorrected velocity component normal to the x, y, and z direction respectively in probe coordinate system, meters/sec

X ordinate normal to wing span

Y ordinate parallel to wing span

Z streamwise ordinate, measured from wing trailing edge

x,y,z ordinates parallel to probe x, y, and z wires respectively

α_o wire temperature coefficients of resistivity, deg C

Γ circulation strength, meters^2/ sec

Θ wing geometric angle of attack, deg

ν kinematic viscosity, meters^2/sec

LIST OF ILLUSTRATIONS

Vortex Velocity Data - Large Rectangular Tip

Vortex Velocity Data - Small Rectangular Tip

Vortex Velocity Data - Ogee Tip

Figure	Mach Number	Pitch Angle	Traverse Direction	Chord Length Downstream	Page
75	0.5	6 deg.	Parallel	2.0	105
76	0.5	6 deg.	Normal	5.0	106
77	0.5	6 deg.	Parallel	5.0	107
78	0.5	9 deg.	Normal	2.0	108
79	0.5	9 deg.	Parallel	2.0	109
80	0.5	9 deg.	Normal	5.0	110
81	0.5	9 deg.	Parallel	5.0	111
82	0.6	9 deg.	Parallel	5.0	112

WING MODELS AND INSTRUMENTATION

High and Low Reynolds Number Models

The desired Reynolds number variation was acquired by fabricating two rectangular aluminum fixed wing models with chords of 66.1 and 10.8 centimeters (26.0 and 4.25 inches) as shown in Figures 1 and 2. Approximately equal aerodynamic efficiencies were obtained for each wing by holding the semispan aspect ratio constant at 2.1:1.0. This value was chosen to ensure that the curve of lift vs. spanwise distance from the wing tip would become asymptotic on the wing surface before the point of interaction between the boundary layers of the model and ground plane at the model base.

The large model was instrumented with 52 static pressure taps to acquire an indication of spanwise lift distribution. The 26 pressure orifices on either side of the blade were located at the 1/4 chord position and spaced spanwise at 5.1 centimeter (2.0 inch) intervals. The large model was a segment of a CH-53A helicopter rotor blade section with a revolved airfoil tip cap. The small model consisted of a segment of a model rotor blade, with a NACA 0012 airfoil and a revolved airfoil tip cap. The airfoil on the large model was a Sikorsky-designed 11 percent thick section, but its aerodynamic characteristics were essentially identical to those of the NACA 0012. Both models were positioned in the wind tunnel with the wing tip as close to the test section centerline as possible as shown in Figure 3. The small 10.8 cm (4.25 inch) chord model was mounted on a 76.2 cm (30 inch) diameter (seven chordlengths) ground plane to ensure two dimensionality of the flow at the model base. The wing models were mounted as far upstream in the test section as possible while keeping within the limits imposed by the constant aerodynamic flow characteristics of the test section. Model location remained fixed for the duration of the vortex test and the traverse mechanism was relocated to the 2 and 5 chordlength downstream locations as required by the test plan.

Ogee Tip Model

The ogee tip wing model, shown in Figures 1 and 3, was fabricated with a base chord of 66.1 cm (26.0 inches) and a wing semispan of 187 cm (73.9 inches), giving a span to chord ratio of 2.8:1.0. Wing area and airfoil section

were identical to those of the large rectangular wing. The basic wing thickness to chord ratio and airfoil section was maintained over the ogee tip to a point 28 cm (11 inches) from the extreme tip. Beyond this point the thickness was held constant, which resulted in a gradual transition to a more elliptical airfoil section at the outboard end, as shown in Figure 1.

The ogee shape evolved from exploratory, small scale, smoke tunnel tests and wake Schlieren studies. The shape is based upon a concept of a two stage tip vortex formation mechanism, which results from the three-dimensionality of the flow field[8]. The primary vortex is formed along the streamwise edge of a rectangular wing tip[9] - much like a delta wing leading edge vortex [10,11]. This separation vortex forms an intense core and, as it passes off the tip trailing edge, the wing shed vortex sheet is entrained and concentrated into a combined tip vortex system. The separation vortex mechanism results in a local lift augmentation in the tip region [11]; however, it is not essential to the primary lifting system [8]. The ogee tip shape is designed to eliminate the separation vortex. This is achieved by cutting back the tip streamwise edge, starting at the leading edge, at an angle sufficient to assure that the local flow swirl angle cannot produce a reattachment of the flow coming from beneath the tip on the upper surface. The cut-back angle gradually decreases toward the wing trailing edge, due to a drop-off in differential pressure and the associated swirl angle. The tip edge is faired smoothly into the wing trailing edge to avoid a sharp discontinuity in local flow.

In the small scale flow visualization tests, the ogee shape did appear to eliminate the concentrated separation vortex mechanism, and also appeared to significantly reduce the concentration of the overall tip vortex system. The present tests were conducted to determine the influence of Mach number and Reynolds number on the small scale observations, and to obtain some quantitative full-scale data on the ogee tip trailing vortex system and on the lift to drag ratio characteristics.

Traverse Mechanism

The triaxial hot wire probe was positioned in the wind tunnel by a traverse mechanism which was located approximately on the wind tunnel test section centerline. This mechanism, shown in Figure 4, was capable of positioning the probe within an 81 x 81 cm (32 x 32 inch) square area in the X-Y plane with a demonstrated repeatability of $\pm$ .03 cm ($\pm$ .01 inches). Traversing speed was approximately 2.5 cm/sec (1 in/sec), but varied somewhat with wind tunnel airspeed. Lower traversing speeds were desirable at certain test conditions where the physical size of the vortex core was extremely small. This requirement was predicated on the response characteristics of the plotter used to record velocity data rather than the response characteristics of the hot wire equipment, and was accomplished by rapid intermittent operation of the traverse mechanism drive motors. Repeatability of vortex velocity distribution data for these cases is excellent, as shown in Figure 6.

The mechanism was driven by two ½ horsepower electric motors which were mounted outside of the wind tunnel test section and operated remotely from

the wind tunnel control room. Probe position was monitored by two potentiometers geared to the drive mechanism. The output voltage signals from these potentiometers were wired directly to the plotter used to record voltages proportional to on-line axial and tangential velocities as a function of probe position in the vortex. The on-line data for both axial and tangential velocities were recorded simultaneously as a function of probe position utilizing a plotter with two recording pens.

Instrumentation

The triaxial hot wire probe was selected as the flow measurement device for this study based on the following attributes:

1. Rapid response characteristics allow continuous acquisition of data as the probe is swept through the flow field.

2. All three components of velocity can be measured directly with one probe of relatively small physical dimensions.

3. Axial velocity variations which occur through the core of the vortex do not affect the instrument calibration or measurement of tangential velocity.

4. The hot wire probe can be accurately calibrated over a wide Mach number range.

The triaxial hot wire probe contains three orthogonal wire elements. Each element has a sensitive wire length of approximately 1.25 mm and a diameter of 5 microns. The sensitive wire length is limited by gold plating which covers the end of the wire support prongs and a small segment of the wire end. This plating reduces interference among the three wires, and between the support prongs and the wire, which is sometimes experienced in the skewed flow field.

The probe wires were heated by three constant temperature anemometers. The voltages required to maintain the constant temperatures of the wires, which are a measure of the velocity normal to each wire, were passed through linearizers to a specialized analog computer. This computing circuit transferred the linearized voltages for the three wires from the probe coordinate system, x, y, z, to the wind tunnel coordinate system, X, Y, Z. These final voltages, along with the position voltage from the traverse mechanism potentiometers, were then used to drive a plotter. A schematic diagram of this instrumentation is shown as Figure 5.

As the probe was traversed through the center of each vortex, an on-line plot was obtained of linearized voltages proportional to tangential and axial velocity in the vortex vs. probe position in the wind tunnel. The plotted data was continuously monitored for repeatability and significant trending.

Vortex Location and Measurement

Prior to acquiring data for a spanwise traverse, the tip vortex was located by moving the probe parallel to the blade span, or in the Y direction, at a predetermined X location. Normal and axial velocities (v_X and v_Z) vs. probe location (Y) were recorded with the on-line plotter and the X location was noted as displayed on a digital voltmeter. The process was repeated for several X locations until the X location for which the peak v_X was a maximum was determined. A traverse in the spanwise (Y) direction at this X position then passed the probe directly through the center of the vortex. Due to the precision of the traverse mechanism, increments on the X axis as small as 0.13 centimeters (0.05 inches) were obtained. Smaller increments were achieved in several cases, but the effect on the magnitude of the peak velocity was negligible. Using this procedure, the center of any vortex could be located within 1 or 2 minutes of time to an accuracy of $\pm$ 0.13 cm ($\pm$ 0.05 inches).

Having located a line passing through the vortex center, between two and six traverses were made and the probe was stopped for a period of time at one or two points near the vortex core.

REDUCTION AND ANALYSIS OF DATA

Vortex Velocity Data Corrections

The on-line vortex velocity profiles recorded directly from the anemometer instrumentation required a number of analytic corrections due to the operating characteristics of a hot wire probe in compressible flow. Basically, a hot wire anemometer measures the rate of convective heat loss from the heated sensor element, the wire, to the surrounding fluid. This rate of heat transfer depends on the geometric shape and temperature of the sensor, and the fluid velocity, temperature, pressure, and thermal properties. The on-line velocity data obtained in this study were corrected for all of these parameters. The recorded on-line data were also corrected for nonlinearity remaining in the probe signal after it was corrected by the linearizers and axis transfer computing circuits which were used during the test.

A semi-empirical heat transfer equation[12], which has been shown to be valid over a free stream Mach number range from 0.05 to 1.9, was used as the basis for the correction equations applied in this study. Partial differentiation of the velocity term in this equation with respect to the stagnation temperature, static pressure, and Mach number respectively yielded error expressions. These were used to correct the velocity data for differences between the ambient test conditions and the probe calibration conditions. Derivations for these error expressions are presented in Appendix A.

The magnitude of the radial static pressure gradient within each surveyed vortex structure was evaluated by integrating the radial component of the Navier-Stokes equation with an assumed constant density. The validity of this approach for estimating swirl induced pressure distributions in axisymmetric flow has been demonstrated [13,14]. No corrections were applied for

stagnation temperature changes in the vortex since resistance thermometer traverses through several vortex flow fields indicated only insignificant stagnation temperature variations.

A basic 10 point calibration of normal velocity versus wire voltage was performed in the tunnel for each wire to establish the reference calibration at known static pressures and stagnation temperatures.

The linearization corrections were required since the on-line axis transfer circuits assume that the voltage inputs from the three sensor wires are linear and identically matched. In practice, perfect signal linearization and matching is impossible and small errors in the degree of approximation can cause significant errors in the indicated vortex velocities. A procedure was incorporated in the data reduction analysis which calculated the voltage sensed by each wire from the on-line velocity profiles, corrected the velocity components normal to each wire for the known nonlinearities, and then reconstructed the vortex velocities. This procedure is also detailed in Appendix A.

The complete data analysis routine was programmed for a UNIVAC 1108 computer. The program input for each case consisted of the digitized on-line voltages proportional to vortex velocities and the pertinent probe calibration points, calibration conditions, and ambient data point conditions. The program output presents a tabular listing of the vortex velocity, vorticity, and circulation distributions in addition to plots of the corrected velocity distributions.

Repeatability of Velocity Measurements

At each test condition, data were recorded for as many as six and at least two traverses through the vortex. These continuous traverses were interrupted periodically to hold the probe at a fixed position in the vortex for up to a full minute. The time required to record data for one traverse direction at one test condition generally varied between 5 and 10 minutes. For each test condition, data for all repeat traverses were identical. With the probe stopped at any position in the vortex, including the point for maximum tangential velocity, no variation of recorded velocity with time was detected. Two typical on-line plots which illustrate this repeatability are presented as Figure 6.

When data for one condition were recorded on separate days with different probes, the reduced velocity data were again in agreement. Due to differences in tunnel temperature, barometric pressure and probe calibrations, this repeatability is not apparent in the on-line data for those conditions, but plots of the corrected, reduced data are in close agreement as shown in Figure 7.

The repeatability of the data obtained gives a high degree of confidence in the measured vortex core diameters and peak velocities.

Symmetry of Velocity Profiles

Tangential velocity distributions measured during traverses parallel to the wing span as shown in Figure 8 are more symmetrical about the center of the vortex ($v_\theta = 0$) than those of Figure 9 which were measured during normal traverses. The same trend is present in the data presented by Chigier and Corsiglia[11]. The dissymmetry is caused by the presence of the inboard vortex sheet which merges with the rolled up tip vortex as measured by McCormick and Tangler[16] and illustrated in the following sketch.

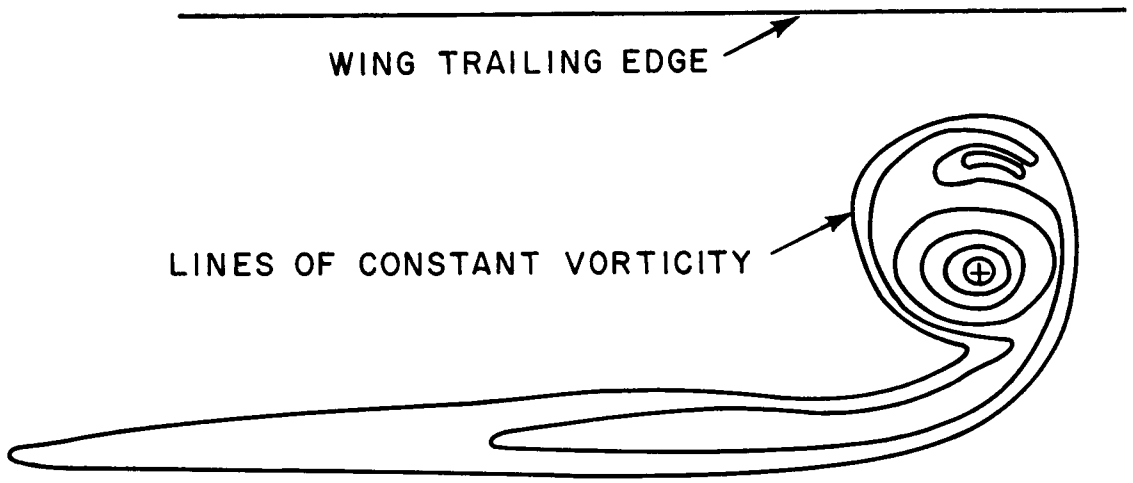

The relative concentration of vorticity on the lower portion of the vortex results in higher velocities in that region than at a corresponding point in the upper portion of the vortex. This dissymmetry becomes evident in examining the data recorded during traverses where the probe was passed through this region. During a spanwise traverse, the probe does not generally pass through the region of the tip vortex - inboard sheet junction, and the measured tangential velocity distribution is more symmetric (Figure 8a).

As the vortex ages however, even velocity distributions measured during spanwise traverses tend to lose their symmetry. This can be seen by tracing the decreasing symmetry of the representative data plotted in Figures 8a, b, c, and d in that order. This trend suggests a rollup of the tip vortex and inboard sheet which progresses as a function of downstream time, not as a function of Mach number, Reynolds number, wing model, or downstream location.

Previous investigators[11] have shown that the tip vortex forms approximately at the wing quarter chord. The vortex age, or elapsed time from formation of the vortex, t, is therefore defined as the time required for an air particle to travel at the free stream velocity, v_∞, from the wing quarter chord to the downstream location at which the vortex was surveyed. When applying the trends developed in the present study, it should be recalled that all data were acquired at locations downstream of the wing trailing edge. These trends are not believed to be valid for conditions upstream of the trailing edge.

Vortex Core Size

The diameter of the vortex core is defined as the distance between the points at which the tangential velocity is a maximum on either side of the core.

Since vortex structure data for each of the two models were measured at three Mach numbers, two geometric angles of attack, and two downstream locations, it was possible to examine the effect of all of these parameters on the vortex structure. Based on this data, it has been determined that Reynolds number, Mach number, and downstream distance have no significant independent effect on vortex core size. For a fixed wing tip geometry, the diameter of the vortex core divided by the wing chord (d_o/c) is a function only of the wing lift coefficient and the elapsed time from the formation of the vortex. The vortex is assumed to have been formed at the wing quarter chord as indicated by the data of Reference 11.

Figure 10 illustrates the trends of core size versus time that are drawn from the present data. The data points plotted, which represent all of the test conditions of this study for the rectangular wing models, group into two distinct trends representing the two angles of attack. At constant angle of attack, a firm correlation between nondimensional core size and time is established independent of Mach number, Reynolds number or model size. The segment of the curve between 8 and 11 milliseconds includes data recorded 5 chordlengths downstream of the small model at Mach 0.20 and 2 chordlengths downstream of the large 66.1 cm (26 inch) chord model at Mach 0.50 and 0.60. Except for the previously noted angle of attack trend, all the points, which were measured at the same time following vortex formation, are nearly coincident. Figure 11 presents the tangential velocity distributions for four data points in this elapsed time region at widely different test conditions. The velocity distributions are nearly identical at each angle of attack.

The accuracy of the combined system, including the traverse mechanism, on-line plotter, and the data reduction system, results in an estimated precision of the core size measurement of $\pm$ 0.13 cm ($\pm$ 0.05 inches).This yields a d_o/c precision of approximately .002 for the large model and .010 for the small model which explains the larger scatter band of the data at the lower values of elapsed time.

Figure 10 shows that the core expands for a very short time following formation of the vortex and then contracts as a logarithmic function of time. At 9 degrees angle of attack, the core size decreases from 9.5 to 3.0 percent of the wing chord between 3 and 54 milliseconds after formation of the vortex. At 6 degrees, the core contracts from 6.0 to 2.5 percent of the wing chord over the same interval. It is expected that, at higher values of time than those attained in this study, a re-expansion of the core would occur and eventually lead to vortex dissipation.

The core diameter of the vortex formed by the ogee tip is from 2 to 5 times larger than those of the rectangular wing sections. Examination of Figure 15 reveals that the core of this vortex is not well defined and a

quantitative discussion of core size trends from these vortices would not be meaningful.

Tangential Velocity

As with core size, the ratio of maximum tangential velocity to free stream velocity was found to vary only as a function of time from vortex formation. The trend is not directly dependent on Mach number, Reynolds number, or model size.

The average maximum tangential velocity is defined as the average of the maximum tangential velocities measured on each side of the vortex core. The purpose of using this averaged value is to eliminate errors in defining the point of zero velocity on the on-line data plots which could have been introduced during calibration of equipment or data reduction. In the remainder of this report the term "maximum tangential velocity" should be considered to be synonymous with the term "averaged maximum tangential velocity".

Figure 12 shows the derived trend of maximum tangential velocity ratio as a logarithmic function of time elapsed from vortex formation. The peak velocities increase until they reach a maximum 5 to 10 milliseconds following formation and then begin to decrease slowly as the core contracts. The resulting logarithmic function is similar to the core size versus time function, but with a time lag between the peak core diameter and the maximum velocity points.

As discussed previously, tangential velocities measured during traverses normal to the wing span are influenced to a considerable extent by the trailing vortex sheet, while traverses parallel to the wing span are more representative of an isolated tip vortex. For this reason only data obtained during spanwise traverses are shown in Figure 12. Inclusion of data from normal traverses does not change the trend shown, but increases the scatter band.

The dramatic effect of the ogee tip on peak tangential velocities is illustrated by Figure 12 which shows that these velocities are reduced below those present in the vortex of a rectangular wing by a factor of 4. The data show that significantly more time is required for the tip vortex formed by the ogee tip to completely roll up and develop its maximum tangential velocity, but this is to be expected as a result of the differences in the spanwise load distributions. It appears that the maximum tangential velocity of the ogee tip has been developed at about 50. milliseconds following vortex formation versus about 5. milliseconds for the rectangular tip.

Axial Velocity

Significant axial velocity variation within the vortex core is evident in all the surveyed structures for rectangular planform wings. In general, the axial velocity profiles consist of a relatively flat region, which is slightly less than the free stream velocity at vortex radial distances greater than 20 percent of the model chord, and a sharp gradient region in the vicinity of the core.

The mean axial velocity parameter, A, represents the averaged axial velocity over a 0.20 chordlength distance on each side of the center of the core divided by the average velocity at the ends of the total traverse sweep. The data plotted in Figure 13 shows a consistent increase of axial velocity with increasing time, with no discernable separation between the data acquired with the high and low Reynolds number models. For very low elapsed time values (less than 4 milliseconds), the averaged axial velocities are slightly below those far outside the core. At the highest times evaluated, (54 milliseconds), mean axial velocity excesses as large as 10 percent were recorded at a wing angle of 9 degrees. The velocity excesses measured at the 9 degree angle of attack are larger than those recorded at the 6 degree test condition.

The growth of the axial velocity excess with time is probably related to the vortex roll-up process. Similar trends were noted by Chigier and Corsiglia[11]. The diffuse tip vortex of the ogee tip did not show any significant axial velocity trends.

Circulation Strength

The circulation strength of a vortex is classically defined as the area integral of the vorticity over the limits of the flow field. In practice, the complete area of vorticity is rarely surveyed. The accuracy of the circulation calculation at large radii from the vortex center is questionable due to small errors in the velocity measurement being magnified by the large radial distance in the calculation. As a result, circulation strengths estimated from experimental vortex velocity distributions are approximate. The circulation strengths were calculated from the present data for each test condition by averaging the integrated vorticity for the normal and spanwise traverse at each test condition.

Figure 14 presents the calculated circulation strengths divided by model chord (Γ/c) as a function of Mach number for the large and small models at 6 and 9 degrees pitch. Although an increase in Γ/c for the higher pitch angle is evident, any trends with model scale, traverse direction, or downstream position are either insignificant or within the estimated $\pm$ 10 percent accuracy of the calculation.

Similar calculations were performed for the ogee tip. Because the tip vortex of the ogee tip is so diffused, the low velocities at large distances from the vortex center introduce a high degree of uncertainty as discussed above. For this reason, calculated circulation strengths are not presented for the ogee tip.

Effect of Ogee Tip

The vortex trailing from the ogee tip is extremely diffuse at all conditions surveyed. Figure 15 shows comparisons of tangential velocity distributions through the core of the vortices generated by both the large rectangular and the ogee tips. The peak velocities in the ogee tip vortex are, in general, only 25 percent of those in the vortex of the large rectangular tip

and, even outside of the larger core of the ogee tip, tangential velocities in the wake of the ogee tip are lower. Figure 12 shows that this trend holds for all test conditions and that a much longer time is required for the ogee tip vortex to develop. It appears that the peak tangential velocities in the core have been fully developed after 54 milliseconds compared to 6 milliseconds for the rectangular planform.

The core diameter of the ogee tip vortex is substantially larger than that of the tip vortex of the rectangular planform wing and is not well defined. The formation process of this vortex is more similar to the roll up of a trailing vortex sheet than the formation of a conventional tip vortex. This suggests that the elimination of the separation vortex mechanism, which was the goal of the ogee tip shape design, was substantially achieved. The concentration mechanism associated with the interaction of the intense core of the separation vortex and the trailing vortex sheet is no longer present. This allows a more gradual and diffuse roll up of the tip vortex system.

Secondary factors contributing to the diffusion of the ogee tip vortex core are believed to be (1) the probable reduction in the spanwise gradient of the lift distribution in the tip region and (2) the likelihood of local separated flow in the region of the extreme tip section, where the thickness to chord ratio dictates a transition to an elliptical airfoil section, which introduces turbulent flow into the vortex core region.

Force Measurements

Lift, drag and pitching moment data were acquired by mounting each wing model on the wind tunnel yaw balance in a configuration identical to that used during the vortex velocity measurements. Force data were acquired for all conditions at which the tip vortices were surveyed. The aerodynamic force coefficients are presented in Figures 16 through 23 as a function of pitch angle for the three models.

Lift to drag ratio as a function of lift coefficient are presented for the large rectangular tip and the ogee tip in Figure 24. At constant lift coefficient, L/D of the ogee tip is always higher than that of the rectangular tip. At constant angle of attack, the drag coefficient of the ogee tip is always higher than that of the rectangular wing with the difference becoming larger as the pitch angle increases. It should also be noted that, since both the ogee tip and the rectangular tip have the same planform area, the aspect ratio of the ogee tip is higher.

Correcting the L/D data for the difference in aspect ratio indicated that, below stall onset, the ogee tip wing had a slight (approximately 5 percent) improvement in efficiency over the rectangular wing.

Large Rectangular Tip Pressure Measurements

The spanwise lift profiles of the large rectangular tip, as indicated by the measured spanwise distribution of pressure coefficients at the upper surface quarter chord line, are presented in Figures 25 through 27 for the five pitch angle - Mach number combinations at which vortex survey data were obtained. It is apparent from the data that the desired asymptotic lift behavior at the model base was never achieved at 9.0 deg. pitch and only partially realized at 6 deg. pitch for Mach numbers of 0.2 and 0.5. The decrease in lift at the base of the wing is probably a result of flow separation due to insufficient sealing at the wing base - tunnel floor junction. This is based on the following observations: (1) the area affected by the lift interference is fairly independent of Mach number at 9.0 deg. pitch, (2) the magnitude of the lift loss is a strong function of the model pitch angle and (3), the lift loss initiates at the distance of 36 cm (14 in.) from the wing base, which is far outside the normal region of boundary layer interference.

If it is conservatively assumed that ½ of the area affected by the lift disturbance is non-functional, a corrected effective aspect ratio of 1.8 is calculated. Also, since the disturbance was limited to the inner 25 % of the wing semi-span, the resulting effect on the rolled up tip vortex is probably small. It should be noted that, based on the wing force measurements presented in Figures 16 through 21, the small rectangular tip apparently did not experience the same lift distribution at the model base.

Rotary Wing Applications

The trends of vortex core diameter and peak tangential velocity as a function of time, together with the velocity distributions measured during this program, have immediate application. Several analytic rotor performance, acoustic, and blade stress models currently in use contain either a prescribed or calculated wake geometry. Most existing analyses currently assume a core diameter of approximately 10 percent of the blade chord.

For a 6-blade, 21.9 meter (72 foot) diameter main rotor with a tip speed of 213.4 meters per second (700 fps), the age of a tip vortex when it passes near the following rotor blade in hover is 0.054 seconds. The data presented in Figure 10 shows that the core diameter will be approximately 3 percent of the blade chord (less than 2.5 cm or one inch), while Figure 12 shows that the peak velocities will be of the order of 152 meters per sec (500 fps) for an angle of attack of about 10 degrees. This represents a vertical velocity gradient in excess of 120 meters per second per centimeter (1000 feet per second per inch).

Detailed information such as this is important for analyses in which the core characteristics of the vortex influence the results, such as calculations of acoustic levels and frequencies, blade stress and wake trajectories.

All measured vortex velocity distributions are presented in Figures 28 through 82.

CONCLUSIONS

1. The following parameters were measured over a range of Mach numbers, Reynolds numbers, and downstream distances. Over the entire range examined, they have been found to be functions of wing lift coefficient and elapsed time from vortex formation:

   a. Vortex core diameter divided by wing chord, d_o/c, varied from 9 percent to 3 percent.

   b. Peak vortex tangential velocity divided by free stream velocity, v_θ / v_∞, varied from 0.40 to 0.76.

   c. Vortex core mean axial velocity divided by axial velocity outside of the core, varied from .95 to 1.10.

2. Rollup of the tip vortex and the inboard sheet is also a function of time, not Mach number, Reynolds number or downstream distance.

3. The trends derived from the test data of this program indicate that adequate modeling of full scale vortex structures in the wind tunnel requires that:

   a. The wind tunnel vortex is surveyed at a time from its formation equal to that of the point of interest in the full scale vortex being modeled. Since vortex age appears to be the key modeling parameter, downstream survey distance requirements can be reduced by testing at low wind tunnel velocities.

   b. The geometric angle of attack of the wind tunnel model is equal to that of the full scale wing.

   c. The model and full scale wings are similar in geometry.

   d. Measured vortex core diameter and velocity distributions are nondimensionalized by wing chord and free stream velocity respectively.

4. The tip vortex formed by the ogee tip is very diffused at all test conditions examined.

5. The maximum tangential velocity in the core of the tip vortex of the ogee tip is approximately 25 percent of the maximum tangential velocity in the core of the tip vortex of a rectangular wing at the same angle of attack.

RECOMMENDATIONS

1. A wind tunnel test should be conducted to measure axial and tangential velocity distributions in the core of a vortex at several far downstream locations at a minimum of two Mach numbers to verify the trends derived from the present study and extend the trend data to higher values of elapsed time.

2. The effects of viscosity and the turbulence of the free stream flow on the trends presented herein should be determined.

APPENDIX A

The voltage signal from a wire element heated by a constant temperature anemometer can be interpreted as a direct measure of the fluid velocity component normal to the wire length only when the effects of the fluid temperature, pressure, and density on the sensor signal can be isolated. The most common method of isolating these effects is to calibrate the non-dimensionalized heat transfer rate of the wire (Nusselt number) as a function of Reynolds number and Knudsen number (wire diameter/mean free moleculer path). A complete calibration of a single wire using this method, however, is extremely time consuming and requires the capability to independently vary the air temperature and density in the calibration wind tunnel.

As an alternative, equations were derived which expressed the percent error in the measured velocity as a function of changes in stagnation temperature and static pressure. These equations were used to correct the on-line velocity data for temperature and pressure shifts between the calibration conditions and the data run conditions. Corrections for nonlinearity remaining in the data after it was corrected by the signal linearizer and axis transfer computer circuit were also applied. The basic semi-empirical heat transfer relationship for a hot wire,which was used to construct the stagnation temperature and static pressure error expressions,was developed in reference 12 and states that:

$$H^* = (T_W - T_E)\left(6.7(p^*v^*D^*)^{0.5} + .58\left\{1 - \left[1.7 + 2\left(\frac{\delta T}{T_E}\right)\right]M\right\}\right) \qquad (1)$$

or, for a given wire:

$$H^* = (T_W - T_E)f(p^*, v^*, M)$$

where:

H^* = rate of heat transfer to the fluid in milliwatts per inch of wire length,

p^* = fluid static pressure expressed in atmospheres,

D^* = wire diameter in thousandths of an inch,

T_W = heated wire temperature in deg K,

T_E = unheated wire temperature in deg K,

M = flow Mach number,

v^* = flow velocity in units of 100 ft/sec,

δT = $T_W - T_E$.

The equation has been found to be valid within 10% for Reynolds numbers based on wire diameter between 0 and 500, and Mach numbers between 0 and 1.9. It, therefore, serves as an excellent base for making corrections to a previously calibrated wire.

Temperature Corrections

By equating the rate of thermal energy loss from the wire to the rate of electrical energy supplied to the wire, it is apparent that:

$$f(p^*,v^*,M) = \frac{I^2 R_W}{(T_W - T_E)\ell} \qquad (2)$$

where ℓ equals the sensitive wire length.

The temperature terms in equations (1) and (2) can be expressed in terms of the wire overheat ratio (h) with the following relationships:

$$T_E \simeq T_O$$

$$R_W - R_E = R_O \alpha_O \ (T_W - T_E) \qquad (3)$$

$$h = R_W / R_E \qquad (4)$$

therefore:

$$f(p^*,v^*, M) = \frac{I^2 R_O \alpha_O}{\ell} \left(\frac{h}{h-1}\right)$$

$$= 6.7 \ (p^* \ v^* \ D^*)^{0.5} + .58\left\{1 - [1.7 + 2(h-1)]M\right\} \qquad (5)$$

The error in measured velocity (δv^*) caused by a stagnation temperature change (δT_o) can now be evaluated by perturbing the wire overheat ratio (h) and solving (5) for the corresponding v^*.

The required equation relating the overheat ratio perturbation (δh) and δT_o can be derived directly from the following expression which was developed in reference 12 to define the magnitude of the perturbed wire equilibrium resistance (R'_E) after the air stream stagnation temperature has shifted by δT_o.

$$R'_E = R_E (1 + \alpha_o \delta T_o)$$

The relationship is valid in this form when the constant α_o is measured at a temperature which is close to the tunnel stagnation temperature. For this study

a value of .004/°C was experimentally determined for α_o at a stagnation temperature of 42° C.

From the previous expression, the perturbed overheat ratio (h') can be calculated as:

$$h' = \frac{R_W}{R'_E} = \frac{R_W}{R_E}\frac{R_E}{R'_E} = \frac{h}{1 + \alpha_o \delta T_o}$$

The magnitude of the corresponding overheat ratio perturbation is then:

$$\delta h = h - h' = \frac{\alpha_o h \delta T_o}{1 + \alpha_o \delta T_o}$$

For small T_o fluctuations, as experienced in this program, this expression can be accurately approximated as:

$$\delta h = \alpha_o h \delta T_o \tag{6}$$

From (5) and (6),

$$\frac{\delta f(p^*, v^*, M)}{f(p^*, v^*, M)} = - \frac{\alpha_o \delta T_o}{h - 1} \tag{7}$$

Also from (6) and the right hand side of (5),

$$\frac{\delta f(p^*, v^*, M)}{f(p^*, v^*, M)} = \frac{6.7\left[p^*(v^* + \delta v^*)D^*\right]^{0.5} + .58\left\{1 - \left[1.7 + 2(h + \alpha_o h \delta T_o - 1)\right]M\right\}}{6.7\,(p^* v^* D^*)^{0.5} + .58\left\{1 - \left[1.7 + 2(h-1)\right]M\right\}} \tag{8}$$

Equating (7) and (8), approximating

$$\left[p^*\,(v^* + \delta v^*)D^*\right]^{0.5}$$

with the partial Taylor series

$$(p^*v^*D^*)^{0.5} + p^*D^*\delta V^* /2 (p^*v^*D^*)^{0.5}$$

and collecting terms yields the following stagnation error expression for v^* due to a T_o change.

$$\frac{\delta v^*}{v^*} = \frac{-2\alpha_o \delta T_o}{h-1}\left(1 + \frac{.58}{6.7(p^*v^*D^*)^{0.5}}\left\{1 - M\left[1.7 + 2(h-1) + 1.16h\,(h-1)\right]\right\}\right) \tag{9}$$

For velocities greater than 100 fps and Mach numbers below 0.7, equation (9) can be written as:

$$\frac{\delta v^*}{v^*} = \frac{-2\,\alpha_o \delta T_o}{h-1} \tag{10}$$

Pressure Correction

An error expression for the change in measured velocity (δv^*) caused by a shift in static pressure (δp^*) can be obtained by differentiating the basic heat transfer relationship as expressed in equation (5). The Mach number differential (δM) is included in order to access its significance. Also, the term

$$\frac{I^2R_o\alpha_o}{\ell}\quad\frac{h}{h-1}$$

of equation (5) is now constant as it does not vary with either Mach number or static pressure.

Hence:

$$3.35(p^*v^*D^*)^{-0.5}(p^*D^*\delta v^*) - .58\left\{1 - \left[1.7 + 2(h-1)\right]\right\}\delta M$$

$$+ 3.35\,(p^*v^*D^*)^{-.5}\,(D^*v^*\delta p^*) = 0 \tag{11}$$

or;

$$\frac{\delta v^*}{v^*} = \frac{.58\left[1.7 + 2(h-1)\right]\delta M}{3.35\,(p^*D^*v^*)^{0.5}} - \frac{\delta p^*}{p^*} \tag{12}$$

Again, the Mach number effect is not significant for the Mach number range covered in the test program. The accuracy of equation (12) was checked against the experimental data presented in reference 15 with the result that 90% of the error induced in the velocity measurement due to static pressure changes was eliminated.

Linearity Correction

The on-line vortex data were corrected for linearization errors by calculating, from the analog computer outputs, the cooling velocity sensed by each wire of the three element probe, correcting these velocities for known nonlinearities, and then reconstructing the required tangential and axial velocities from the corrected cooling velocities. The degree of nonlinearity remaining in each wire signal after passage through the on line linearizers was determined during the probe calibration. Since the linearity correction effects only the magnitude of the maximum tangential velocity and not its position, linearity corrections were not required for vortex location.

The relationship between the probe co-ordinate system ($\vec{i}'$, $\vec{j}'$, $\vec{k}'$) and the tunnel co-ordinate system ($\vec{i}$, $\vec{j}$, $\vec{k}$) is illustrated below.

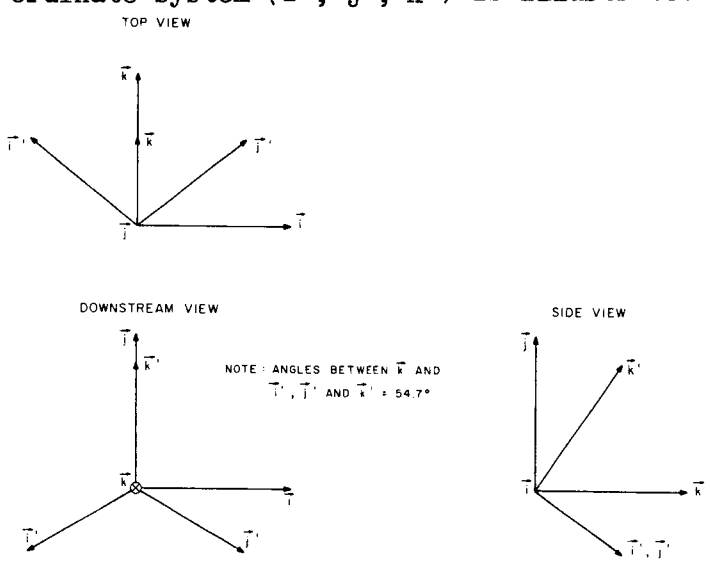

Accordingly the conversion from the $\vec{i}'$, $\vec{j}'$, $\vec{k}'$ and the $\vec{i}$, $\vec{j}$, $\vec{k}$ orthogonal triads is then:

$$\left.\begin{aligned} \vec{i} &= -(1/2)^{0.5}\ \vec{i}' + (1/2)^{0.5}\ \vec{j}' \\ \vec{j} &= -(1/6)^{0.5}\ \vec{i}' - (1/6)^{0.5}\vec{j}' + (2/3)^{0.5}\vec{k}' \\ \vec{k} &= (1/3)^{0.5}\ \vec{i}' + (1/3)^{0.5}\vec{j}' + (1/3)^{0.5}\vec{k}' \end{aligned}\right\} \quad (13)$$

and the uncorrected velocity components v_{ux}, v_{uy}, v_{uz} parallel to the three probe wires can be expressed in terms of the uncorrected velocities v_{uX}, v_{uY}, and v_{uZ} measured in the tunnel coordinate system as:

$$
\left.
\begin{aligned}
v_{ux} &= (\vec{i} \cdot \vec{i}')\, v_{uX} + (\vec{j} \cdot \vec{i}')v_{uY} + (\vec{k} \cdot \vec{i}')\, v_{uZ} \\
v_{uy} &= (\vec{i} \cdot \vec{j}')\, v_{uX} + (\vec{j} \cdot \vec{j}')v_{uY} + (\vec{k} \cdot \vec{j}')\, v_{uZ} \\
v_{uz} &= (\vec{i} \cdot \vec{k}')\, v_{uX} + (\vec{j} \cdot \vec{k}')v_{uY} + (\vec{k} \cdot \vec{k}')\, v_{uZ}
\end{aligned}
\right\} \qquad (14)
$$

or :

$$
\left.
\begin{aligned}
v_{ux} &= -(1/2)^{0.5}\, v_{uX} - (1/6)^{0.5} v_{uY} + (1/3)^{0.5} v_{uZ} \\
v_{uy} &= (1/2)^{0.5}\, v_{uX} - (1/6)^{0.5} v_{uY} + (1/3)^{0.5} v_{uZ} \\
v_{uz} &= (2/3)^{0.5} v_{uY} + (1/3)^{0.5} v_{uZ}
\end{aligned}
\right\} \qquad (15)
$$

The uncorrected cooling velocities v_{unx}, v_{uny}, v_{unz} which are normal to the x, y, z wire directions are respectively identified as:

$$
\left.
\begin{aligned}
v_{unx} &= (v_{uy}^{2} + v_{uz}^{2})^{0.5} \\
v_{uny} &= (v_{ux}^{2} + v_{uz}^{2})^{0.5} \\
v_{unz} &= (v_{ux}^{2} + v_{uy}^{2})^{0.5}
\end{aligned}
\right\} \qquad (16)
$$

The voltages V_x, V_y, V_z sensed by the three wires can now be calculated by dividing v_{unx}, v_{uny}, v_{unz} by the scale factor C (ft/volt sec) which was assumed for reducing the on-line data. The choice of C is arbitrary since the velocities in the tunnel co-ordinate system are directly proportional to the assumed C.

$$
\begin{aligned}
V_x &= \frac{v_{unx}}{C} \\
V_y &= \frac{v_{uny}}{C} \qquad (17) \\
V_z &= \frac{v_{unz}}{C}
\end{aligned}
$$

Corrected cooling velocities v_{nx}, v_{ny}, v_{nz} can now be obtained from the actual voltage vs. velocity curves determined during the calibration of the wires and linearizers as shown in the following illustration.

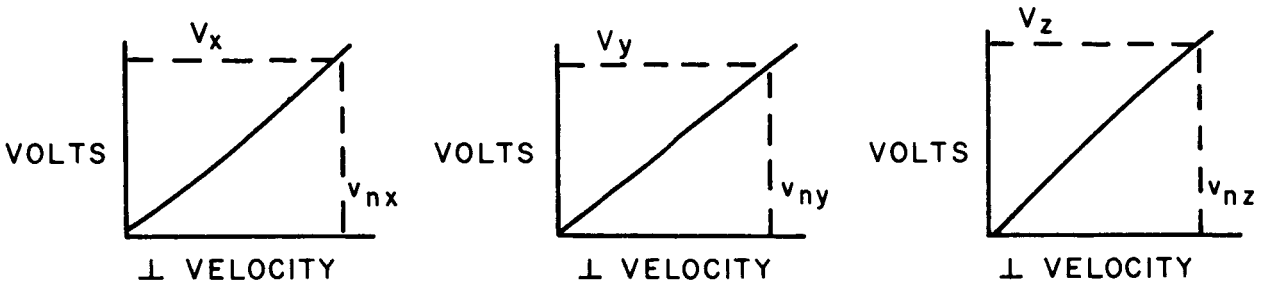

The corrected velocities in the wind tunnel coordinate system are then reconstructed as follows:

$$\left.\begin{aligned} v_x &= 0.5\left[\left(-v_{nx}^2 + v_{ny}^2 + v_{nz}^2\right)\right]^{0.5} \\ v_y &= 0.5\left[\left(v_{nx}^2 - v_{ny}^2 + v_{nz}^2\right)\right]^{0.5} \\ v_z &= 0.5\left[\left(v_{nx}^2 + v_{ny}^2 - v_{nz}^2\right)\right]^{0.5} \end{aligned}\right\} \quad (18)$$

$$\left.\begin{aligned} v_X &= -(1/2)^{0.5} v_x + (1/2)^{0.5} v_y \\ v_Y &= -(1/6)^{0.5} v_x - (1/6)^{0.5} v_y + (2/3)^{0.5} v_z \\ v_Z &= (1/3)^{0.5} v_x + (1/3)^{0.5} v_y + (1/3)^{0.5} v_z \end{aligned}\right\} \quad (19)$$

It should be noted that the vortex radial velocities (v_Y for a spanwise traverse and v_X for a normal traverse) were assumed to be zero for all data corrections. This assumption is valid only outside the vortex core region as shown by Chigier and Corsiglia in reference 11. However, linearity corrections calculated with an assumed radial velocity distribution in the core similar to that measured in reference 11 showed no significant effect on the calculated tangential and axial velocities.

REFERENCES

1. Jenney, D. S.; Olson, J. R.; and Landgrebe, A. J.: A Reassessment of Rotor Hovering Performance Prediction Methods. J. Am. Helicopter Soc., vol. 13, no. 2, April 1968.

2. Clark, D. R.; and Leiper, A. C.: The Free Wake Analysis. J. Am. Helicopter Soc., vol. 15, no. 1, January, 1970, pp 3-11.

3. Rorke, J. B.; and Wells, C. D.: The Prescribed Wake-Momentum Analysis. Proceedings of the Third Annual CAL/AVLABS Symposium, (Buffalo, New York), June 18-20, 1969.

4. Ward, J. F.: Helicopter Rotor Periodic Differential Pressures and Structural Response Measured in Transient and Steady State Maneuvers. J. Am. Helicopter Soc., vol. 16, no. 1, January 1971, pp 16-25.

5. Widnal, S.: Helicopter Noise Due to Blade-Vortex Interaction. J. Acoust. Soc. Am., vol. 50, no. 1, part 2, July 1971, pp 354-365.

6. Landgrebe, A. J.: An Analytical Method for Predicting Rotor Wake Geometry, AIAA/AHS/Georgia Tech VTOL Aircraft Meeting, September 1968.

7. Sadler, S. G.: A Method for Predicting Helicopter Wake Geometry, Wake Induced Flow, and Wake Effects on Blade Airloads. Paper presented at the 27th Annual National Forum of the American Helicopter Society (Washington, D. C.), May 1971.

8. Batchelor, G. K.: Axial Flow in Trailing Vortices. J. Fluid Mech., vol. 20, part 4, 1964, pp 645-658.

9. Spivey, R. F.: Blade Tip Aerodynamics - Profile and Planform Effects. Proceedings of the 24th Annual National Forum of the American Helicopter Society (Washington, D. C.), May 1968.

10. Wickens, R. H.: The Vortex Wake and Aerodynamic Load Distribution of Slender Rectangular Wings. Canadian Aeronautics and Space Journal, vol. 13, no. 6, June 1967, pp 247-260.

11. Chigier, N. A.; and Corsiglia, V. R.: Tip Vortices - Velocity Distributions. Paper presented at the 27th Annual National Forum of the American Helicopter Society (Washington, D. C.), May 19-21, 1971.

12. Flow Corporation Bulletin No. 25: Selected Topics in Hot Wire Anemometer Theory. Flow Corporation, Cambridge, Massachusetts.

13. Chigier, N. A.: Velocity Measurement in Vortex Flows. Paper presented at the ASME Fluids Engineering Division Conference (Pittsburgh, Pennsylvania), May 11, 1971.

14. Newman, B. G.: Flow in a Viscous Trailing Vortex. Aeron. Quart., vol. 10, February - November 1959, pp 149-162.

15. Norman, B.: Hot-Wire Anemometer Calibration at High Subsonic Speeds. DISA Information, no. 5, DISA S & B, Franklin Lakes, N.J., June 1967, pp 5-19.

16. McCormick, B. W.; and Tangler, J. L.: A Study of the Vortex Sheet Immediately Behind an Aircraft Wing. The Pennsylvania State University Department of Aeronautical Engineering, University Park, Pennsylvania, December, 1965.

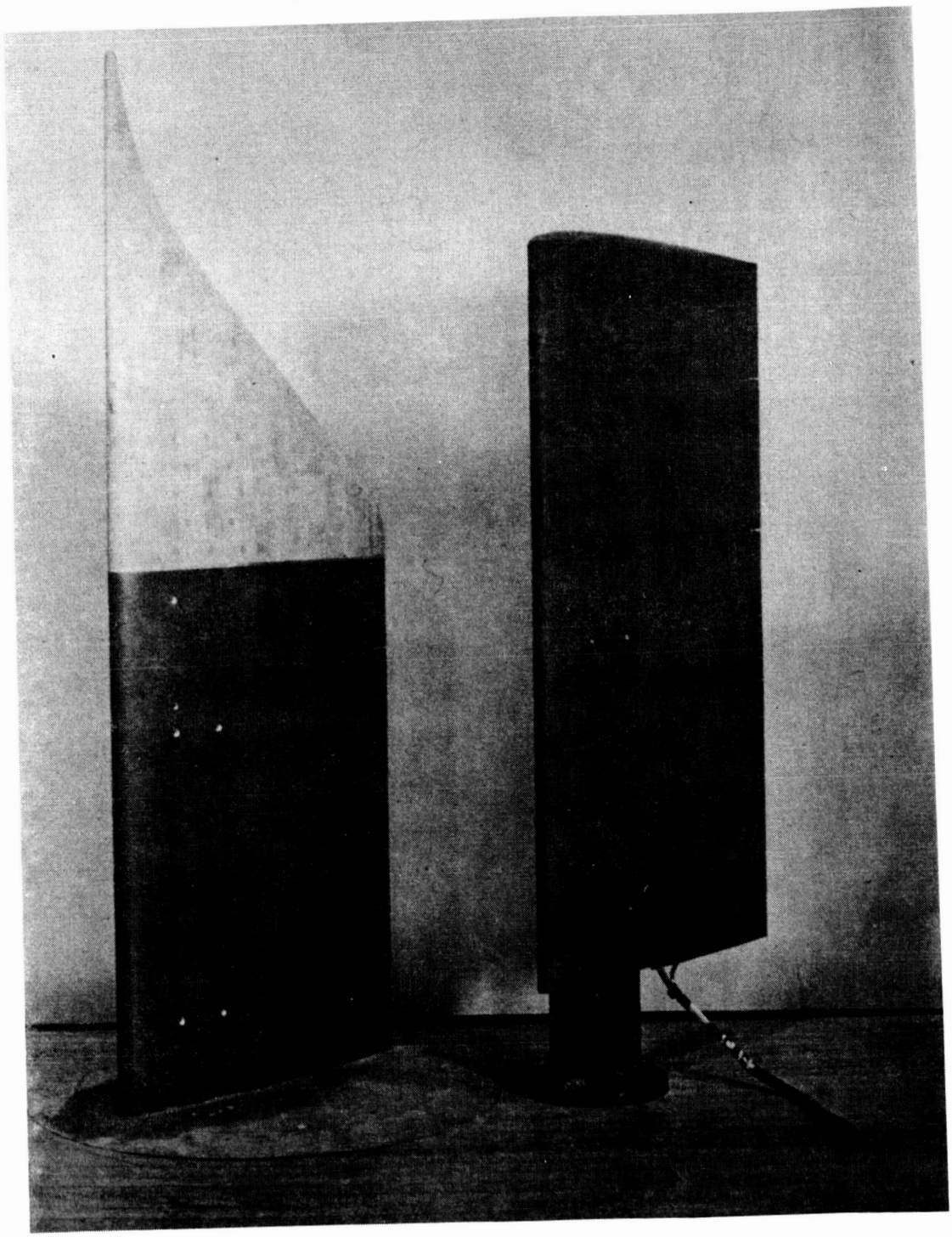

Figure 1. Large Rectangular and Ogee Wing Tips

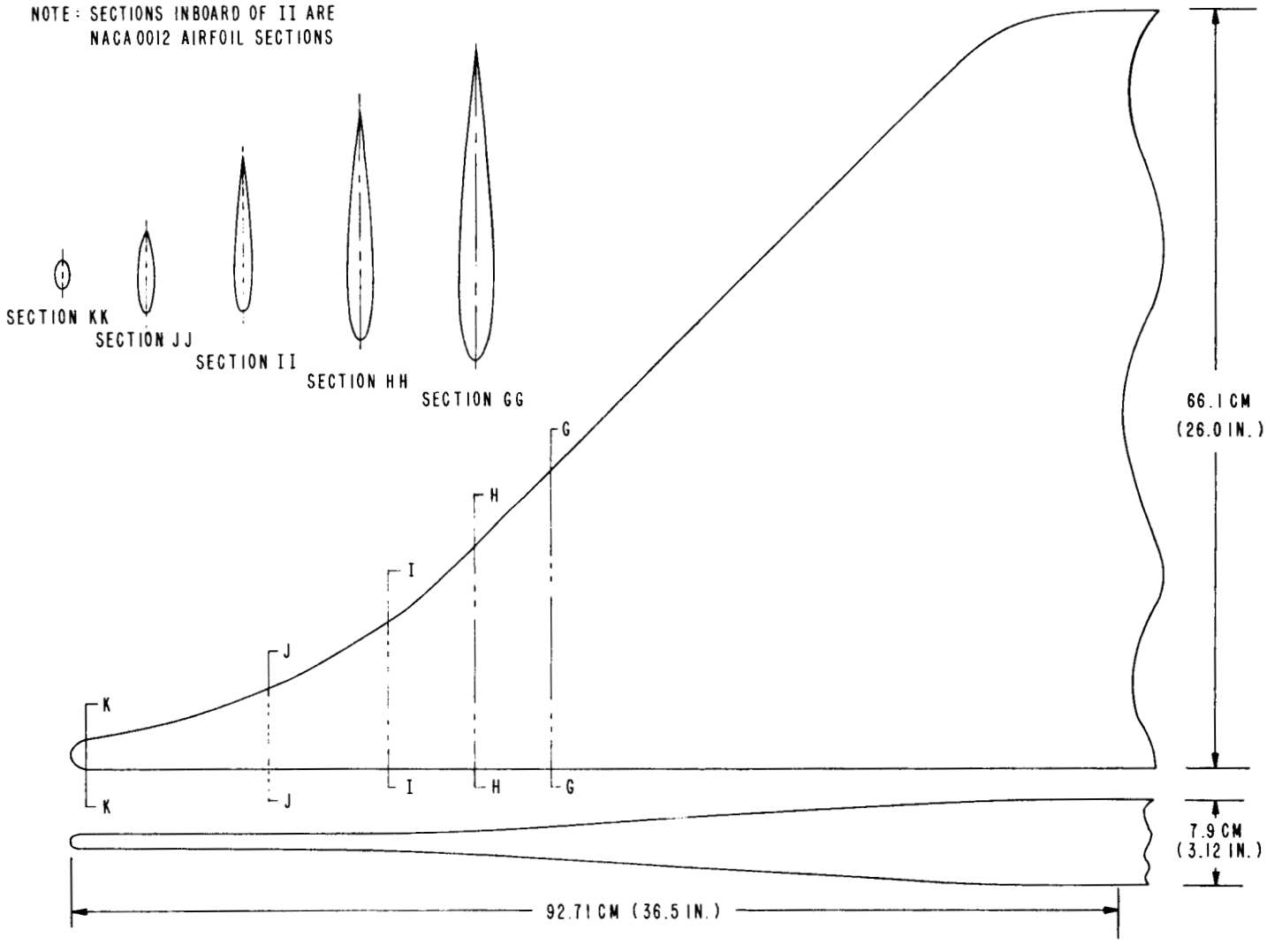

Figure 1. Continued - Ogee Wing Tip

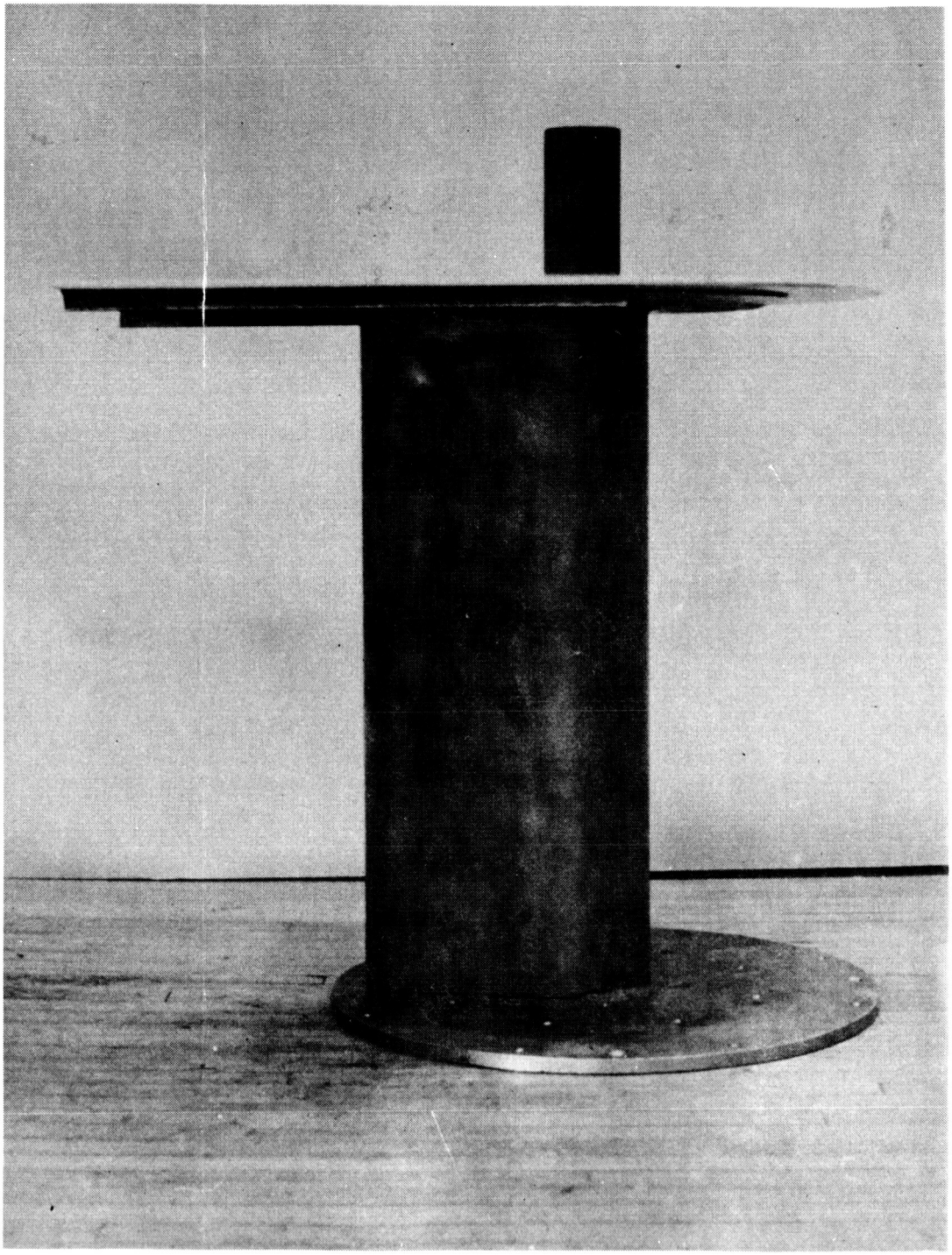

Figure 2. Small Rectangular Wing Tip, Support Base, and Ground Plane

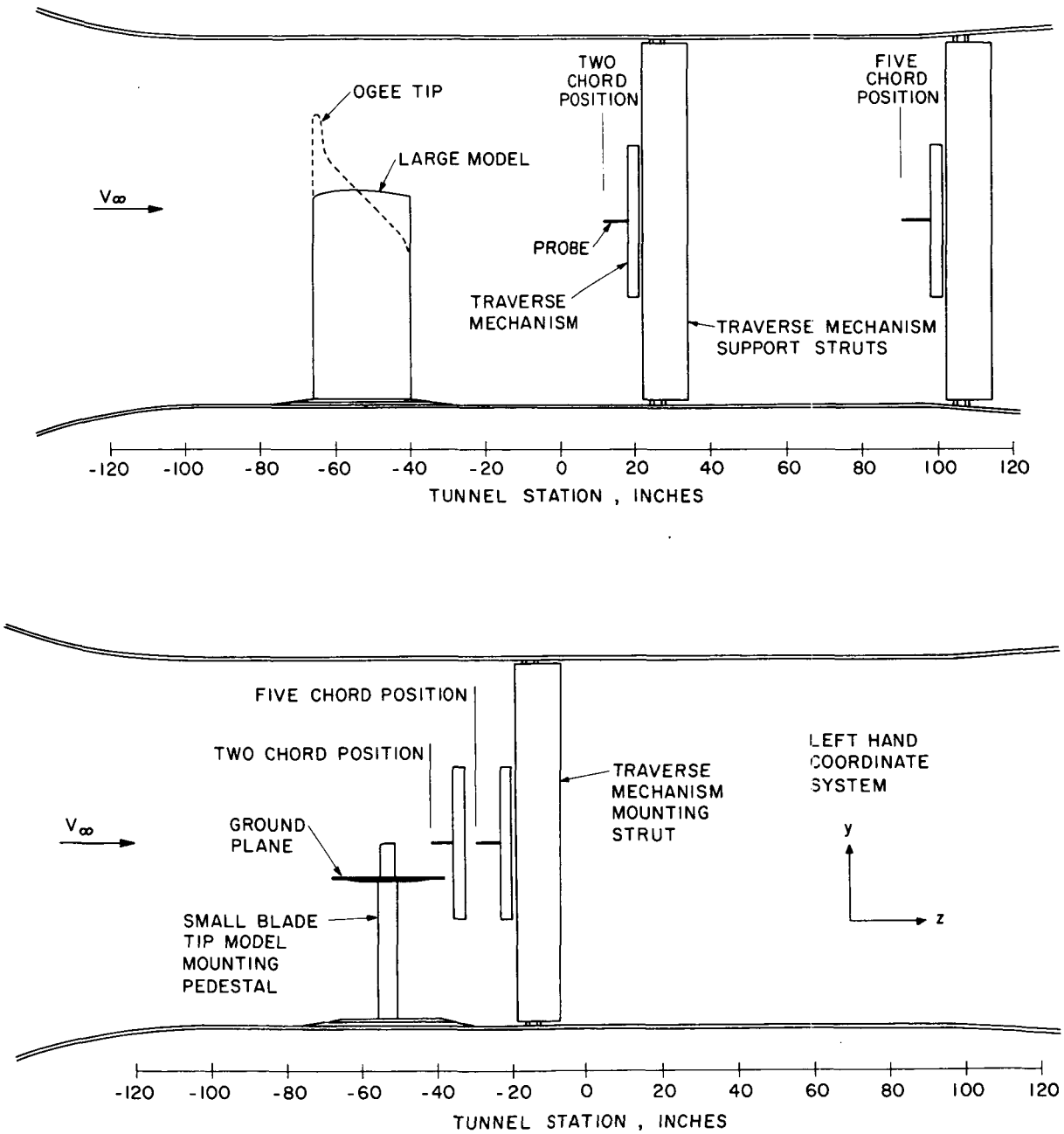

Figure 3. Wing and Probe Installation in Wind Tunnel

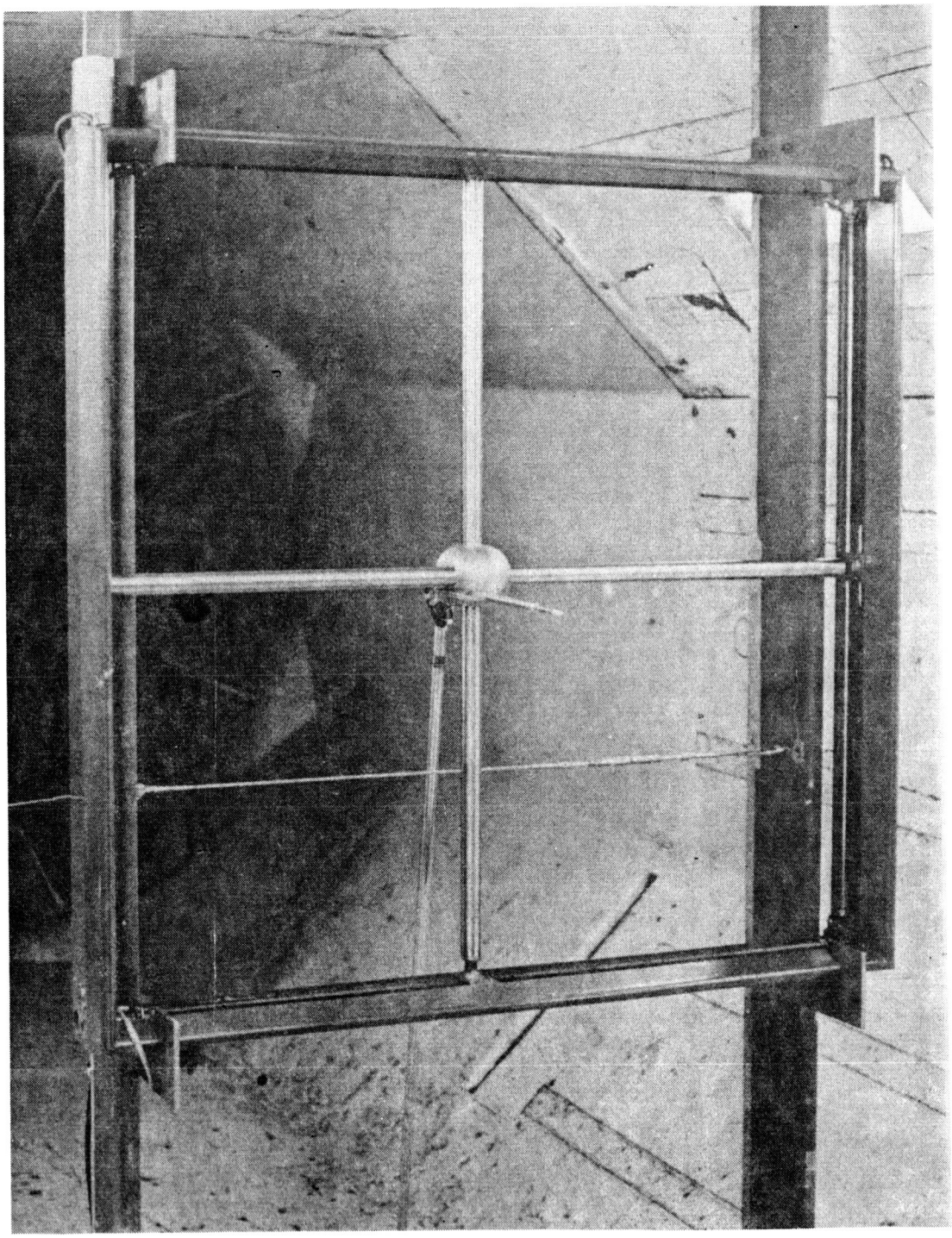

Figure 4. Traverse Mechanism in Wind Tunnel

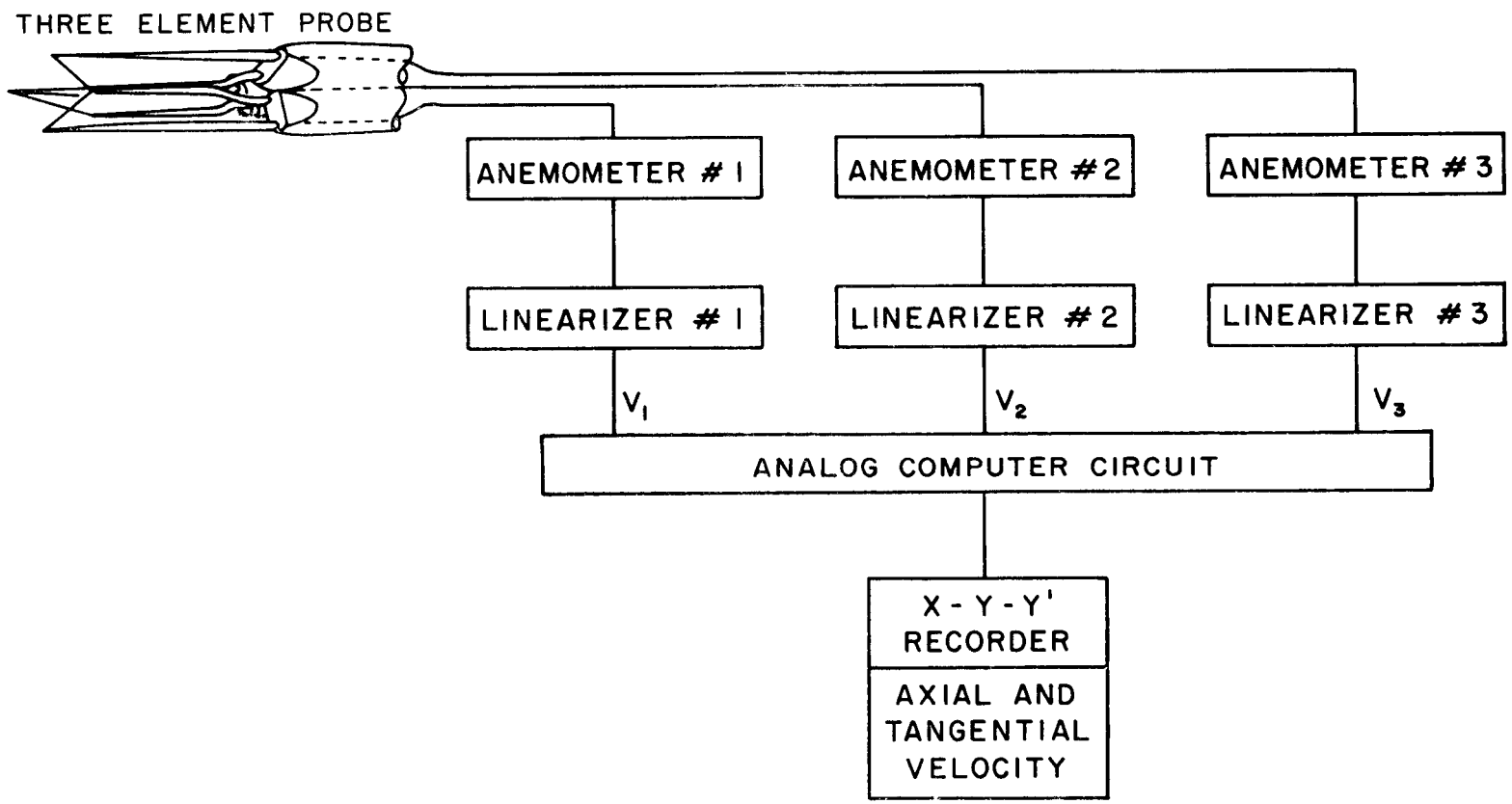

Figure 5. Schematic of Anemometer Instrumentation

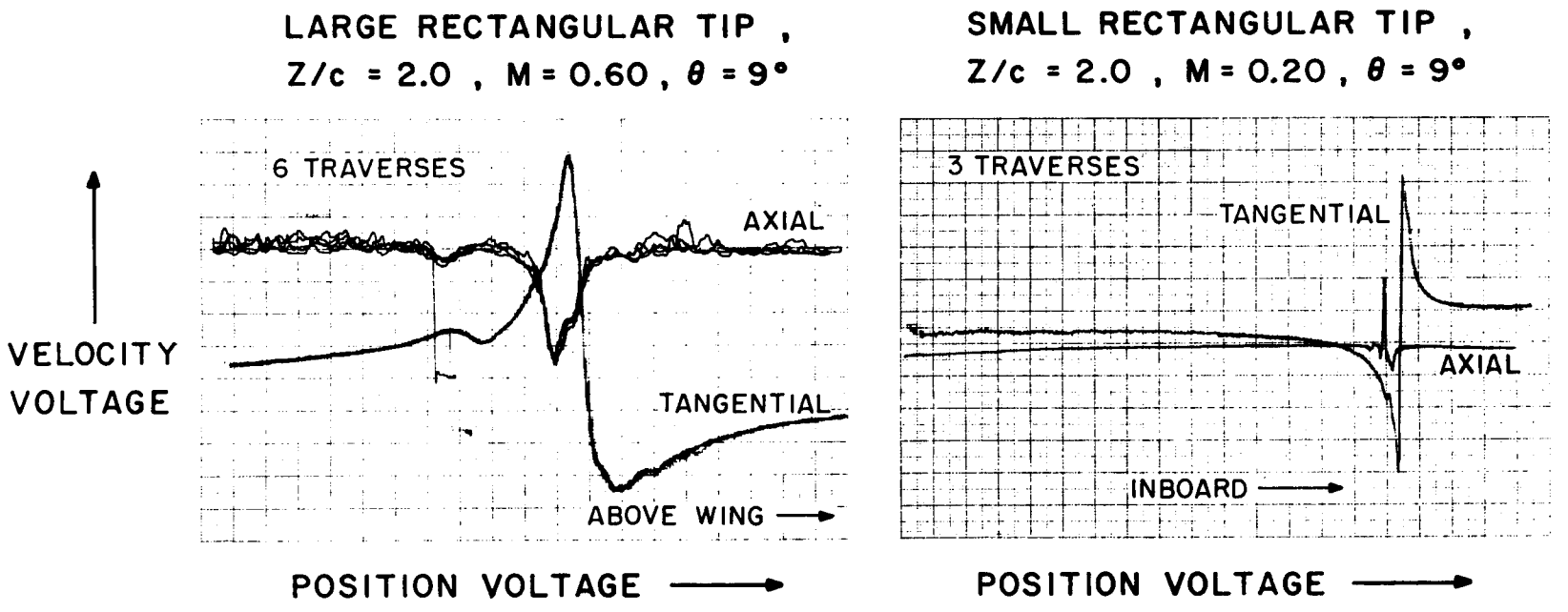

Figure 6. Sample On-Line Vortex Velocity Data

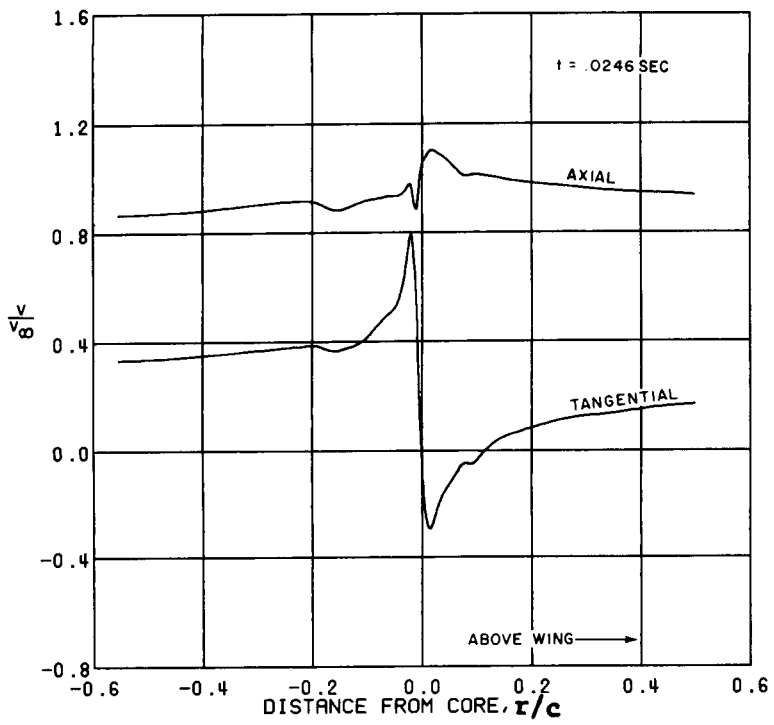

Probe No. 5 on June 23, 1971.

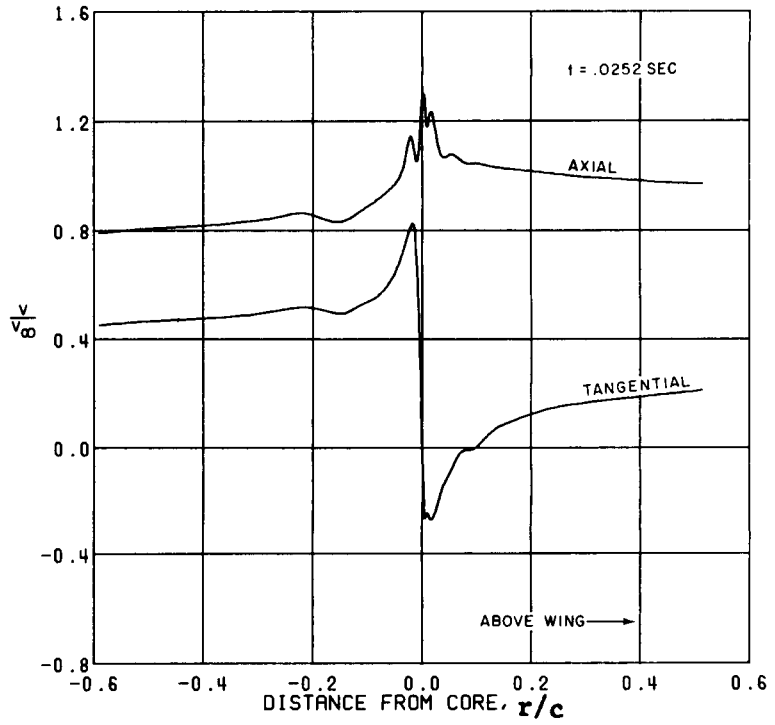

Probe No. 8 on July 12, 1971.

Figure 7. Repeat Data, Large Rectangular Tip Vortex Velocity Distribution, Z/c = 2.0, M = 0.20, θ = 6 degrees

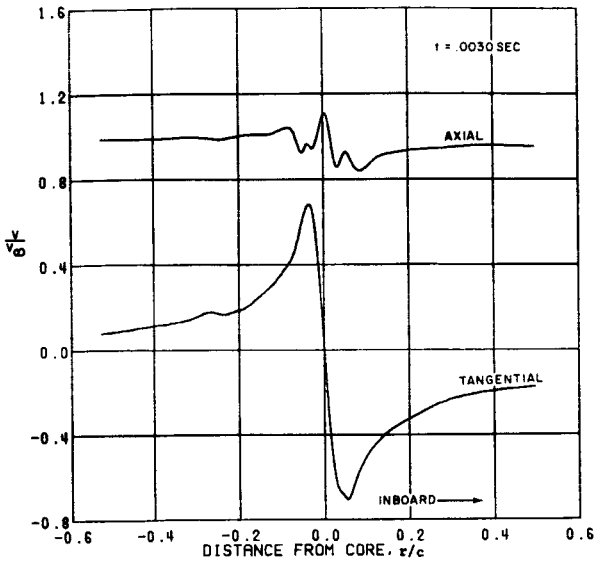

a. Small Rectangular Wing, M = 0.60.

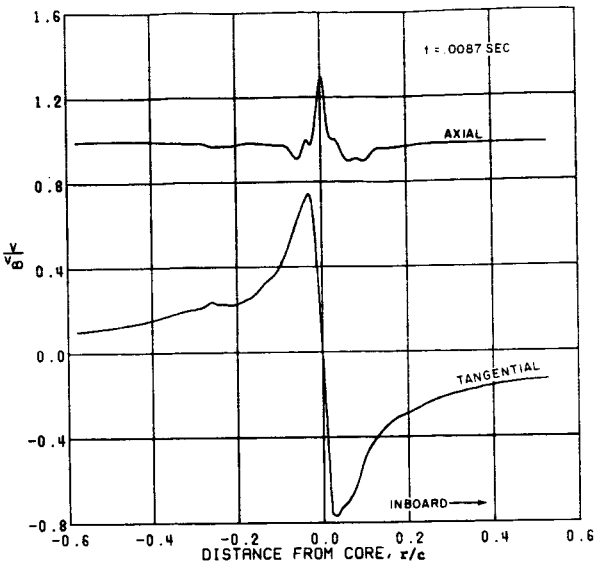

b. Small Rectangular Wing, M = 0.20.

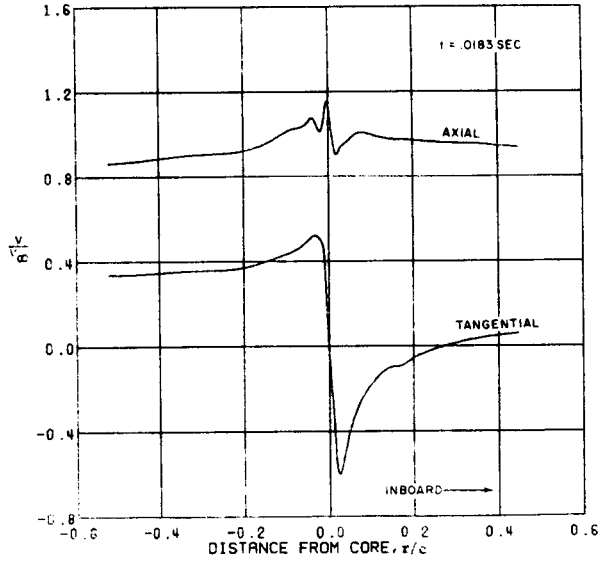

c. Large Rectangular Wing, M = 0.60.

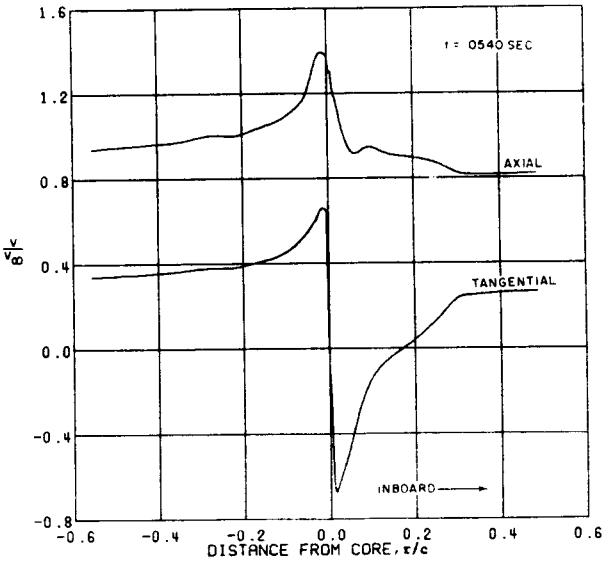

d. Large Rectangular Wing, M = 0.20.

Figure 6. Sequence of Vortex Velocity Plots for Spanwise Traverse Illustrating the Influence of Vortex Age on Velocity Symmetry, Z/c = 5.0, Θ = 9 deg.

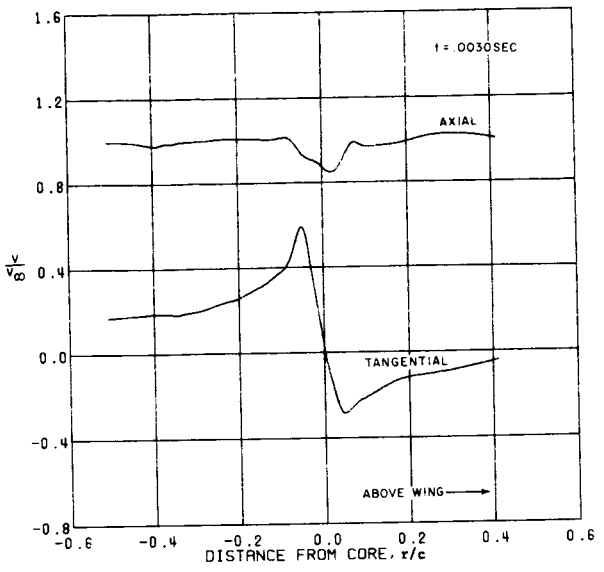

a. Small Rectangular Wing, M = 0.60.

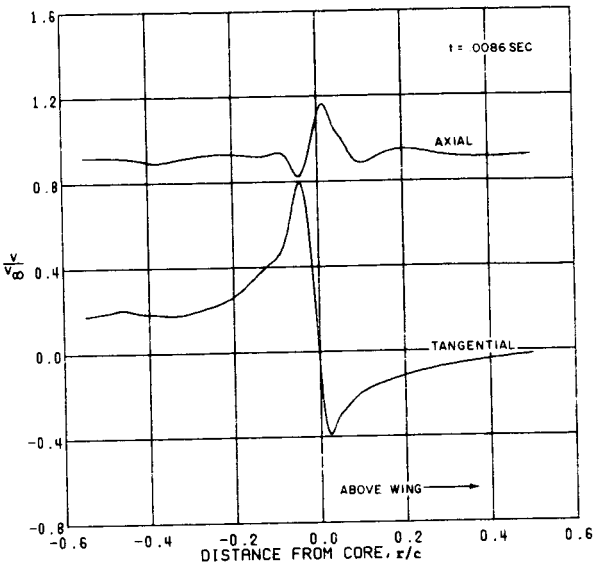

b. Small Rectangular Wing, M = 0.20.

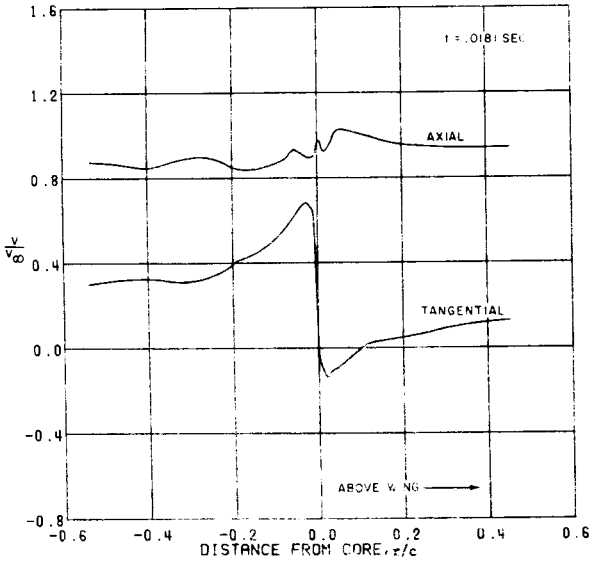

c. Large Rectangular Wing, M = 0.60.

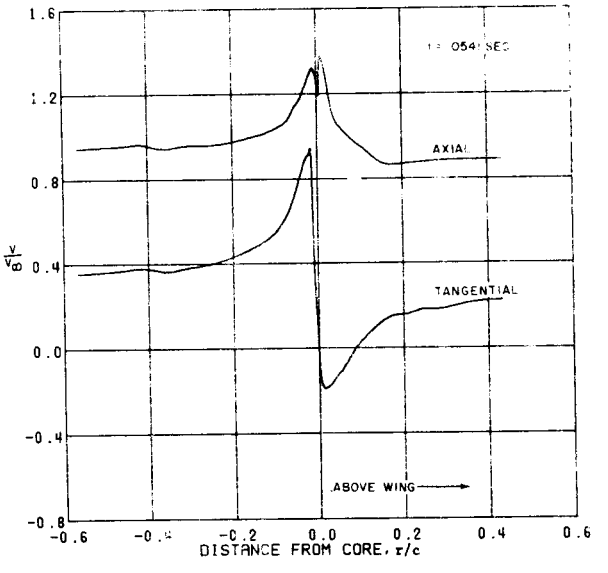

d. Large Rectangular Wing, M = 0.20.

Figure 9. Sequence of Vortex Velocity Plots for Normal Traverses Illustrating the Influence of Vortex Age on Velocity Symmetry, Z/c = 5.0, θ = 9 deg.

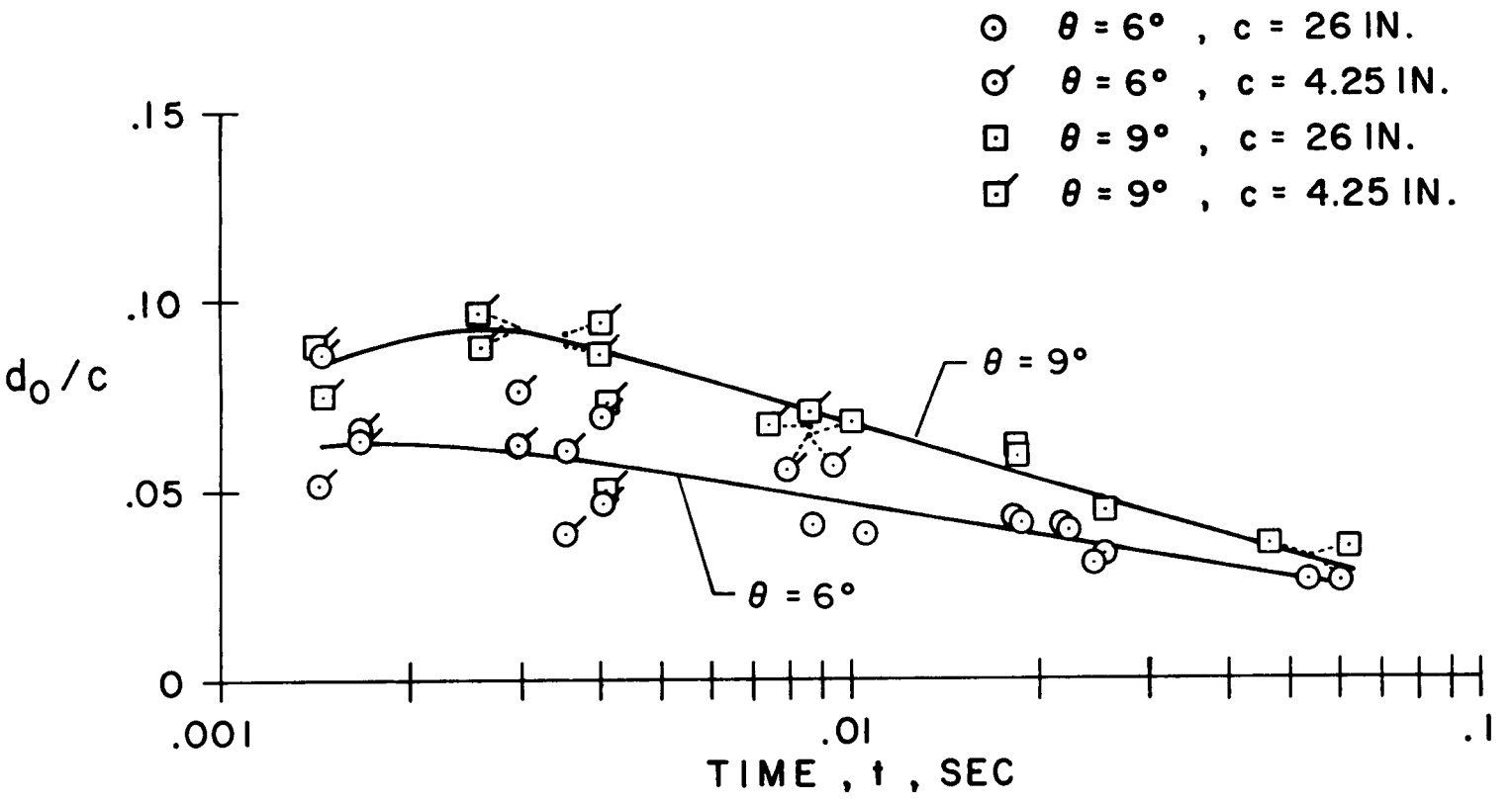

Figure 10. Vortex Core Diameter as a Function of Vortex Age

$\theta = 9°$

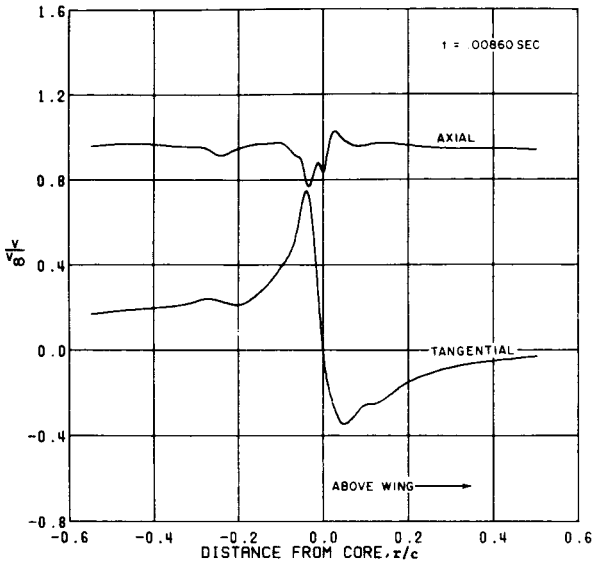

a. Large Rectangular Tip, Z/c = 2.0, M = 0.60.

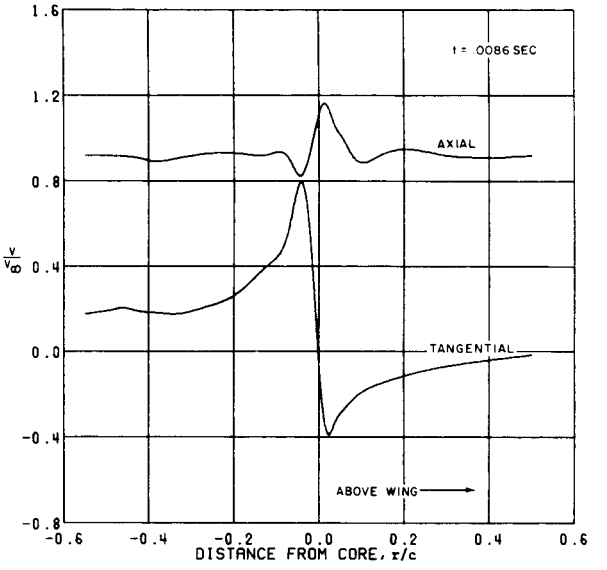

b. Small Rectangular Tip, Z/c = 5.0, M = 0.20.

$\theta = 6°$

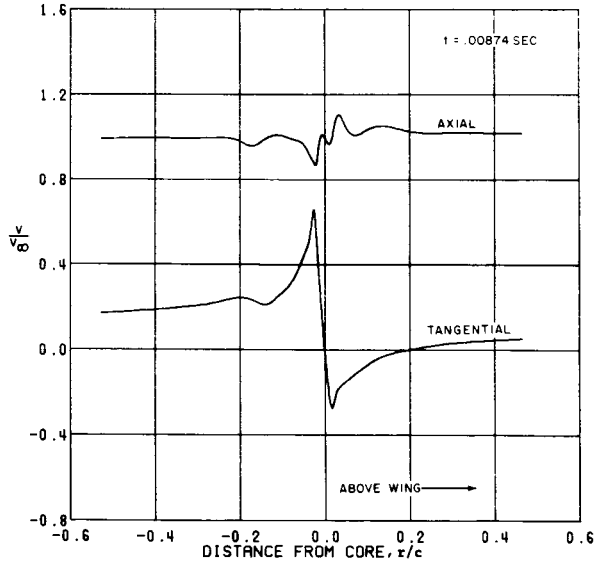

c. Large Rectangular Tip, Z/c = 2.0, M = 0.60.

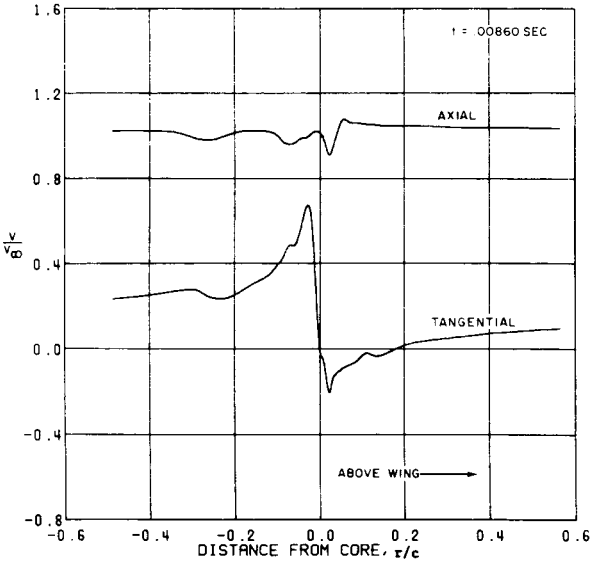

d. Small Rectangular Tip, Z/c = 5.0, M = 0.20.

Figure 11. Vortex Velocity Distributions for Various Test Conditions at Approximately Equal Vortex Ages

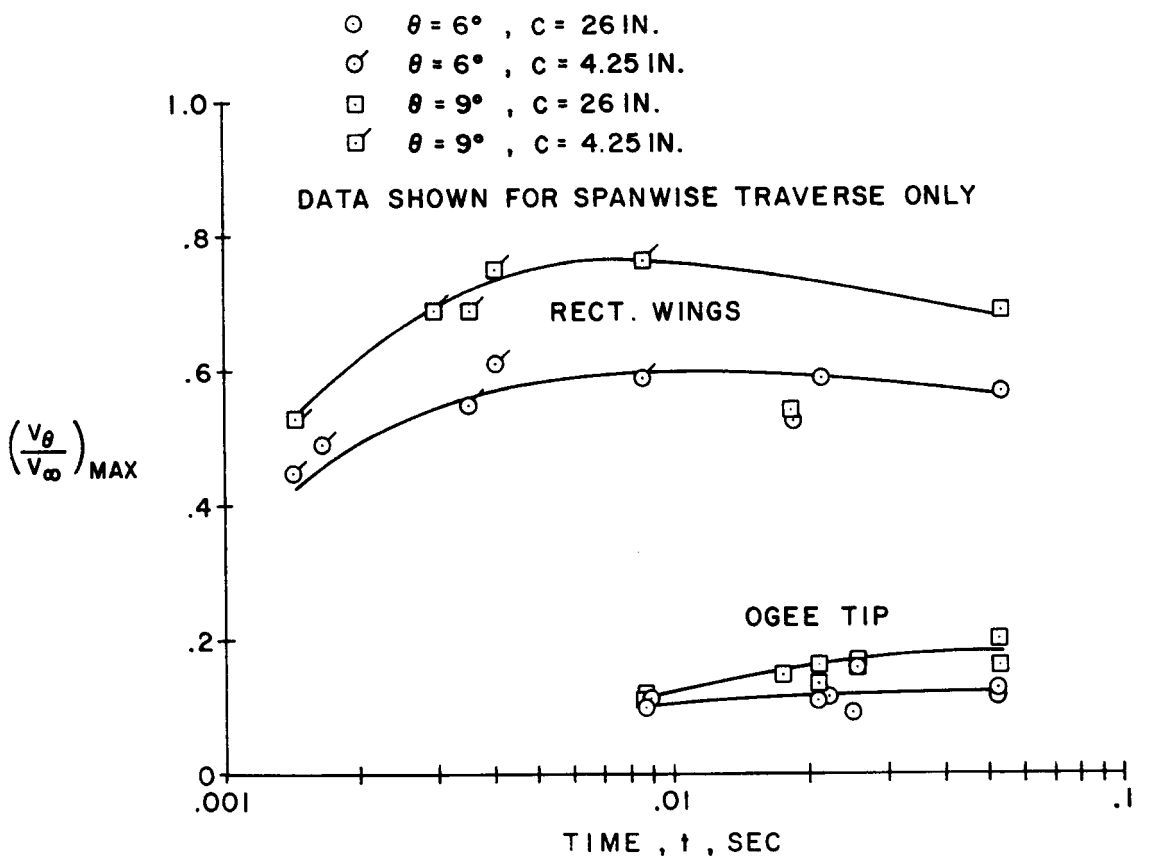

Figure 12. Maximum Tangential Velocity as a Function of Vortex Age

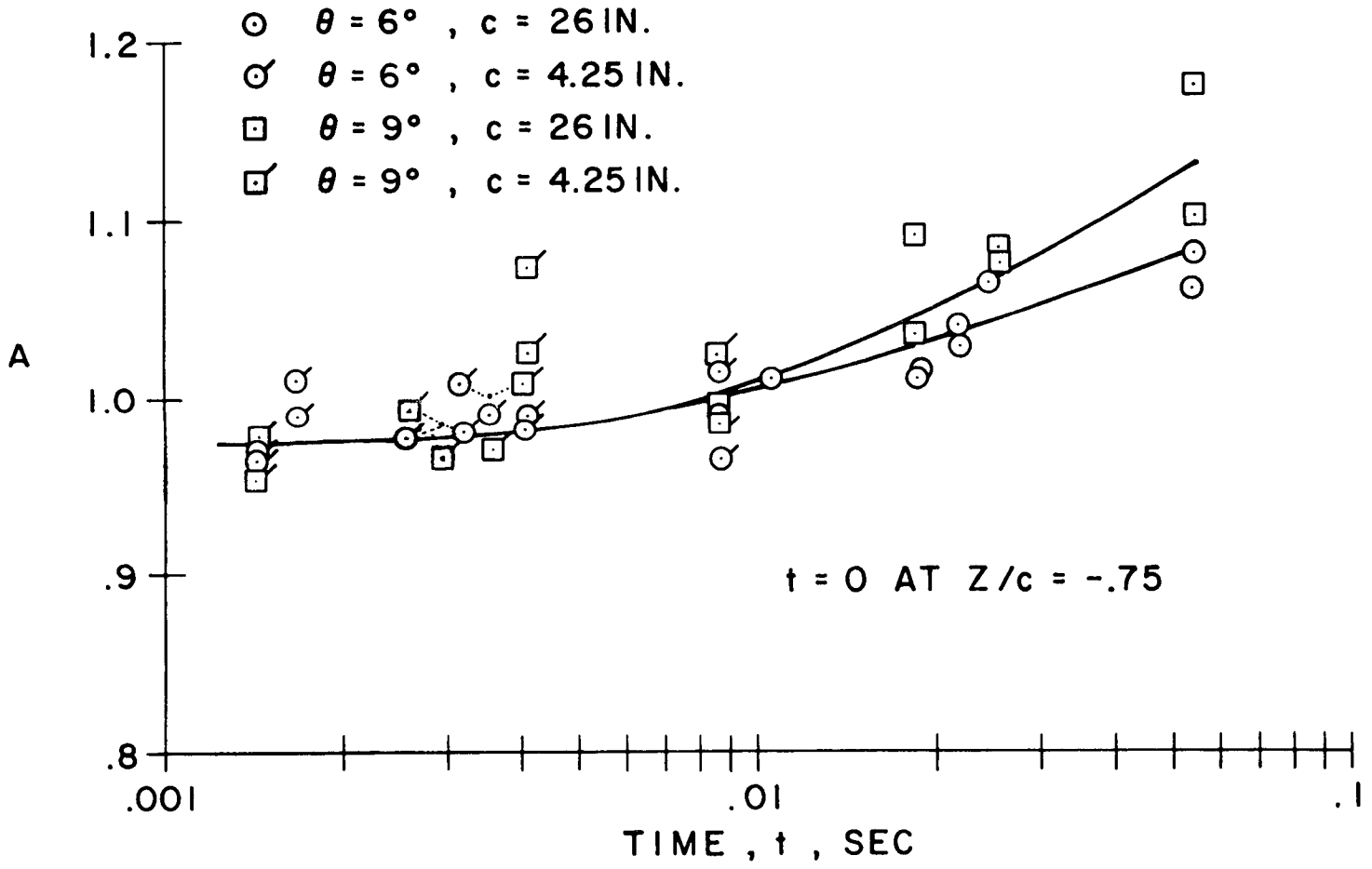

Figure 13. Mean Axial Velocity Ratio, A, as a Function of Vortex Age

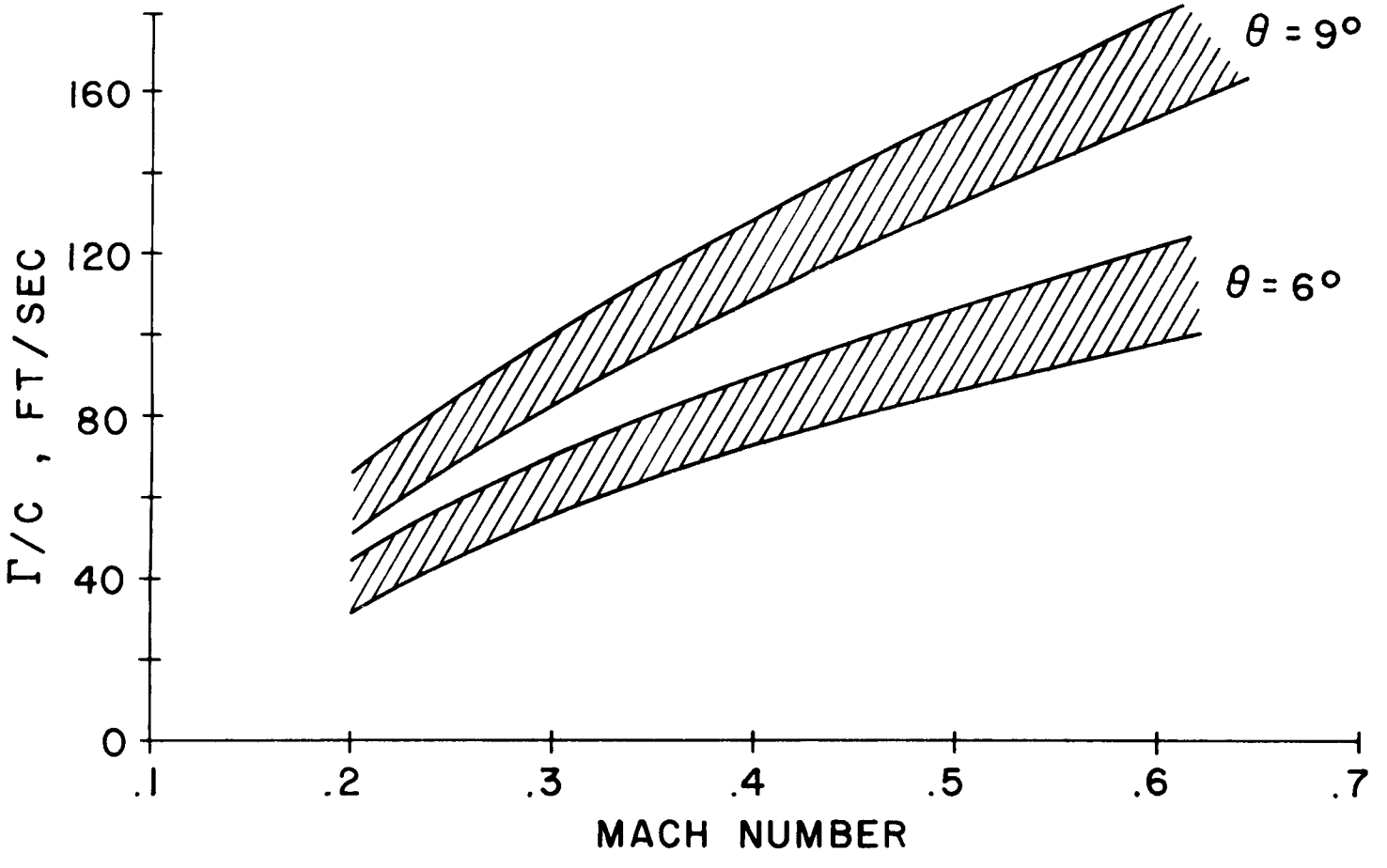

Figure 14. Vortex Circulation Strength as a Function of Mach Number and Wing Pitch Angle for Rectangular Wings

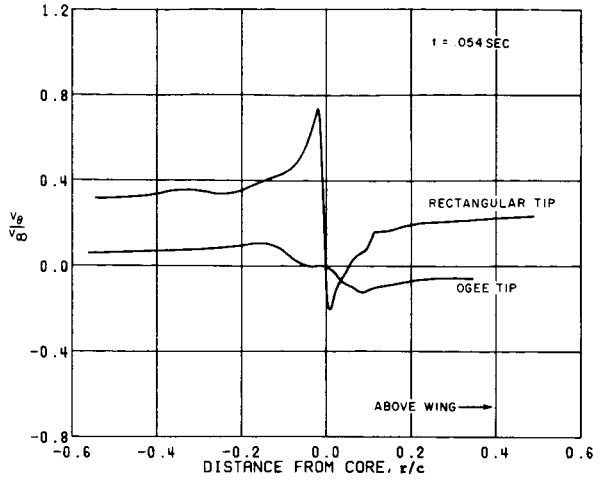

a. M = 0.20, Normal Traverse.

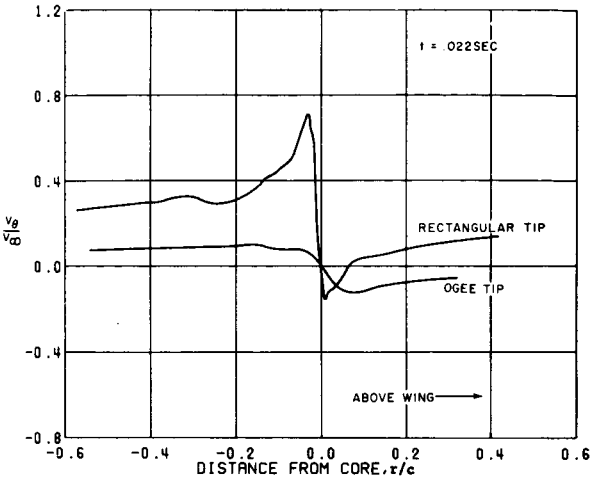

b. M = 0.50, Normal Traverse.

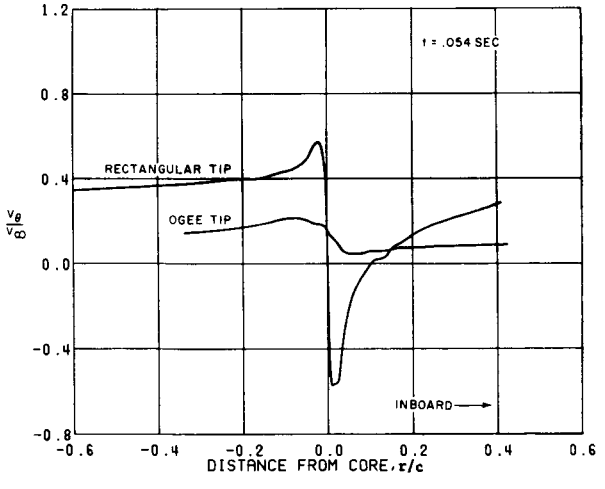

c. M = 0.20, Spanwise Traverse.

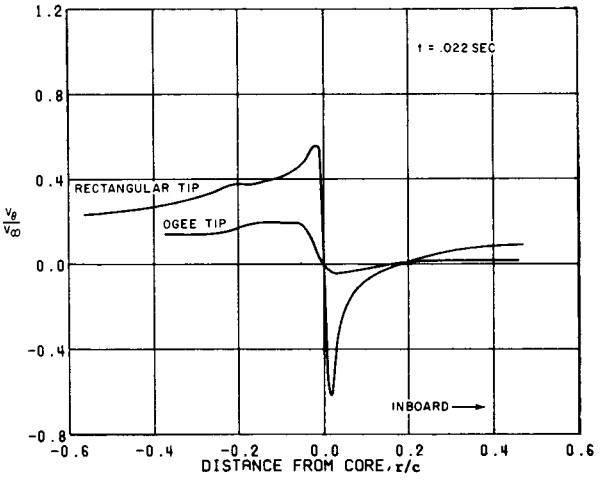

d. M = 0.50, Spanwise Traverse.

Figure 15. Comparison of Ogee Tip and Large Rectangular Tip Tangential Velocity Distributions at Selected Test Conditions, Z/c = 5.0, θ = 6 deg.

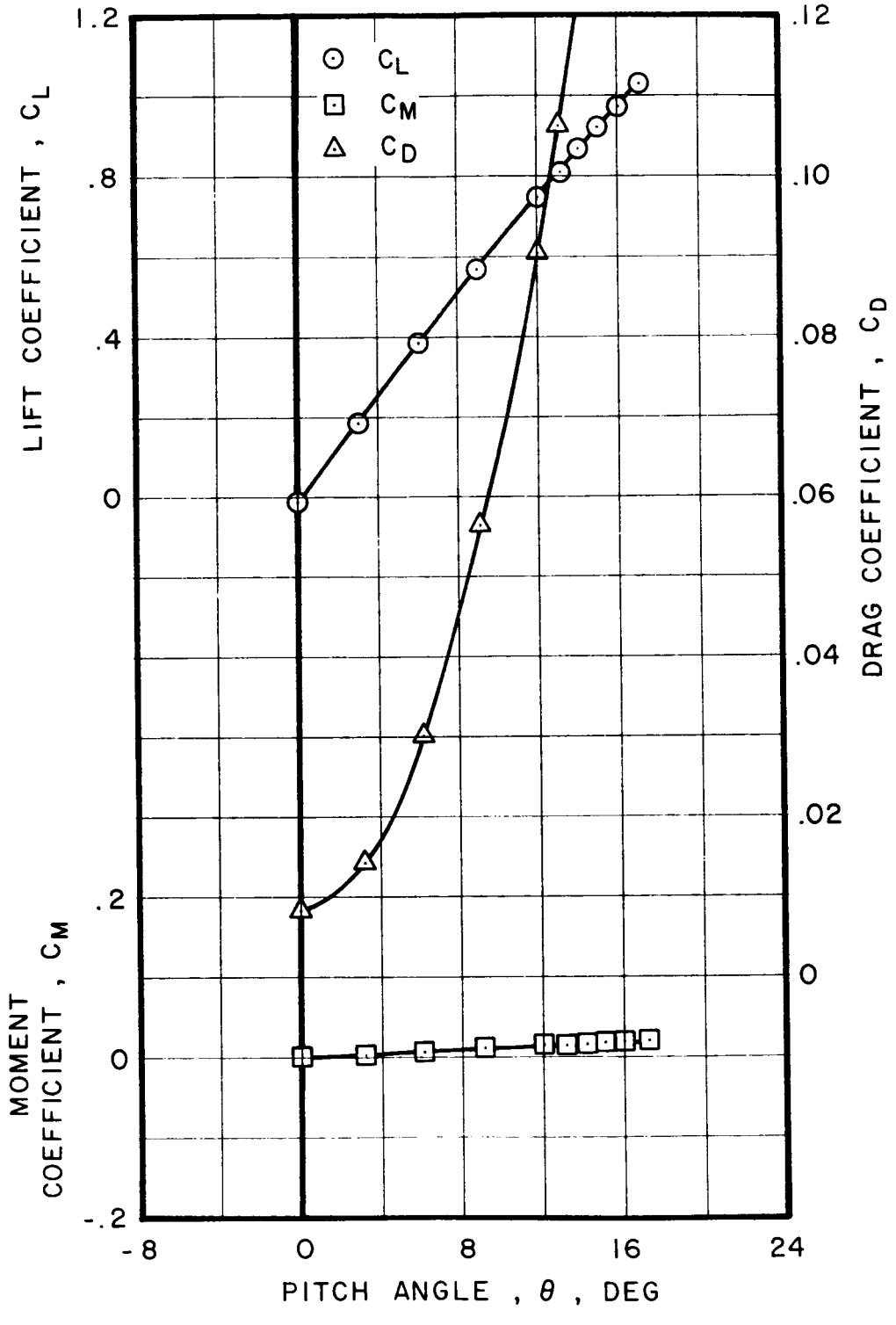

Figure 16. Large Rectangular Tip Aerodynamic Force Coefficients as a Function of Model Pitch Angle, Mach Number = 0.2

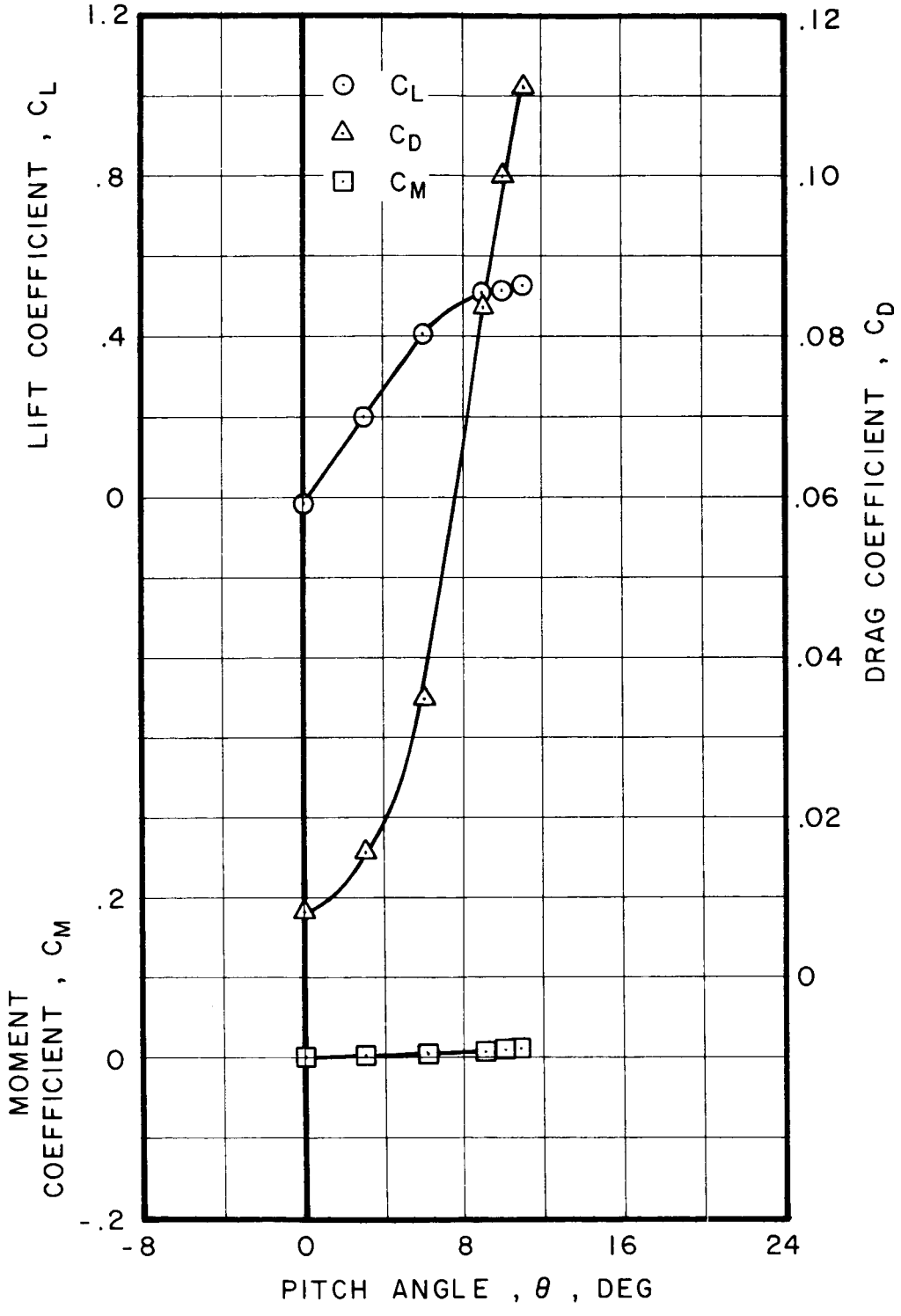

Figure 17. Large Rectangular Tip Aerodynamic Force Coefficients as a Function of Model Pitch Angle, Mach Number = 0.5

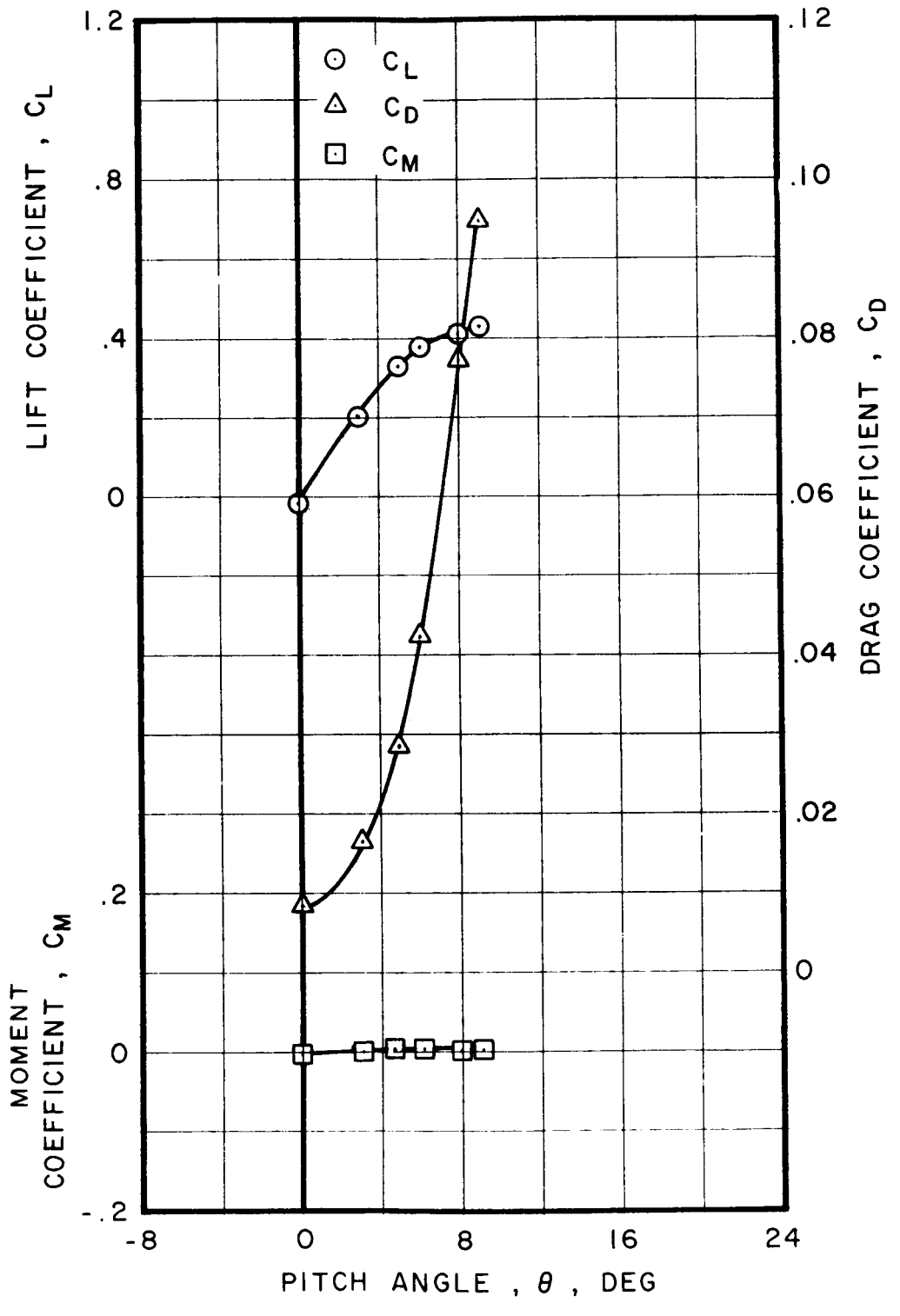

Figure 18. Large Rectangular Tip Aerodynamic Force Coefficients as a Function of Model Pitch Angle, Mach Number = 0.6

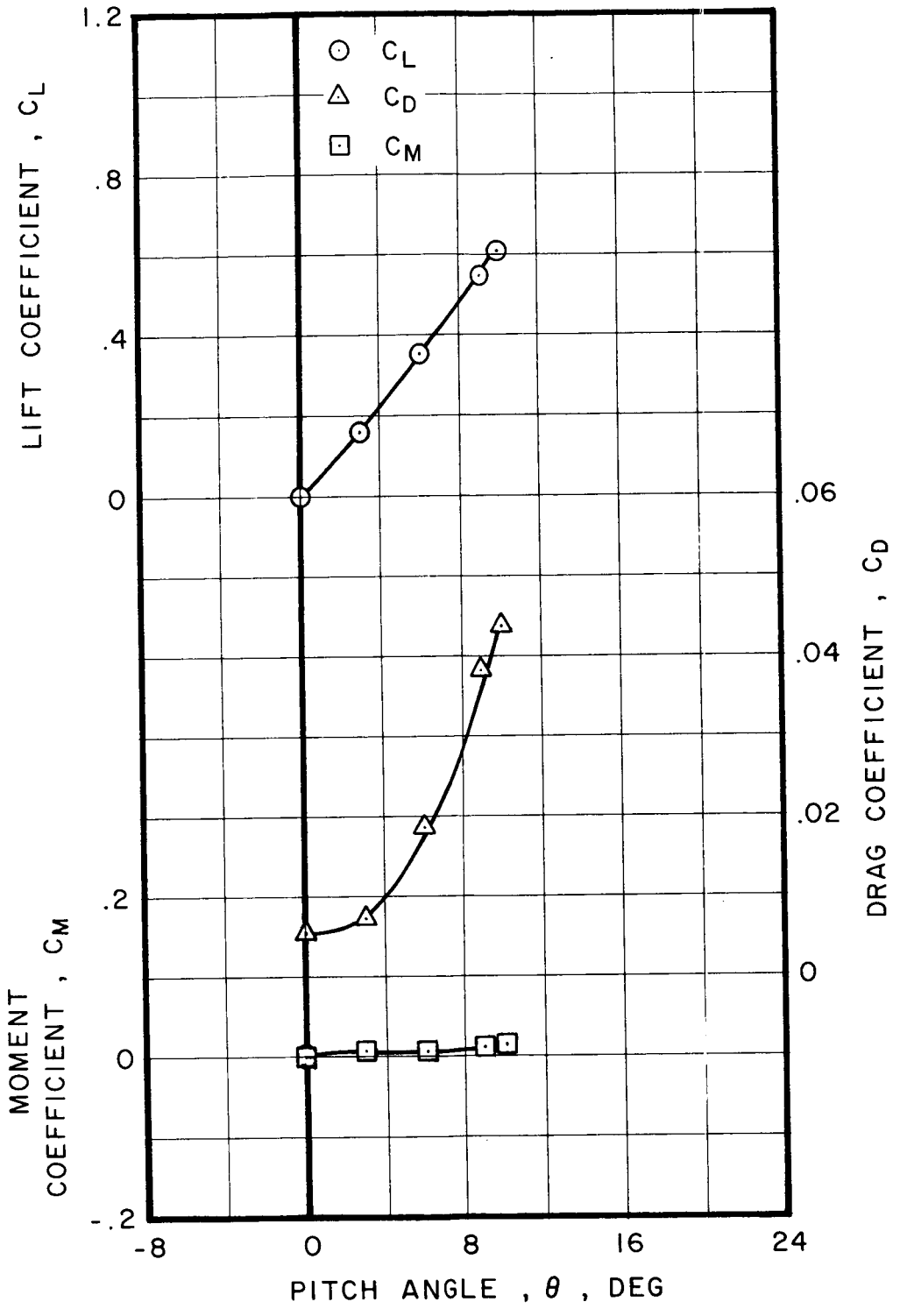

Figure 19. Small Rectangular Tip Aerodynamic Force Coefficients as a Function of Model Pitch Angle, Mach Number = 0.2

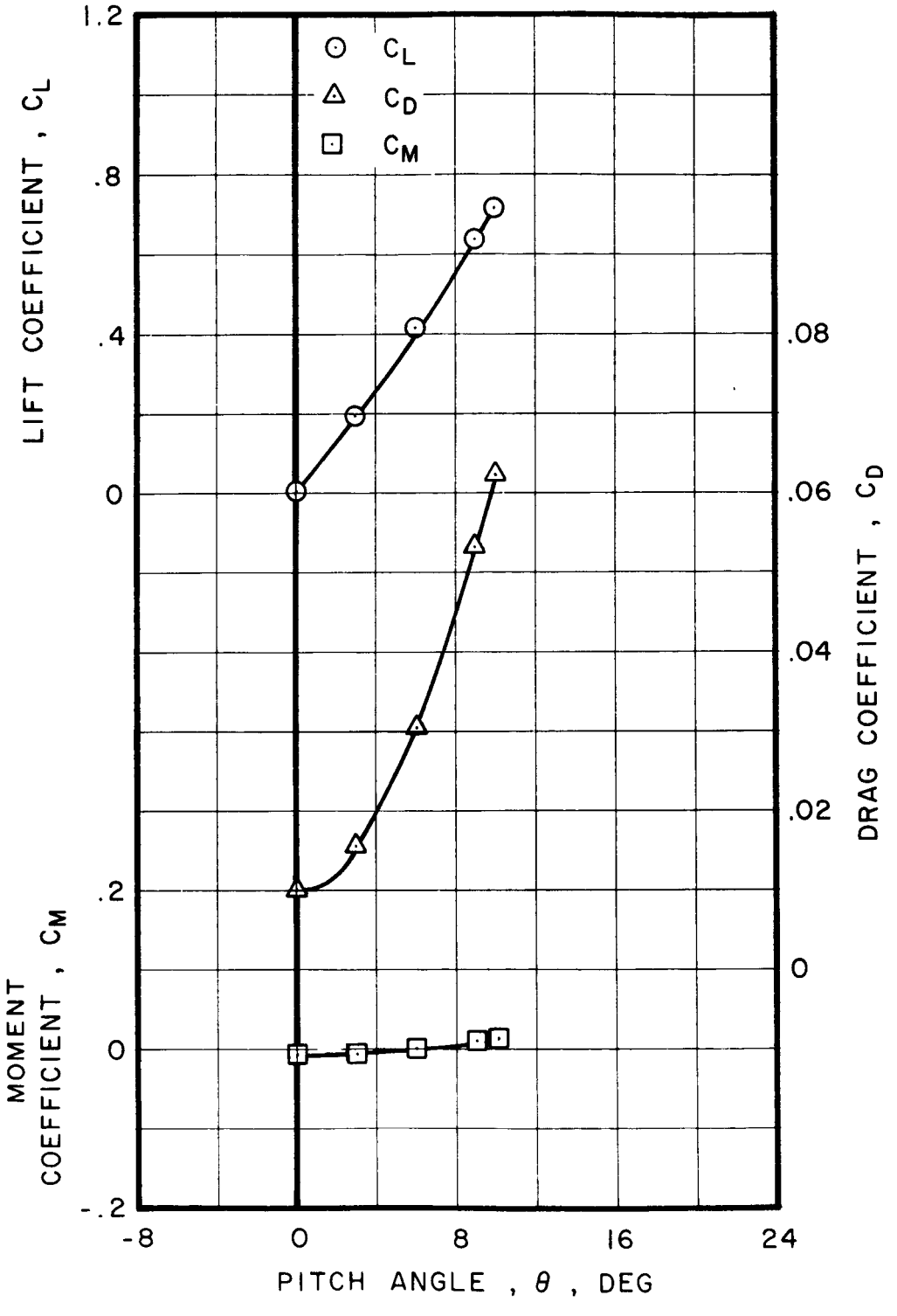

Figure 20. Small Rectangular Tip Aerodynamic Force Coefficients as a Function of Model Pitch Angle, Mach Number = 0.5

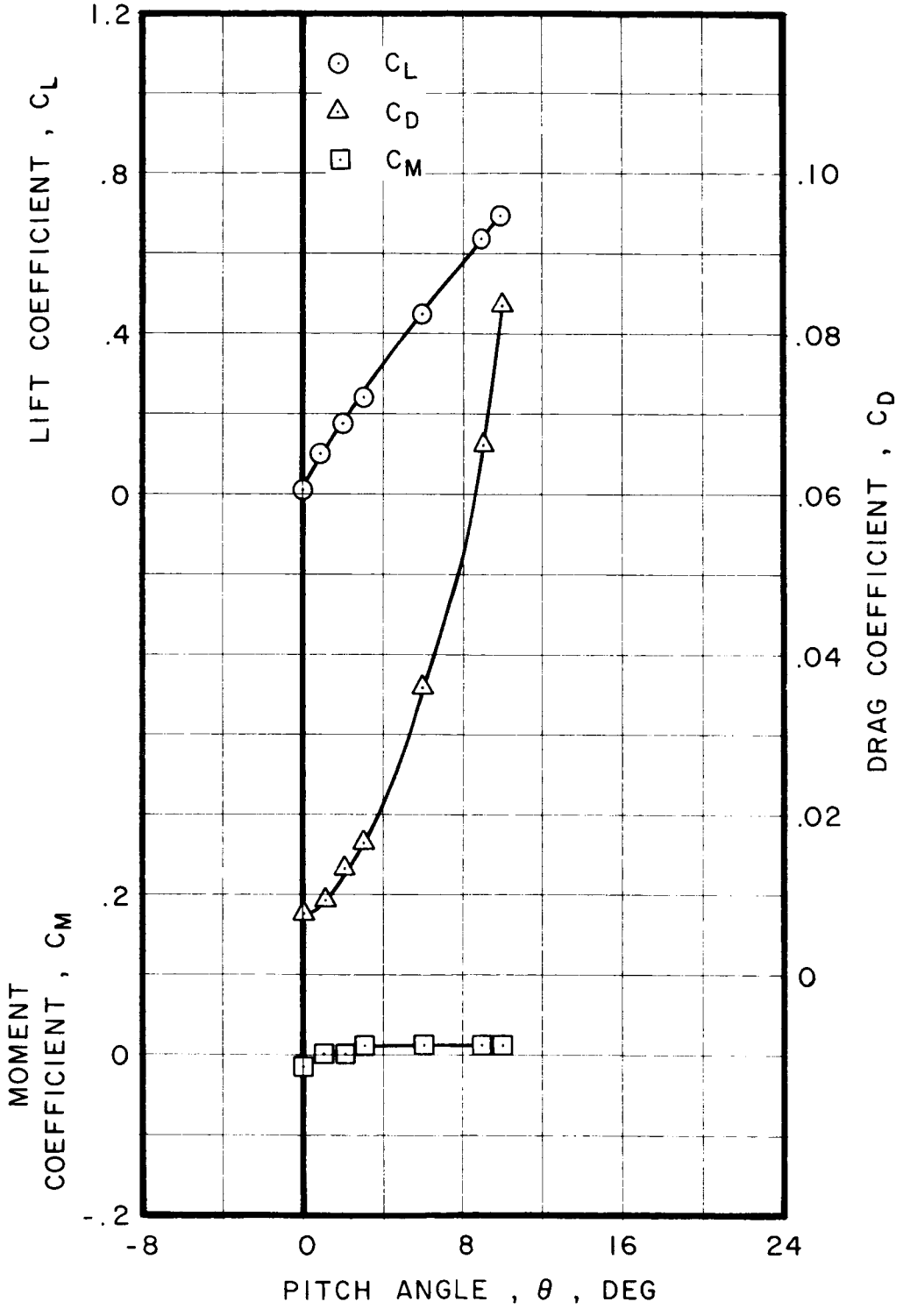

Figure 21. Small Rectangular Tip Aerodynamic Force Coefficients as a Function of Model Pitch Angle, Mach Number = 0.6

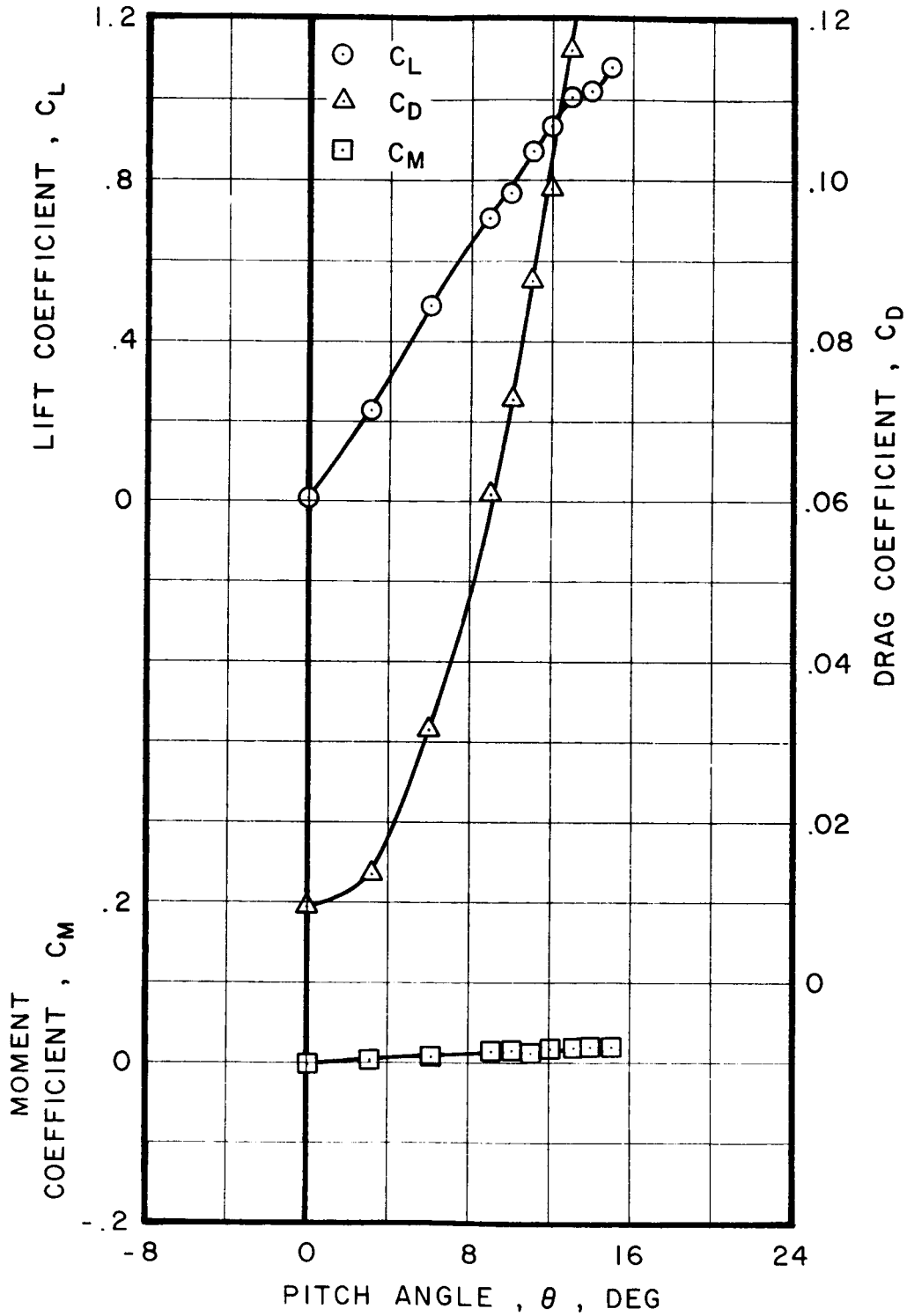

Figure 22. Ogee Tip Aerodynamic Force Coefficients as a Function of Model Pitch Angle, Mach Number = 0.2

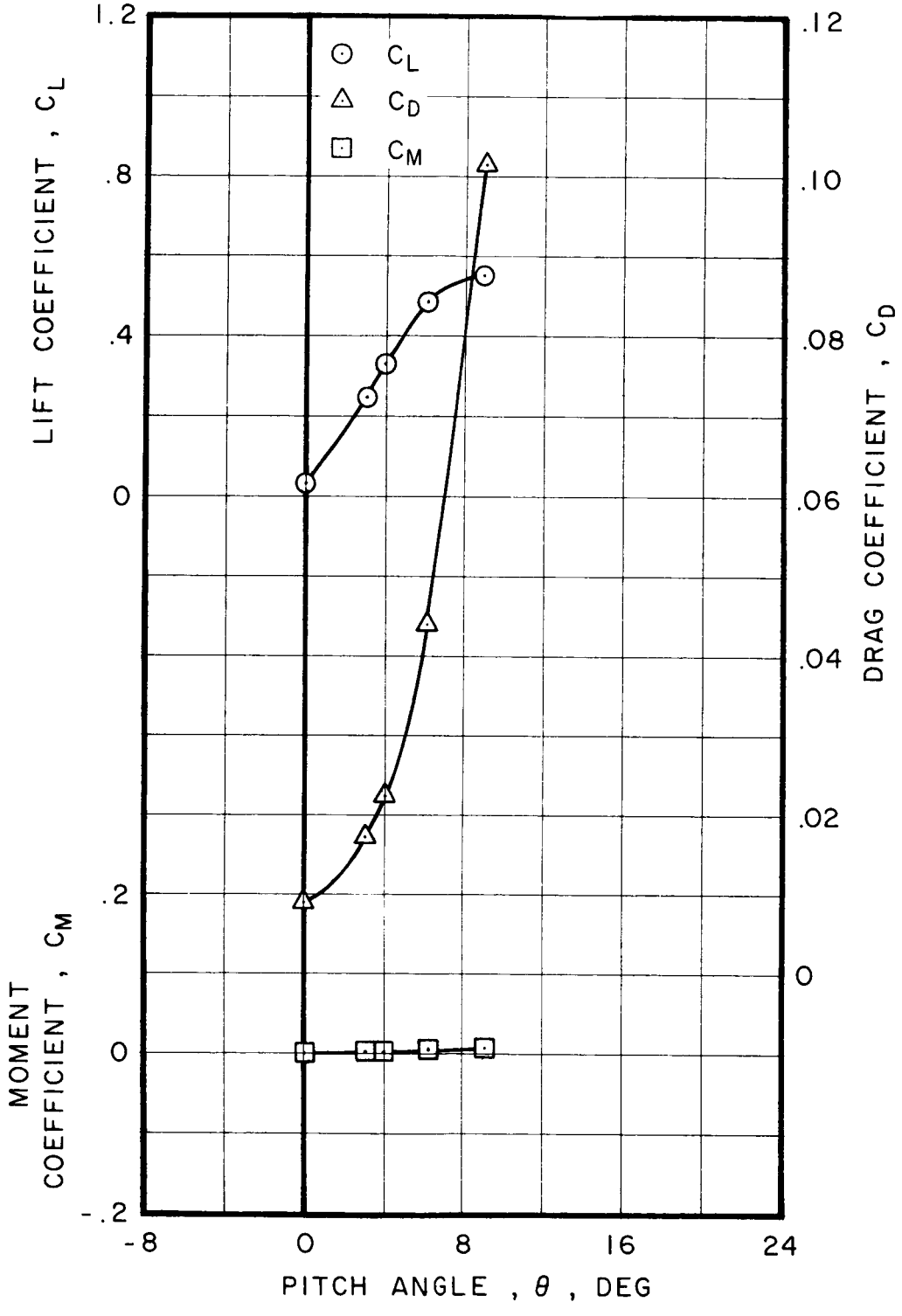

Figure 23. Ogee Tip Aerodynamic Force Coefficients as a Function of Model Pitch Angle, Mach Number = 0.5

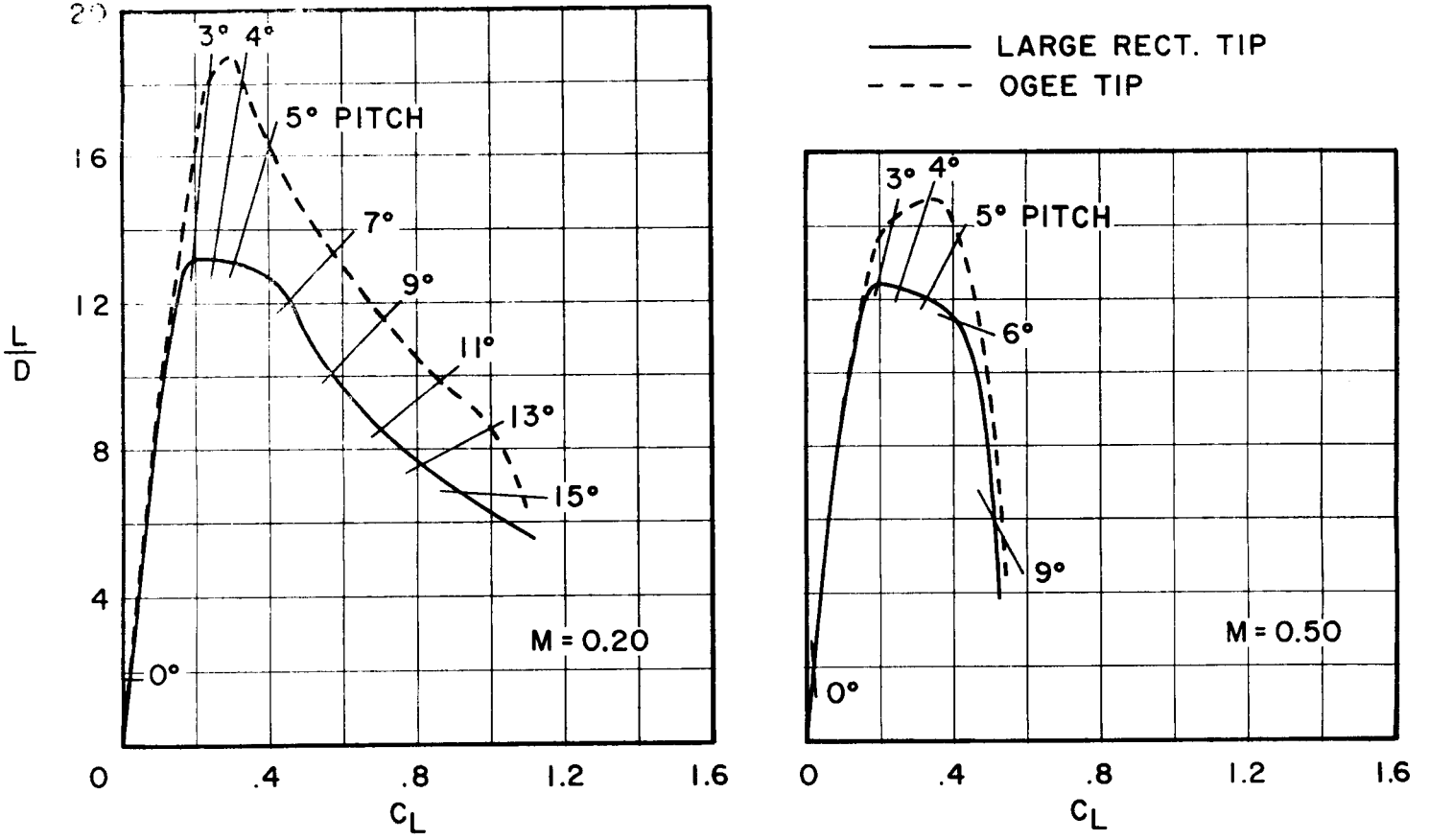

Figure 24. Comparison of Lift/Drag Ratio vs. Lift Coefficient for the Ogee and Large Rectangular Tip at Mach Numbers of 0.2 and 0.5

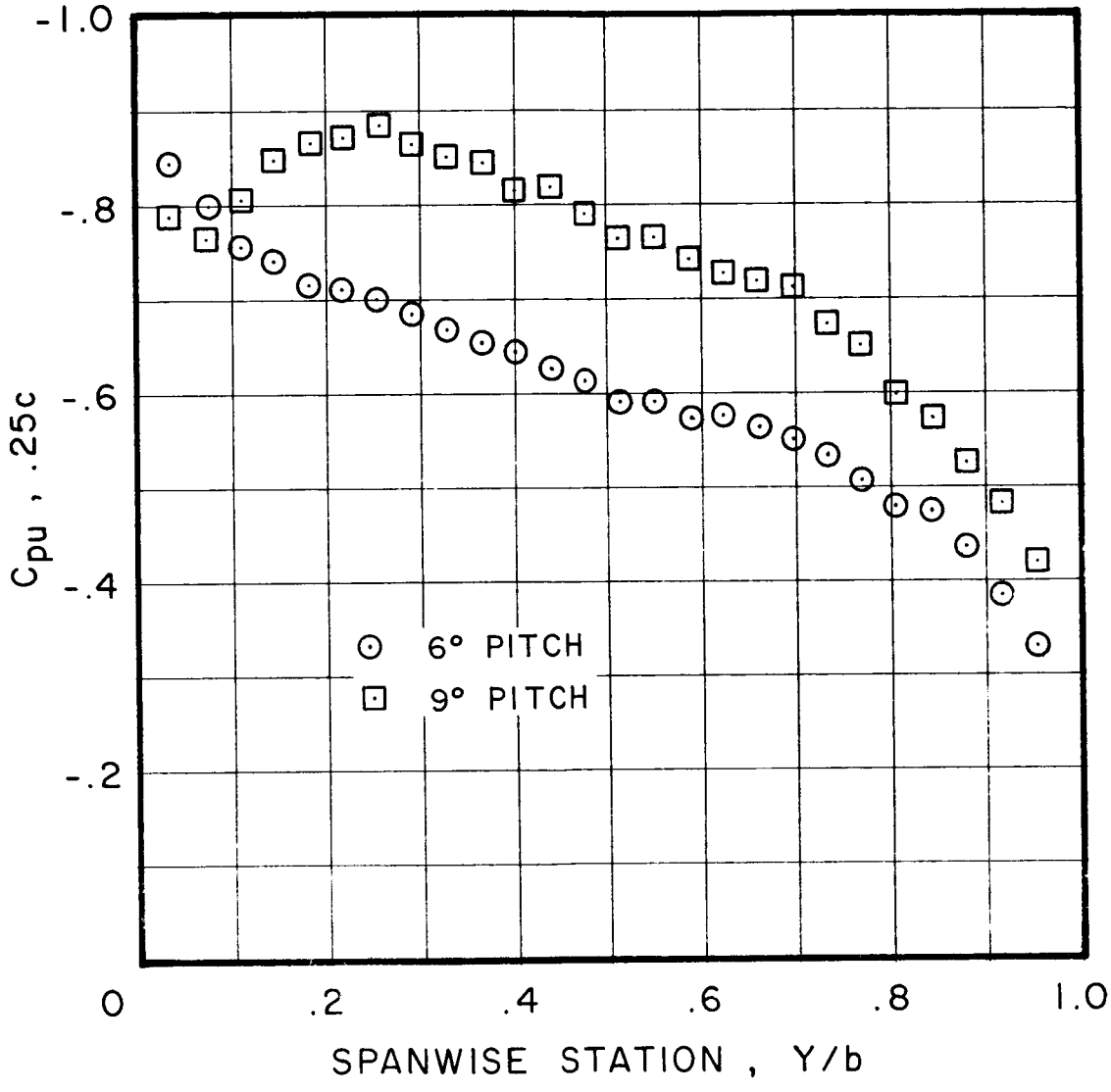

Figure 25. Large Rectangular Tip Spanwise Pressure Distribution at Upper Surface Quarter Chord, Pitch Angle = 6 and 9 Deg. Mach Number = 0.2

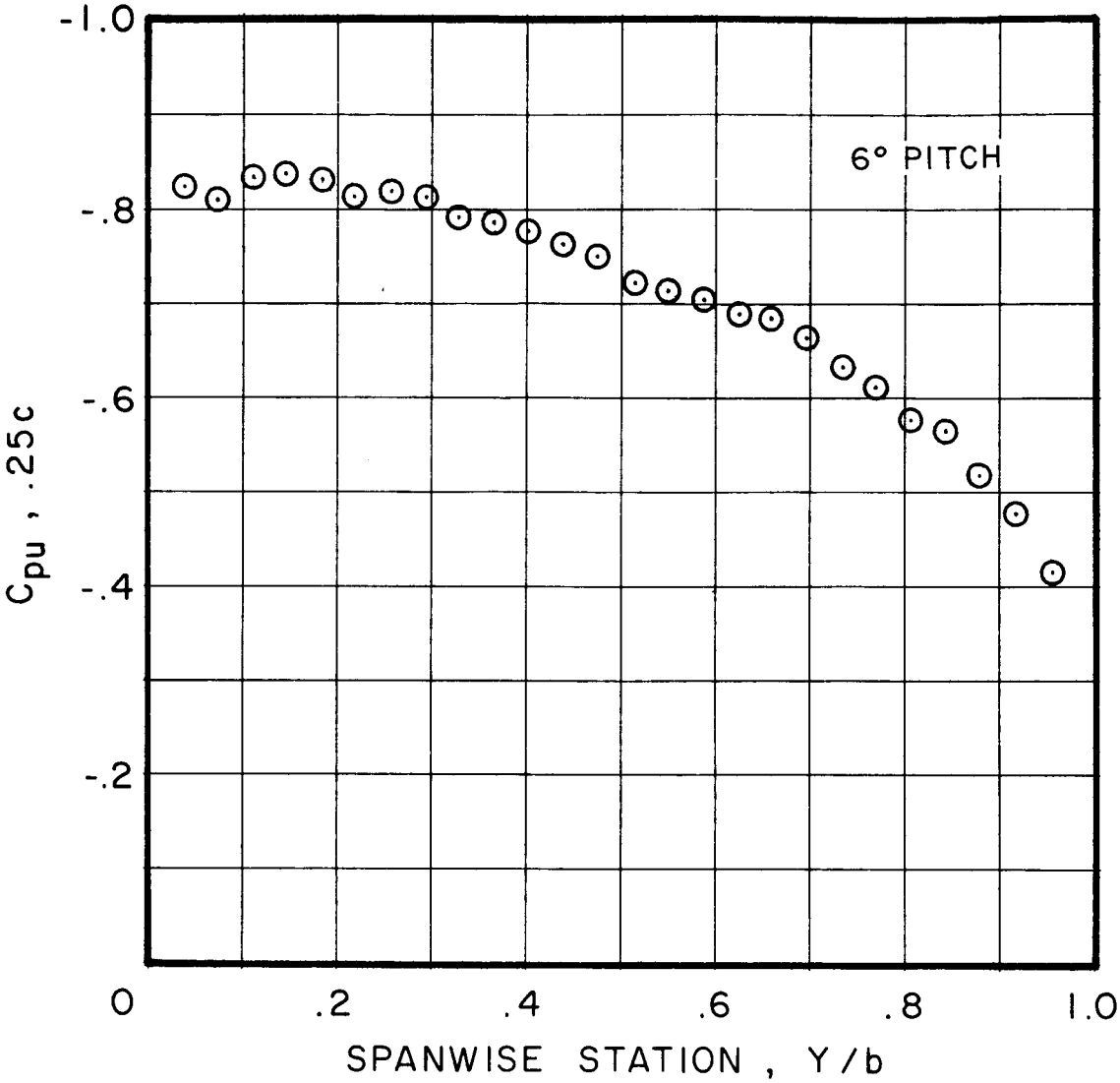

Figure 26. Large Rectangular Tip Spanwise Pressure Distribution at Upper Surface Quarter Chord Pitch Angle = 6 Deg. Mach Number = 0.5

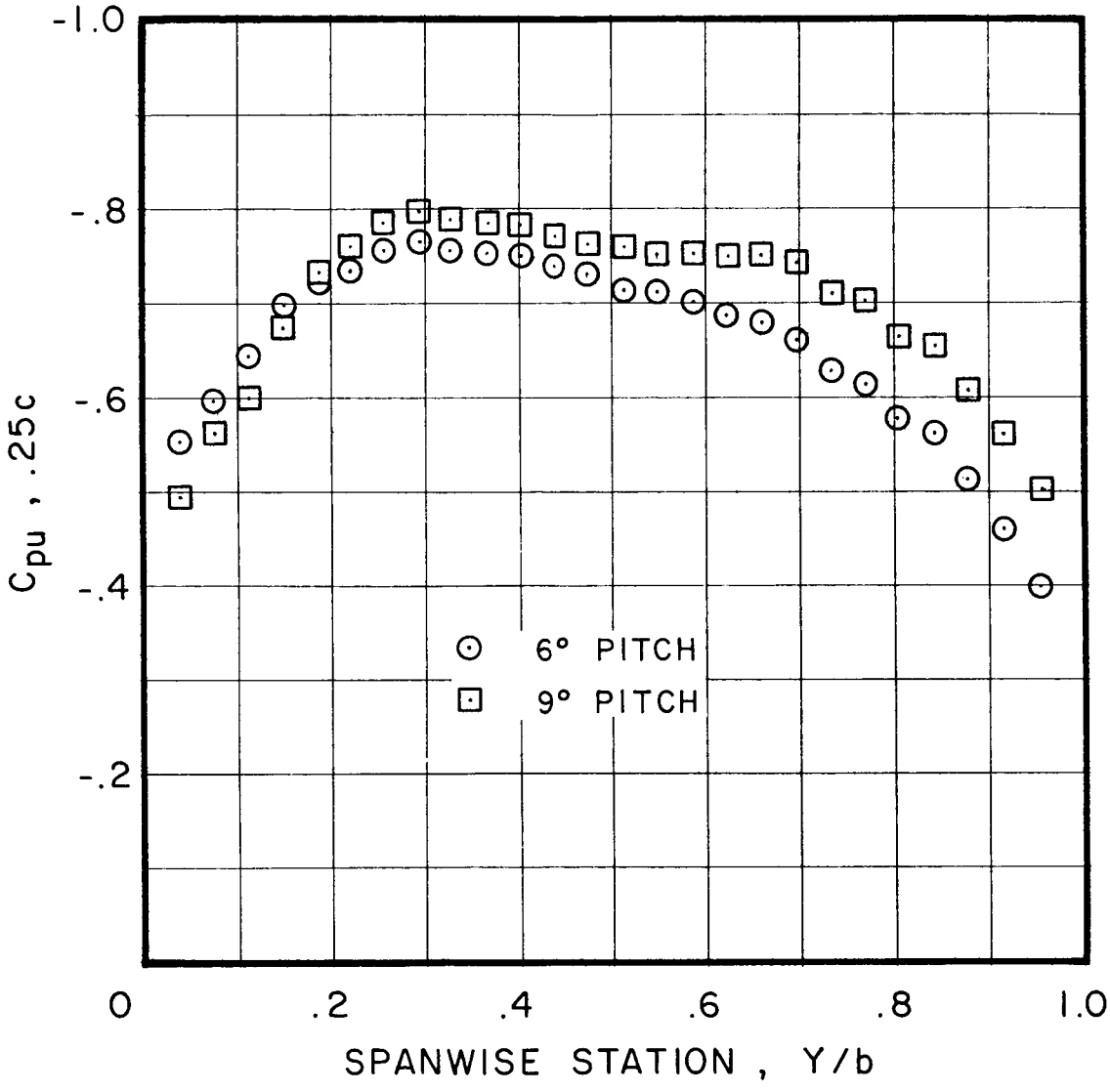

Figure 27. Large Rectangular Tip CP Distribution at Upper Surface Quarter Chord, Pitch Angle = 6 and 9 Deg. Mach Number = 0.6.

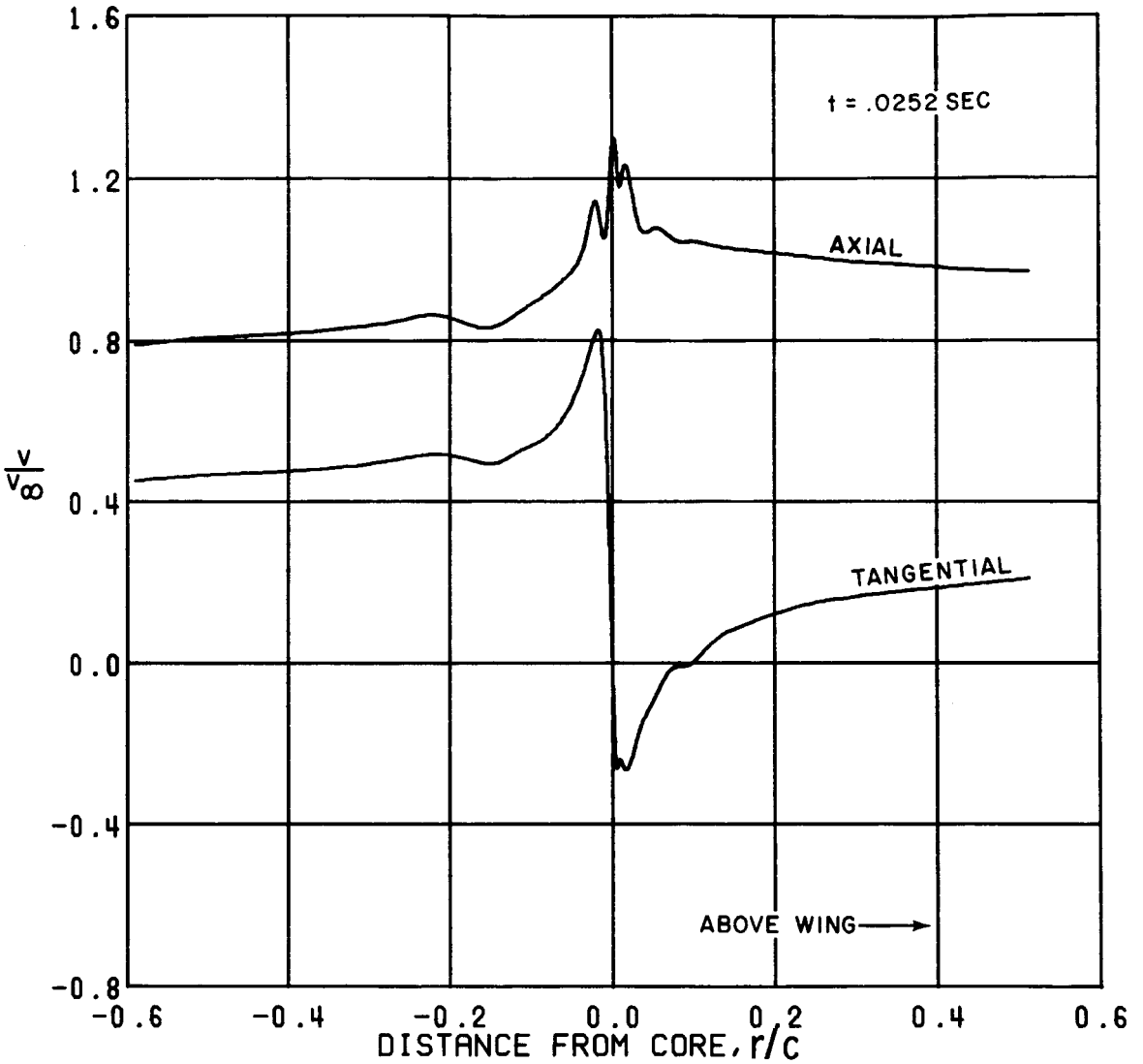

FIGURE 28. LARGE RECT. TIP, VORTEX VELOCITY DISTRIBUTIONS

2.0 CHORD LENGTHS FROM TRAILING EDGE
TRAVERSE NORMAL TO SPAN
MACH 0.20 6.0 DEG PITCH
REYNOLDS NUMBER = 2 000 000.
FREE STREAM VELOCITY = 72. M/SEC = 237. FT/SEC

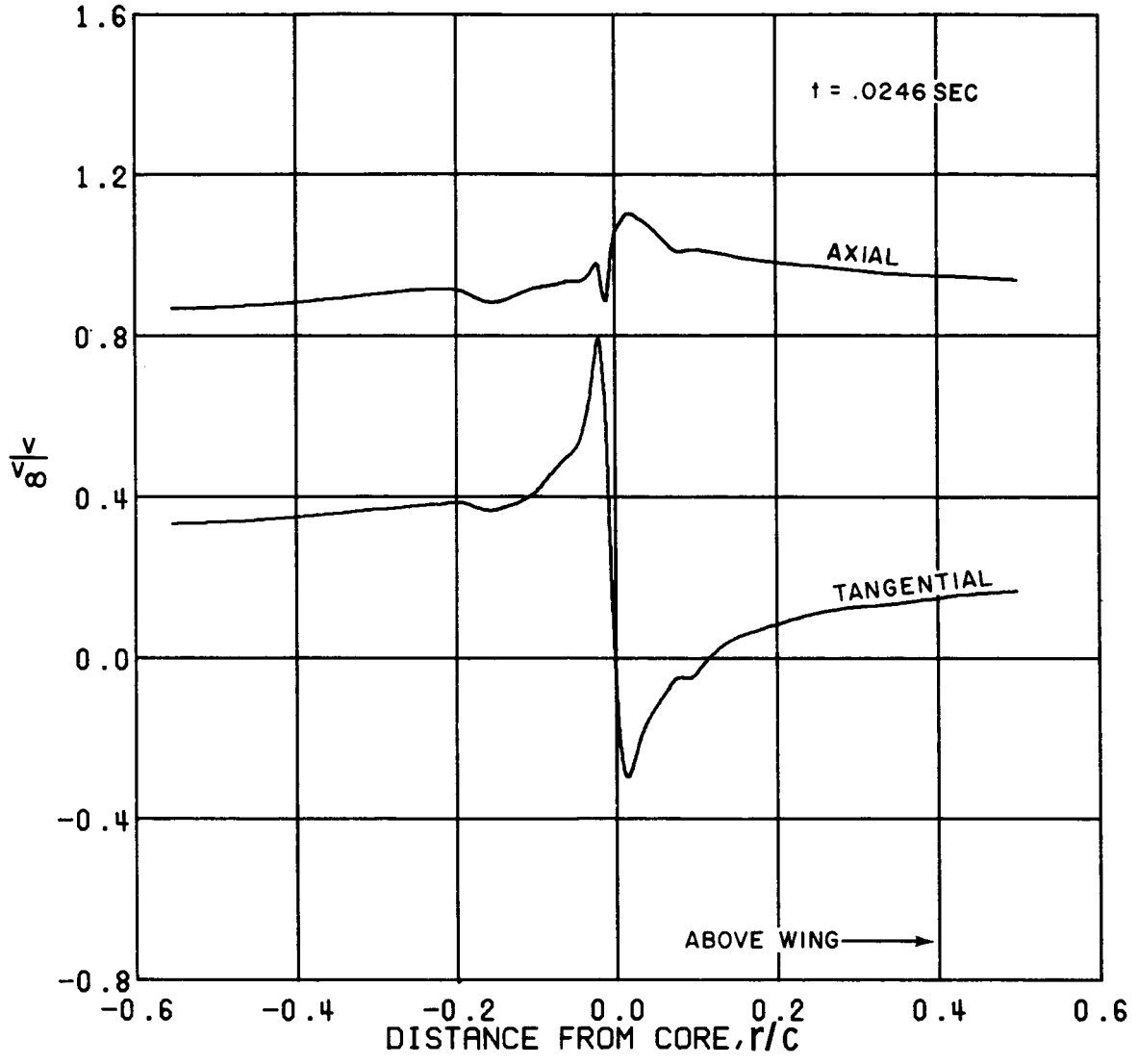

FIGURE 29. LARGE RECT. TIP, VORTEX VELOCITY DISTRIBUTIONS

2.0 CHORD LENGTHS FROM TRAILING EDGE
TRAVERSE NORMAL TO SPAN
MACH 0.20 6.0 DEG PITCH
REYNOLDS NUMBER = 2 800 000.
FREE STREAM VELOCITY = 74. M/SEC = 242. FT/SEC

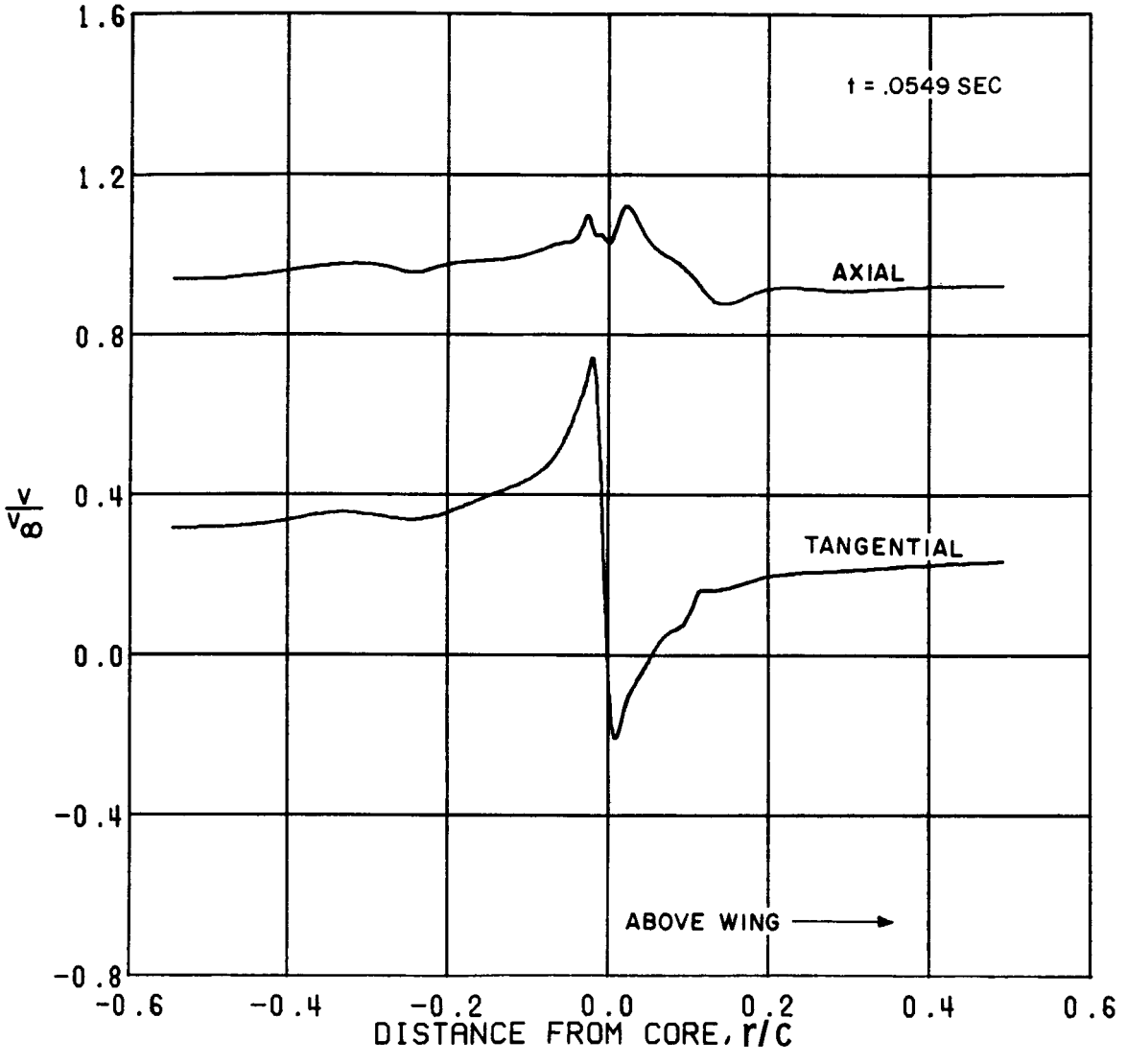

FIGURE 30. LARGE RECT. TIP, VORTEX VELOCITY DISTRIBUTIONS

6.0 CHORD LENGTHS FROM TRAILING EDGE
TRAVERSE NORMAL TO SPAN
MACH 0.20 8.0 DEG PITCH
REYNOLDS NUMBER = 2 000 000.
FREE STREAM VELOCITY = 71. M/SEC = 232. FT/SEC

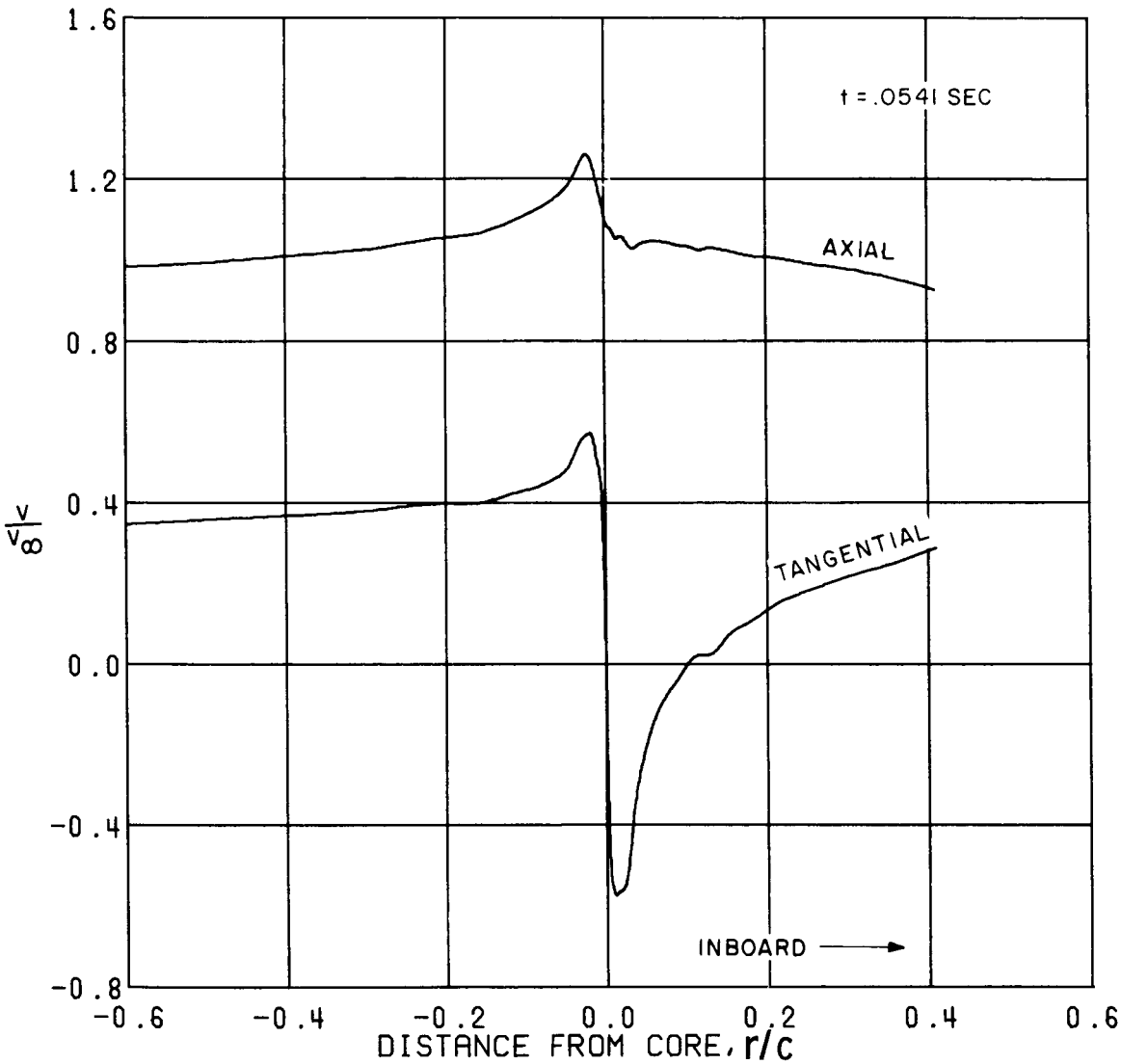

FIGURE 31. LARGE RECT. TIP, VORTEX VELOCITY DISTRIBUTIONS

5.0 CHORD LENGTHS FROM TRAILING EDGE
TRAVERSE PARALLEL TO SPAN
MACH 0.20 6.0 DEG PITCH
REYNOLDS NUMBER = 2 700 000.
FREE STREAM VELOCITY = 70. M/SEC = 230. FT/SEC

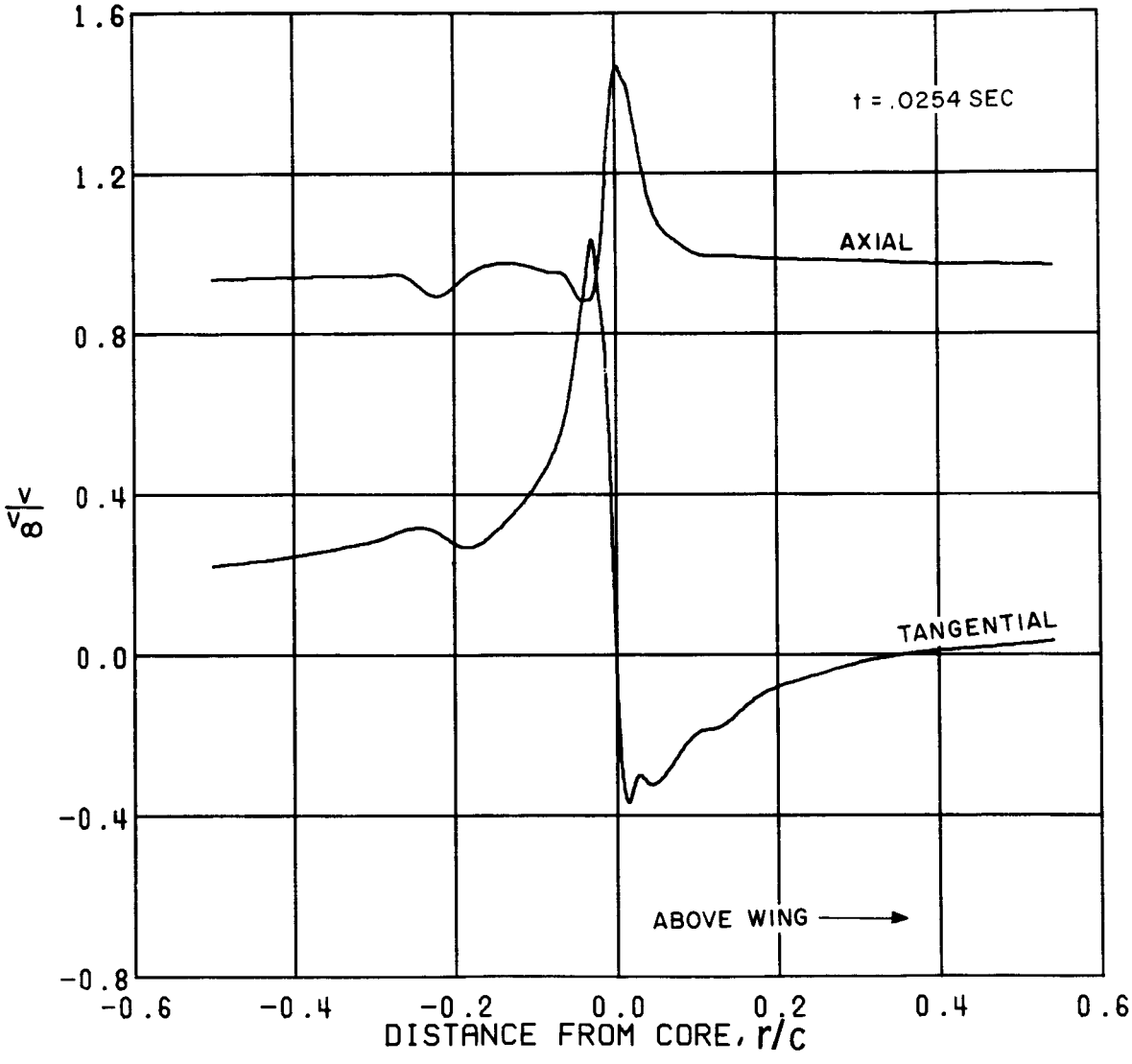

FIGURE 32. LARGE RECT. TIP, VORTEX VELOCITY DISTRIBUTIONS

2.0 CHORD LENGTHS FROM TRAILING EDGE
TRAVERSE NORMAL TO SPAN
MACH 0.20 9.8 DEG PITCH
REYNOLDS NUMBER = 2 800 000.
FREE STREAM VELOCITY = 71. M/SEC = 234. FT/SEC

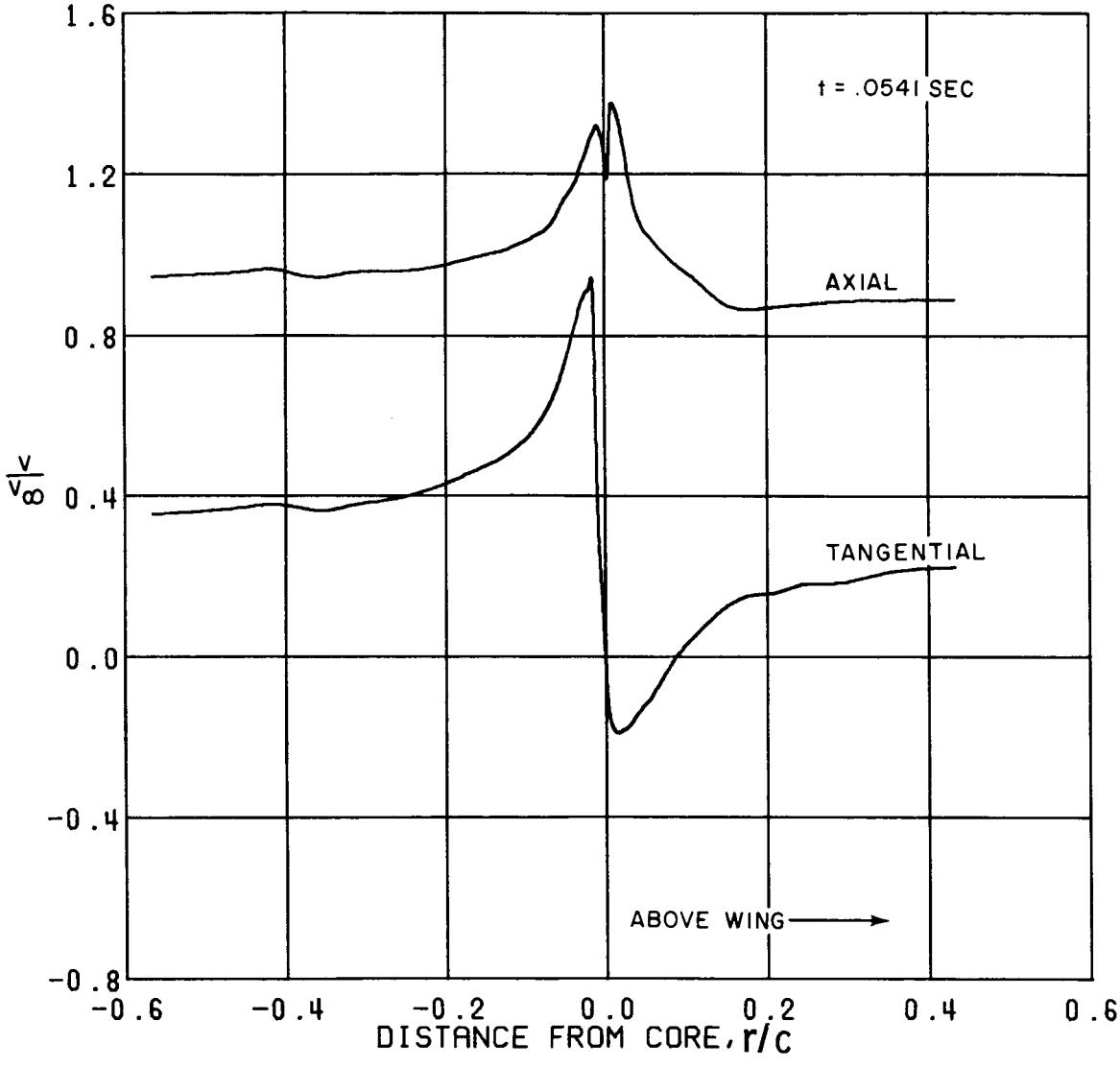

FIGURE 33. LARGE RECT. TIP, VORTEX VELOCITY DISTRIBUTIONS

5.0 CHORD LENGTHS FROM TRAILING EDGE
TRAVERSE NORMAL TO SPAN
MACH 0.20 9.0 DEG PITCH
REYNOLDS NUMBER = 2 700 000.
FREE STREAM VELOCITY = 70. M/SEC = 230. FT/SEC

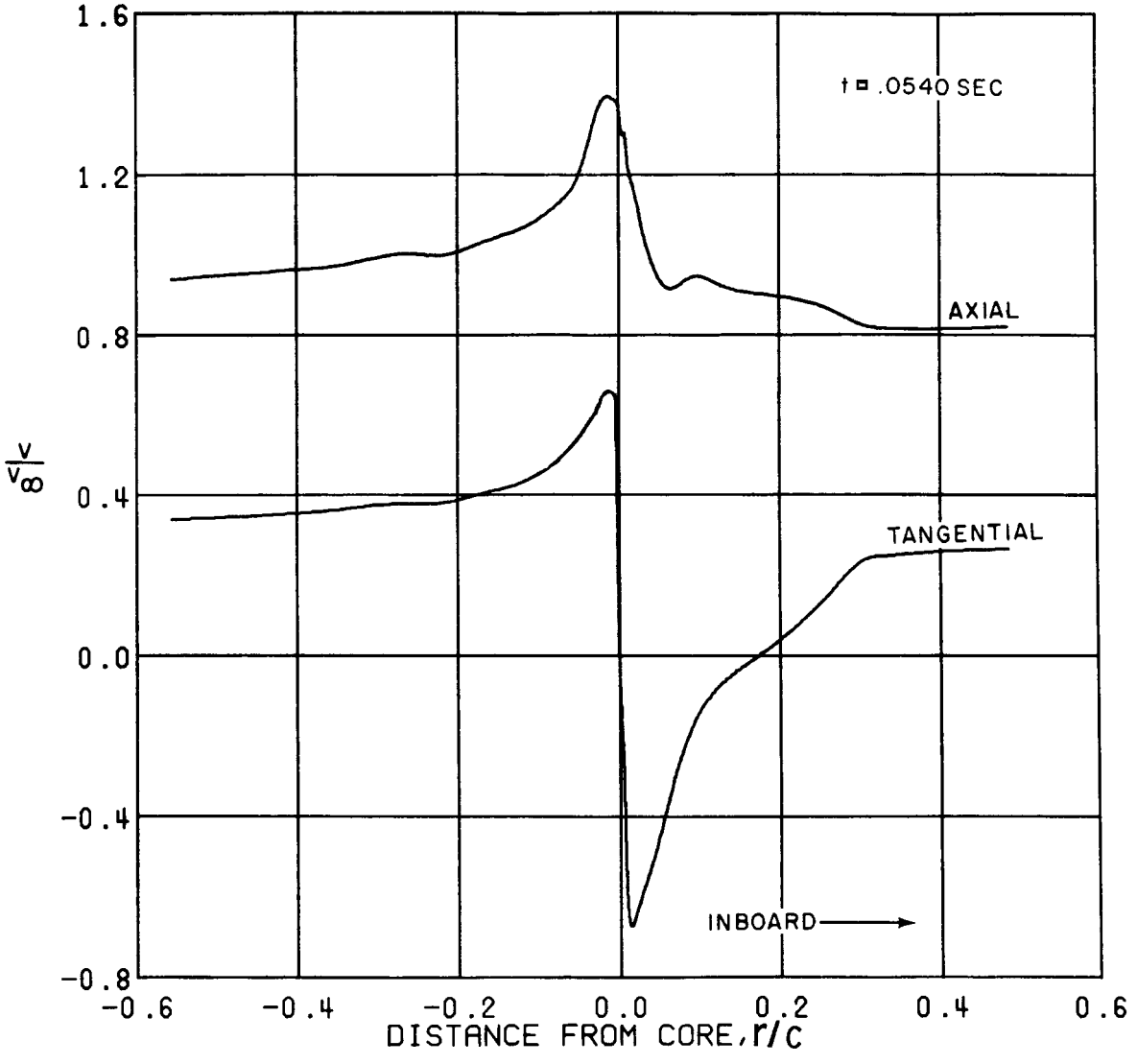

FIGURE 34. LARGE RECT. TIP, VORTEX VELOCITY DISTRIBUTIONS

5.0 CHORD LENGTHS FROM TRAILING EDGE
TRAVERSE PARALLEL TO SPAN
MACH 0.20 9.0 DEG PITCH
REYNOLDS NUMBER = 2 700 000.
FREE STREAM VELOCITY = 70. M/SEC = 231. FT/SEC

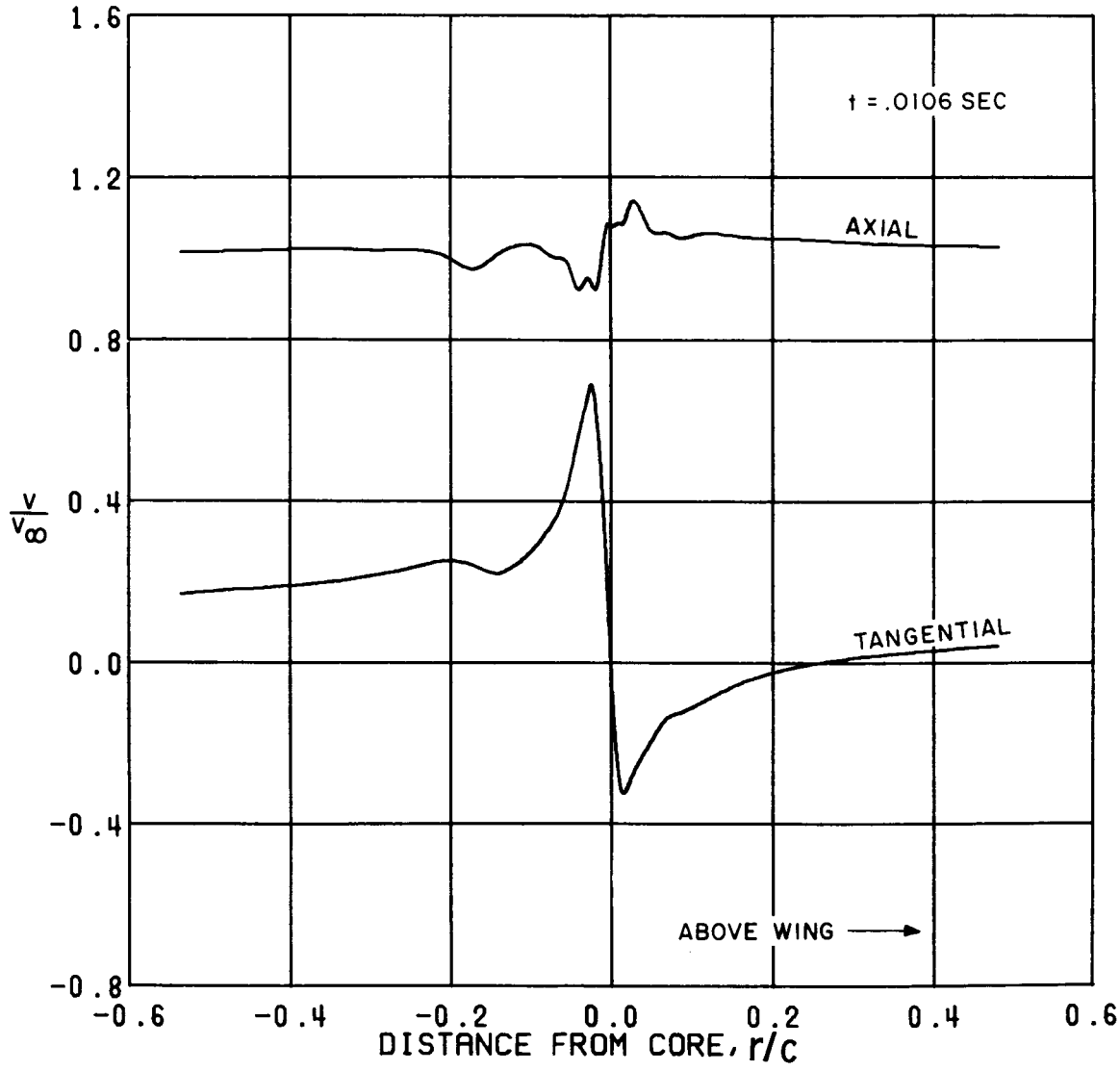

FIGURE 35. LARGE RECT. TIP, VORTEX VELOCITY DISTRIBUTIONS

2.0 CHORD LENGTHS FROM TRAILING EDGE
TRAVERSE NORMAL TO SPAN
MACH 0.50 6.0 DEG PITCH
REYNOLDS NUMBER = 6 000 000.
FREE STREAM VELOCITY = 171. M/SEC = 562. FT/SEC

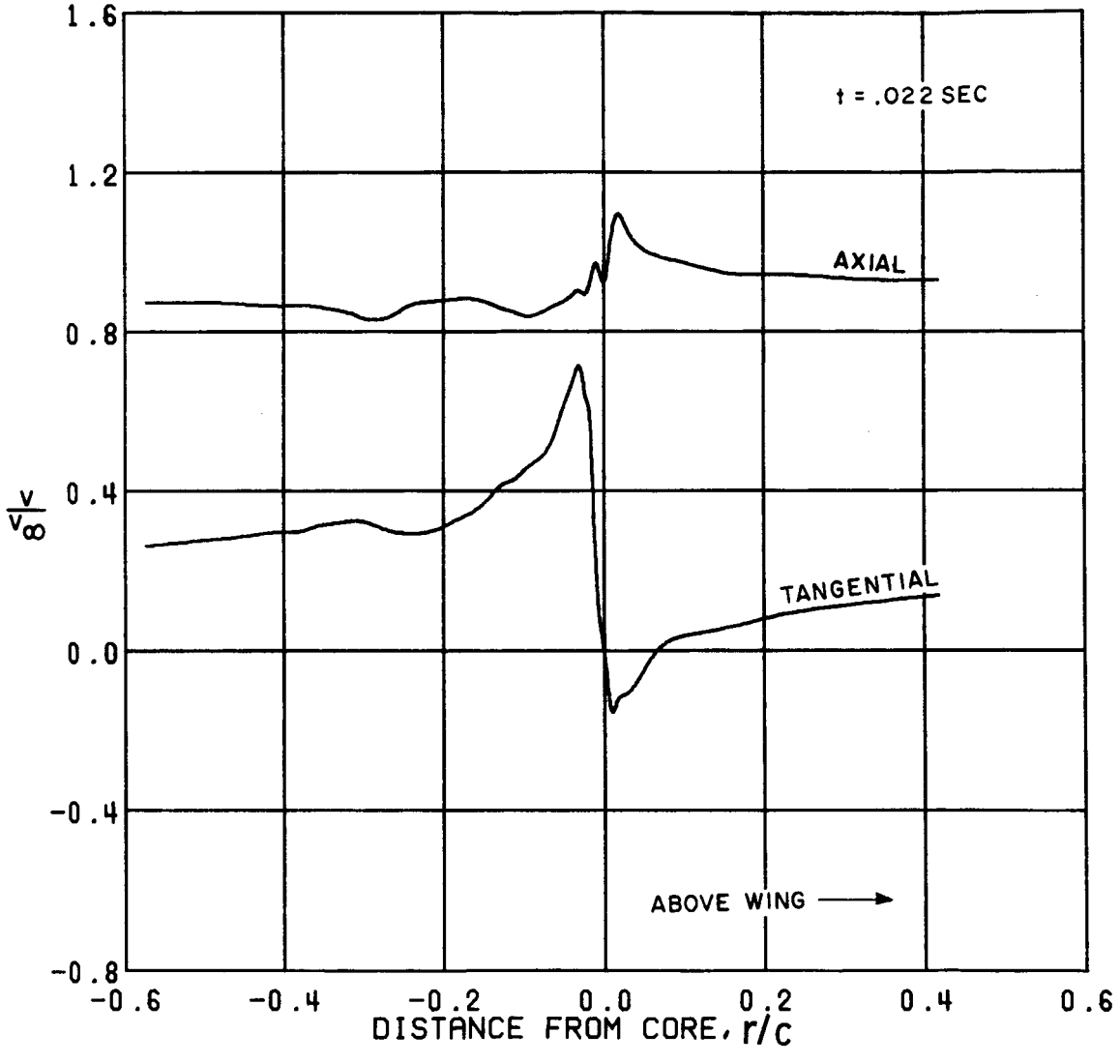

FIGURE 36. LARGE RECT. TIP, VORTEX VELOCITY DISTRIBUTIONS

5.0 CHORD LENGTHS FROM TRAILING EDGE
TRAVERSE NORMAL TO SPAN
MACH 0.80 6.0 DEG PITCH
REYNOLDS NUMBER = 6 000 000.
FREE STREAM VELOCITY = 173. M/SEC = 567. FT/SEC

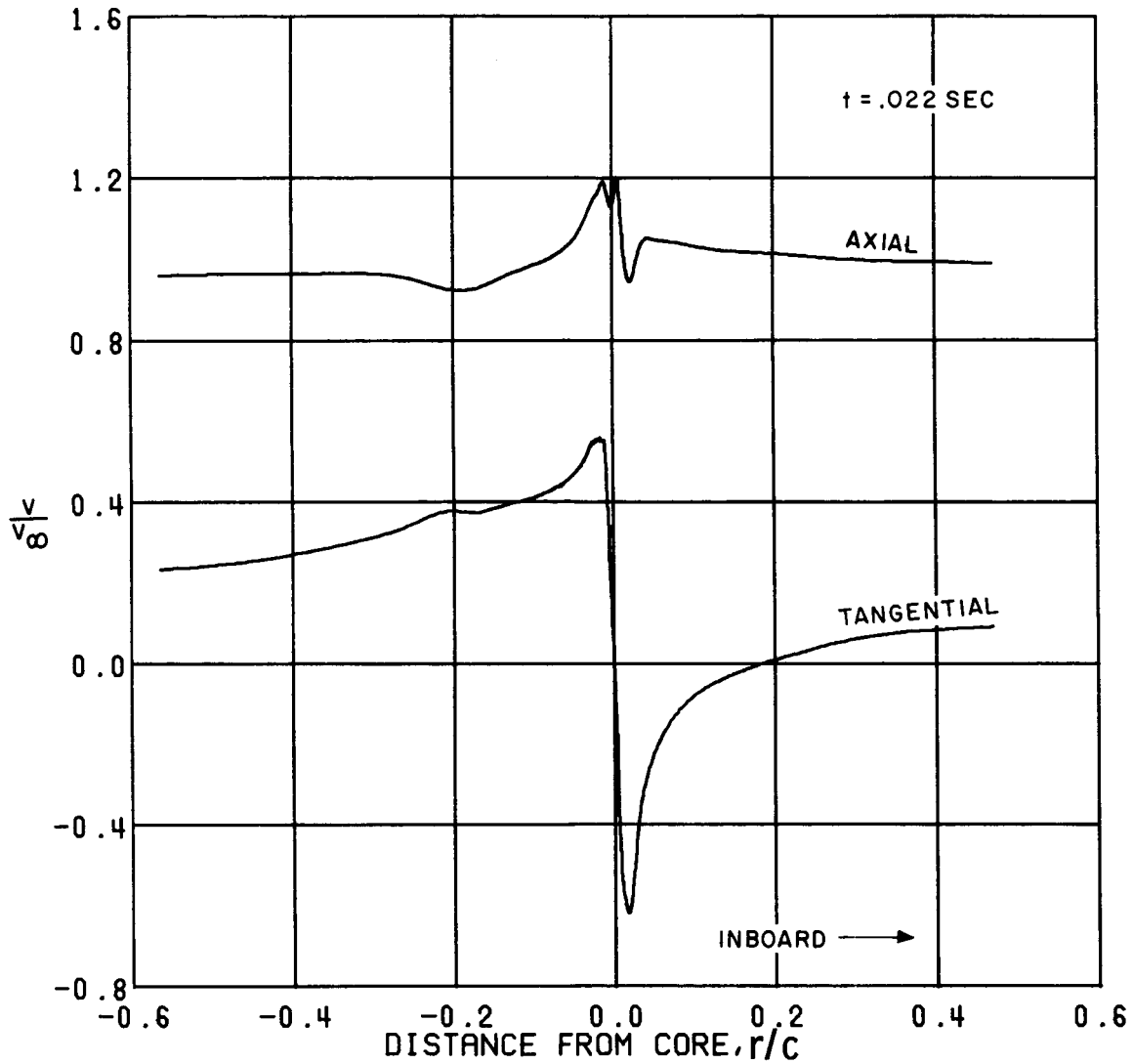

FIGURE 37. LARGE RECT. TIP, VORTEX VELOCITY DISTRIBUTIONS

5.0 CHORD LENGTHS FROM TRAILING EDGE
TRAVERSE PARALLEL TO SPAN
MACH 0.50 6.0 DEG PITCH
REYNOLDS NUMBER = 6 100 000.
FREE STREAM VELOCITY = 174. M/SEC = 569. FT/SEC

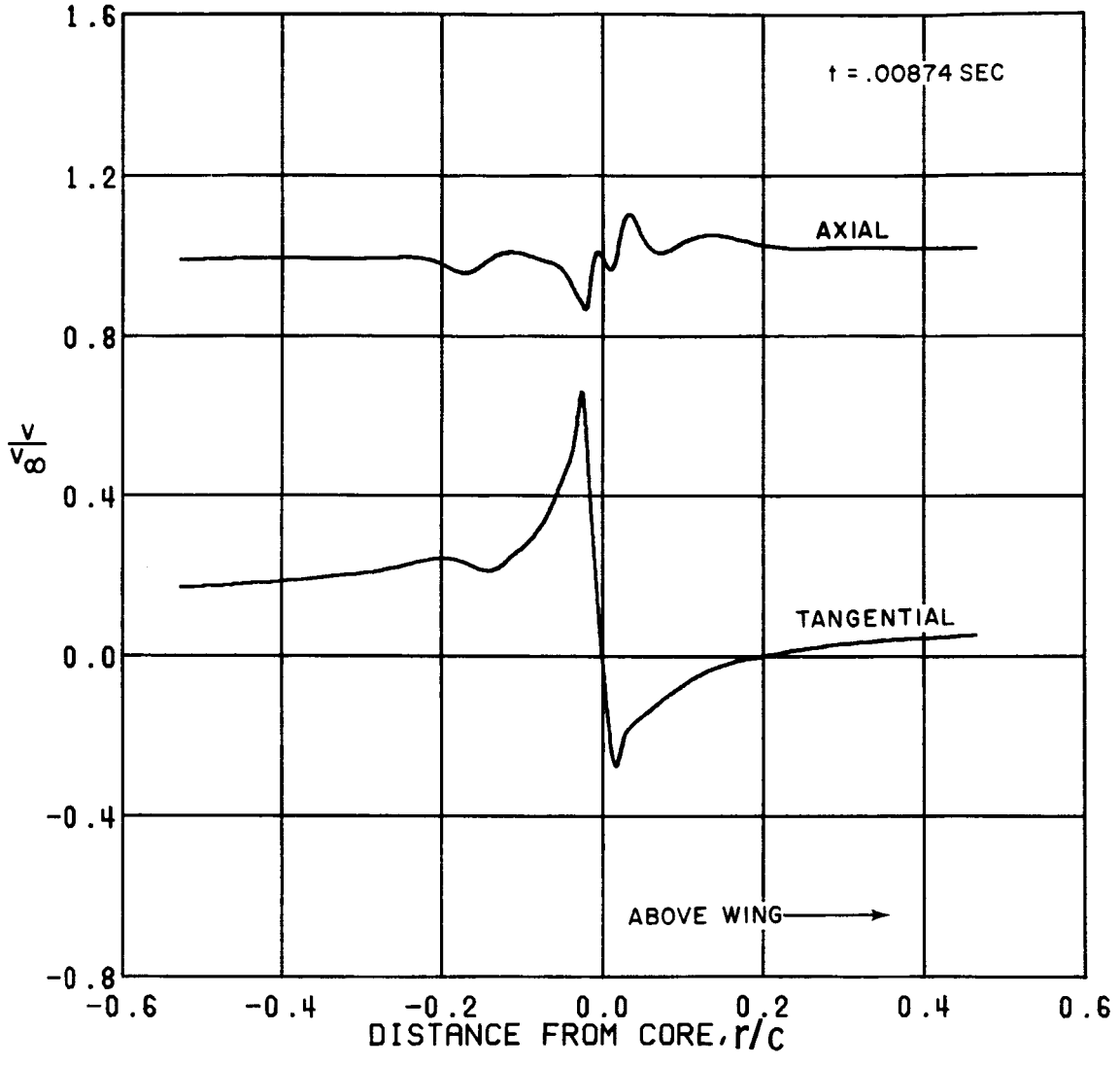

FIGURE 38. LARGE RECT. TIP, VORTEX VELOCITY DISTRIBUTIONS

2.0 CHORD LENGTHS FROM TRAILING EDGE
TRAVERSE NORMAL TO SPAN
MACH 0.80 8.0 DEG PITCH
REYNOLDS NUMBER = 6 900 000.
FREE STREAM VELOCITY = 269. M/SEC = 884. FT/SEC

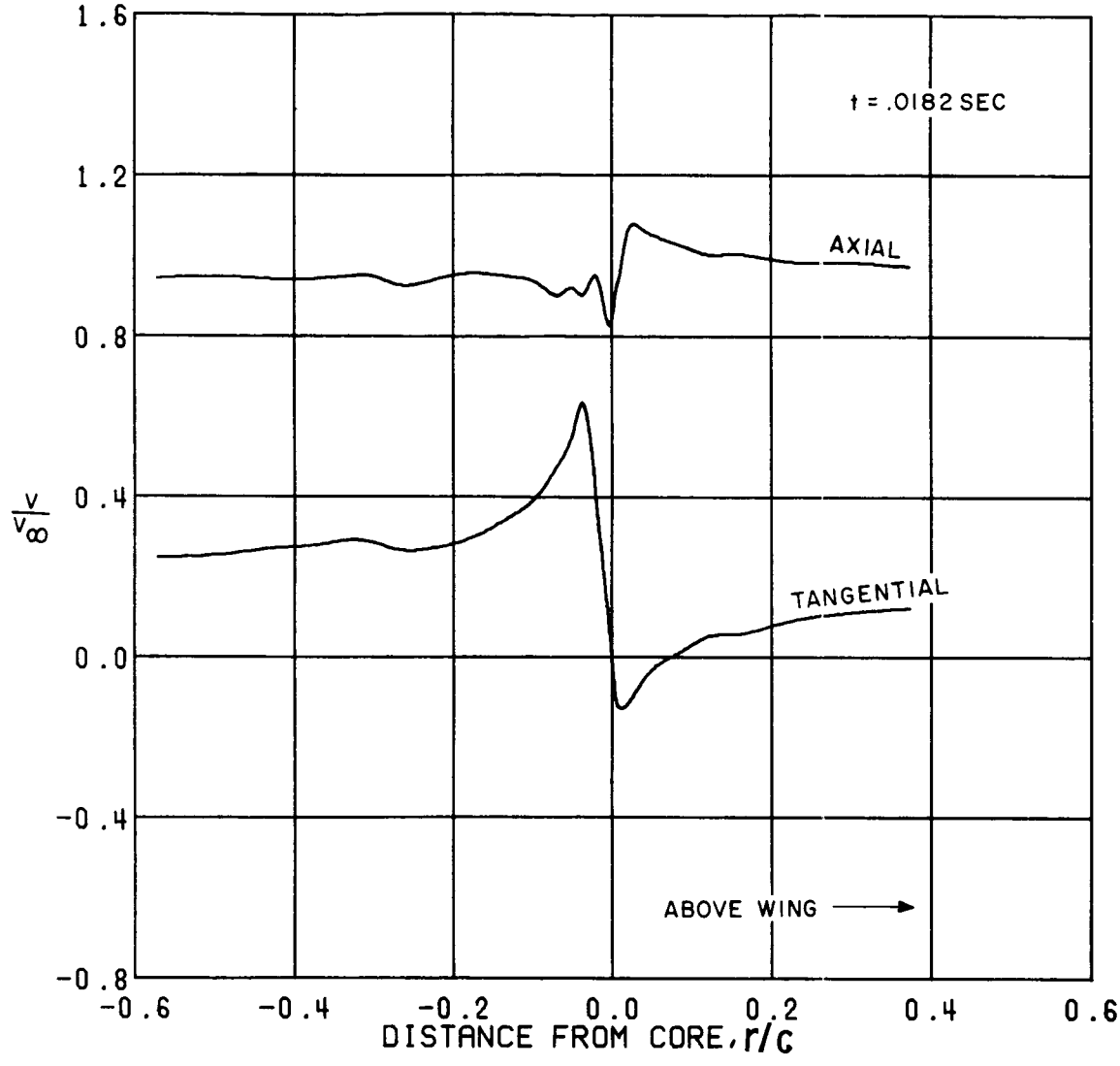

FIGURE 39. LARGE RECT. TIP, VORTEX VELOCITY DISTRIBUTIONS

8.0 CHORD LENGTHS FROM TRAILING EDGE
TRAVERSE NORMAL TO SPAN
MACH 0.60 6.0 DEG PITCH
REYNOLDS NUMBER = 7 000 000.
FREE STREAM VELOCITY = 208. M/SEC = 687. FT/SEC

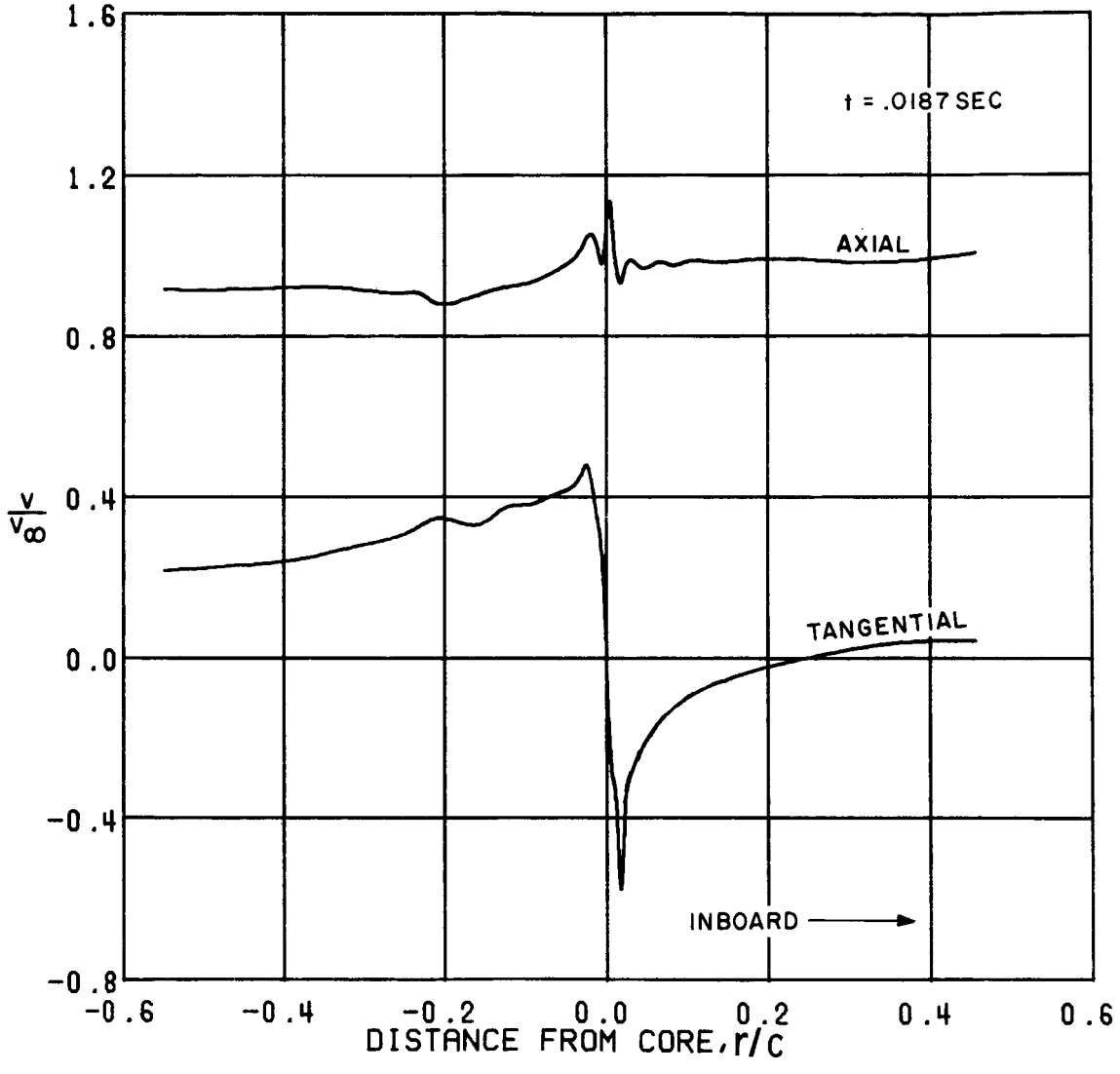

FIGURE 40. LARGE RECT.TIP, VORTEX VELOCITY DISTRIBUTIONS

5.0 CHORD LENGTHS FROM TRAILING EDGE
TRAVERSE PARALLEL TO SPAN
MACH 0.60 6.0 DEG PITCH
REYNOLDS NUMBER = 6 000 000.
FREE STREAM VELOCITY = 204. M/SEC = 668. FT/SEC

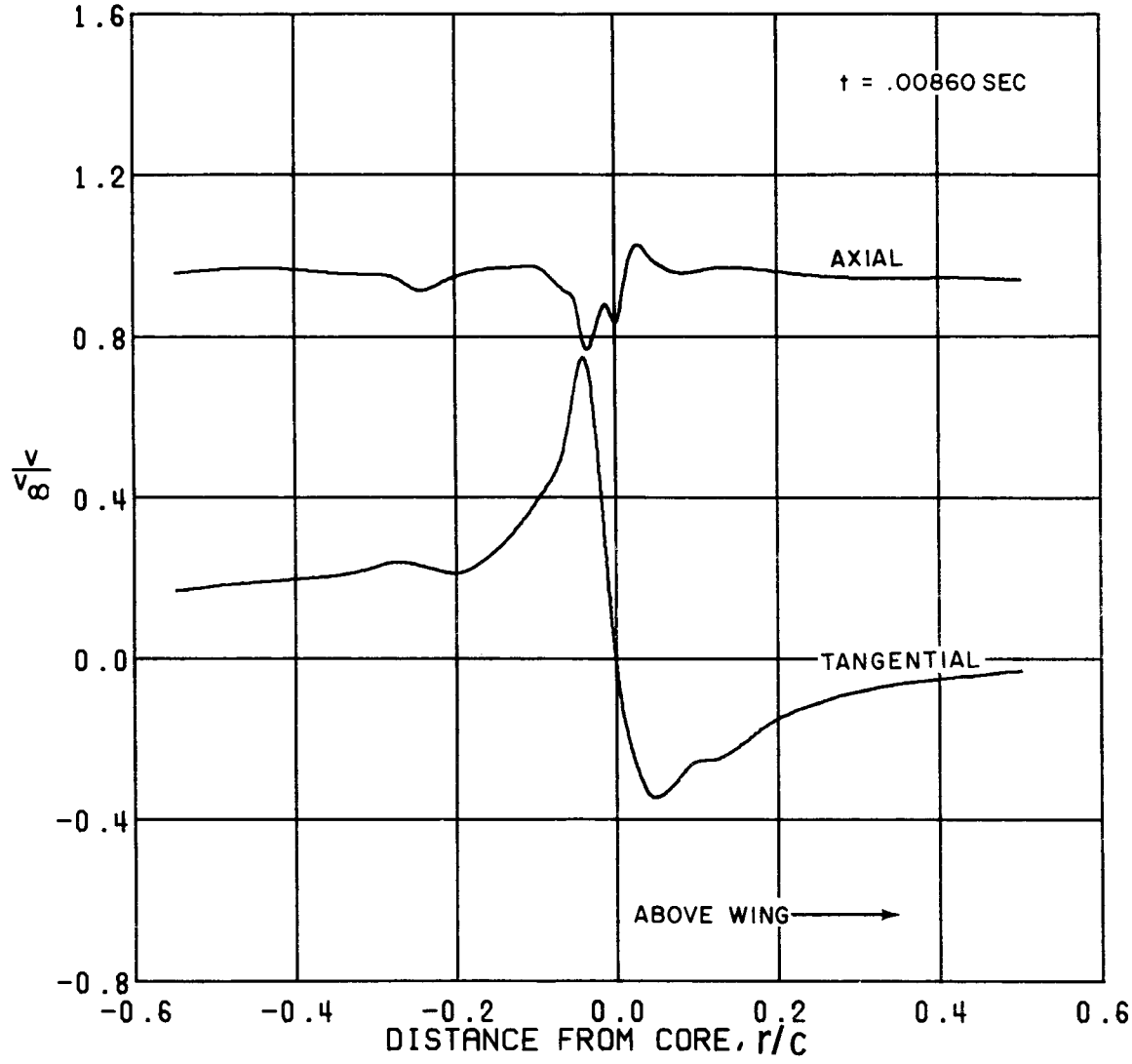

FIGURE 41. LARGE RECT. TIP, VORTEX VELOCITY DISTRIBUTIONS

2.0 CHORD LENGTHS FROM TRAILING EDGE
TRAVERSE NORMAL TO SPAN
MACH 0.60 9.0 DEG PITCH
REYNOLDS NUMBER = 6 000 000.
FREE STREAM VELOCITY = 212. M/SEC = 695. FT/SEC

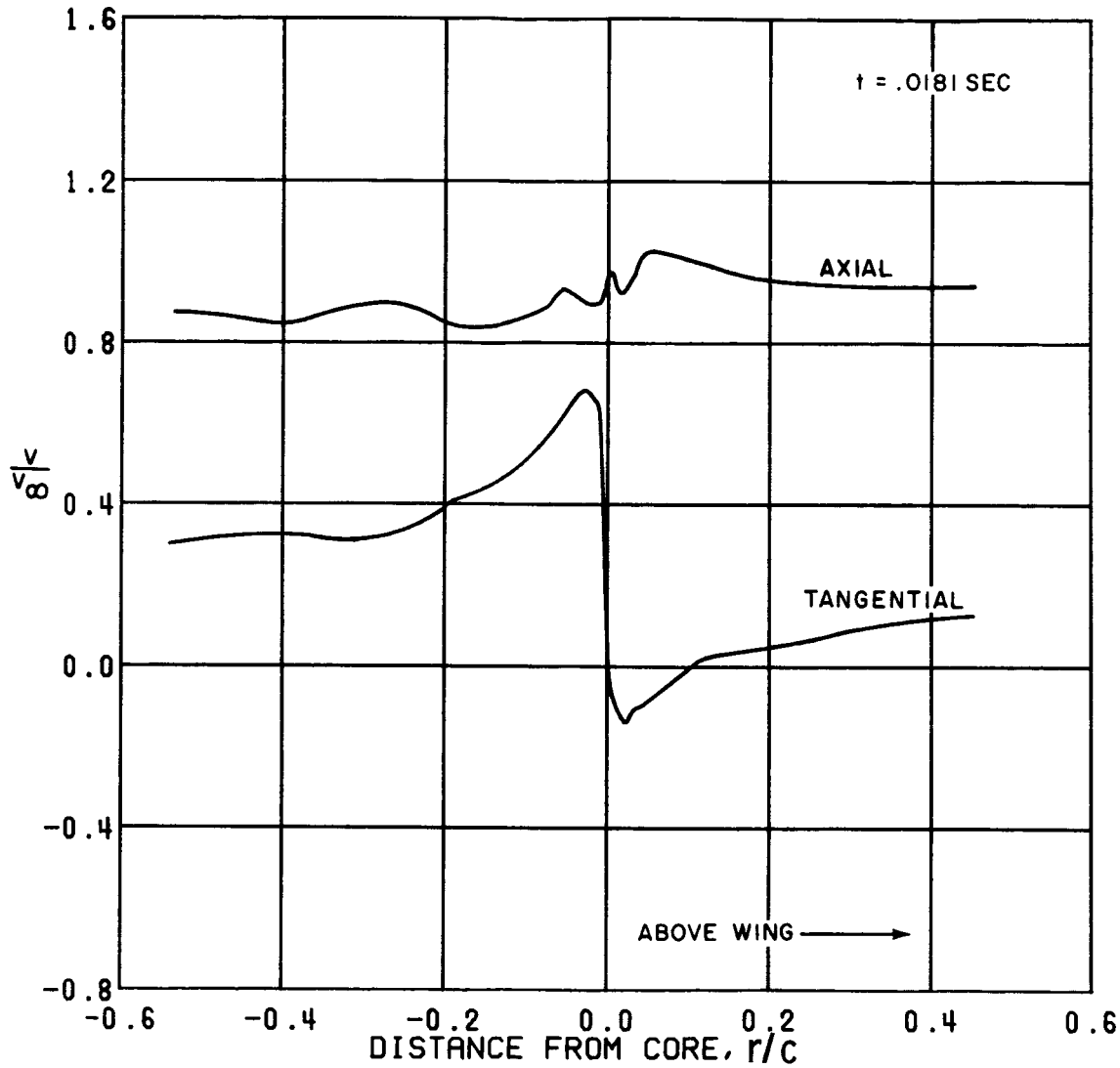

FIGURE 42. LARGE RECT. TIP, VORTEX VELOCITY DISTRIBUTIONS

6.0 CHORD LENGTHS FROM TRAILING EDGE
TRAVERSE NORMAL TO SPAN
MACH 0.60 9.0 DEG PITCH
REYNOLDS NUMBER = 6 900 000.
FREE STREAM VELOCITY = 210. M/SEC = 688. FT/SEC

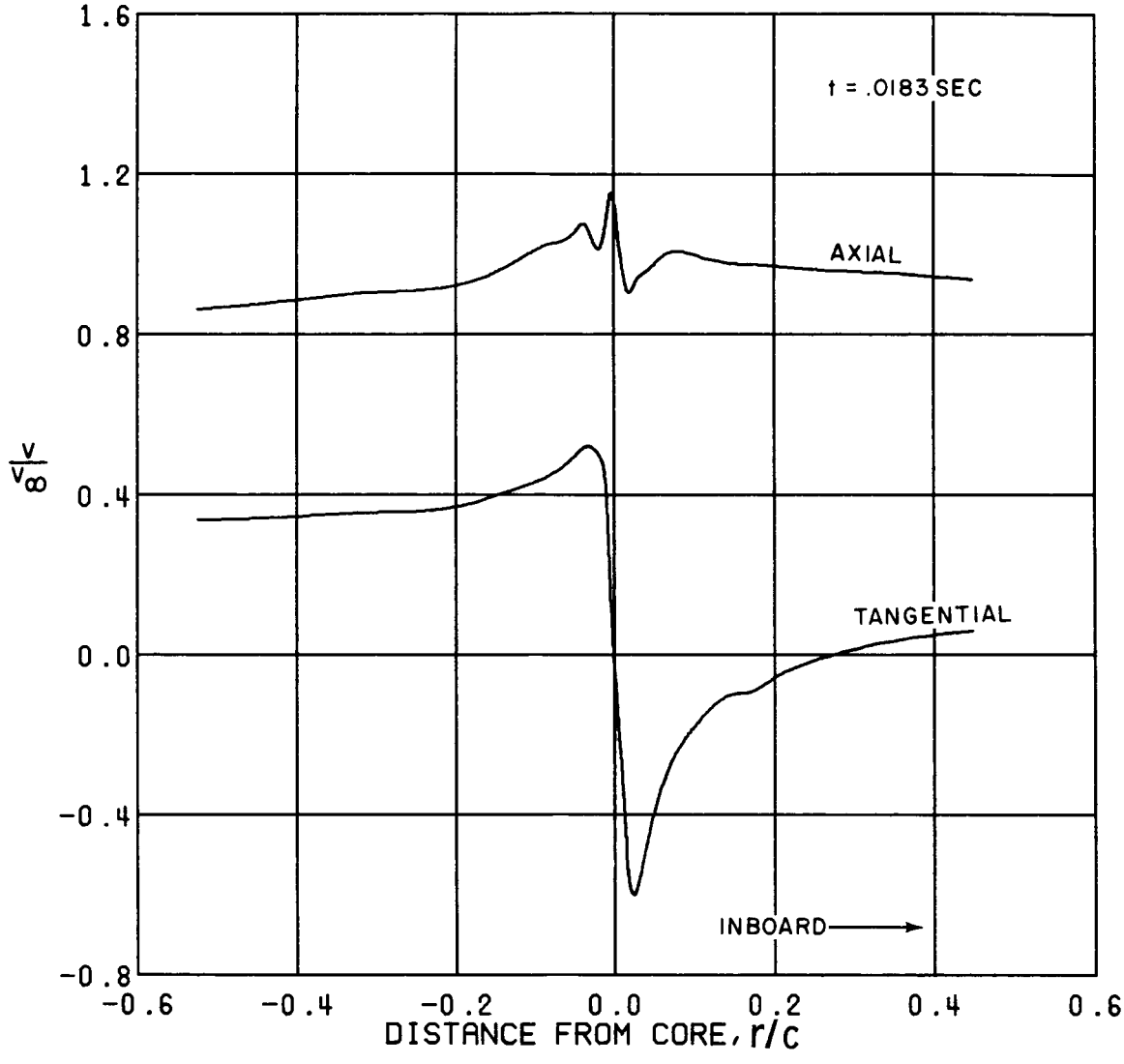

FIGURE 43. LARGE RECT. TIP, VORTEX VELOCITY DISTRIBUTIONS

5.0 CHORD LENGTHS FROM TRAILING EDGE
TRAVERSE PARALLEL TO SPAN
MACH 0.60 9.0 DEG PITCH
REYNOLDS NUMBER = 6 700 000.
FREE STREAM VELOCITY = 208. M/SEC = 682. FT/SEC

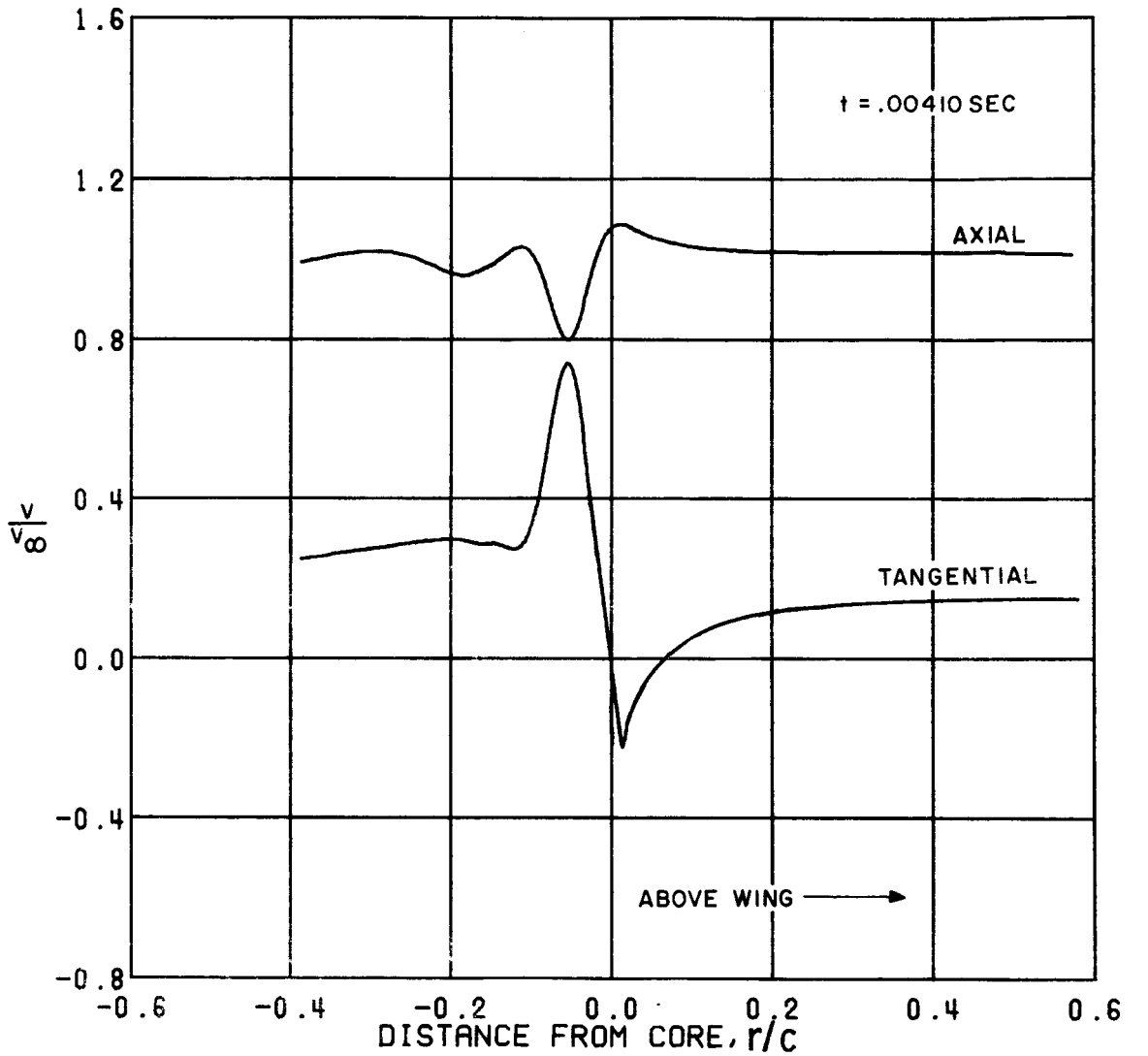

FIGURE 44. SMALL RECT. TIP, VORTEX VELOCITY DISTRIBUTIONS

2.0 CHORD LENGTHS FROM TRAILING EDGE
TRAVERSE NORMAL TO SPAN
MACH 0.20 6.0 DEG PITCH
REYNOLDS NUMBER = 460 000.
FREE STREAM VELOCITY = 72. M/SEC = 237. FT/SEC

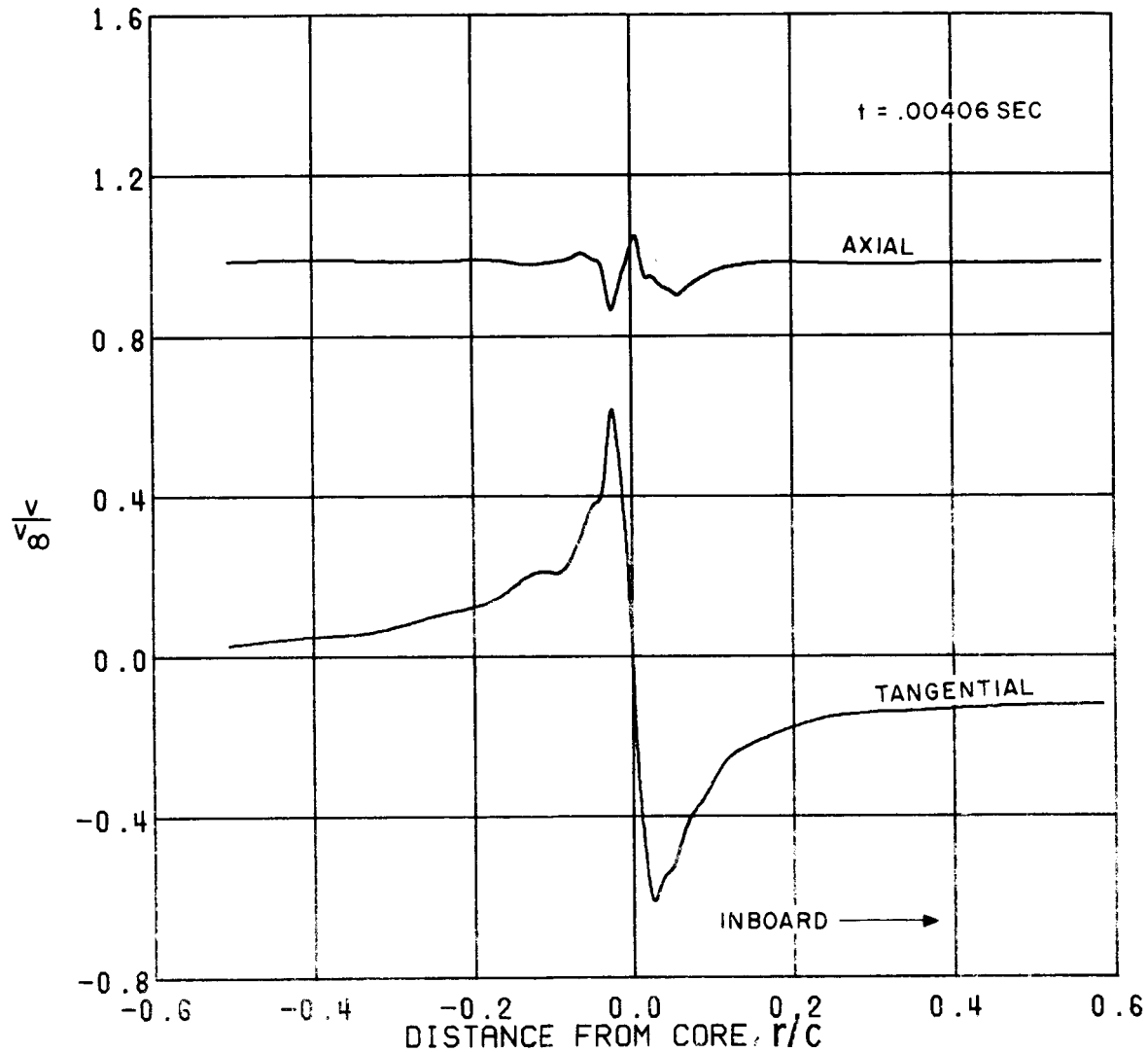

FIGURE 45. SMALL RECT. TIP, VORTEX VELOCITY DISTRIBUTIONS

2.0 CHORD LENGTHS FROM TRAILING EDGE
TRAVERSE PARALLEL TO SPAN
MACH 0.20 8.0 DEG PITCH
REYNOLDS NUMBER = 460 000.
FREE STREAM VELOCITY = 73. M/SEC = 240. FT/SEC

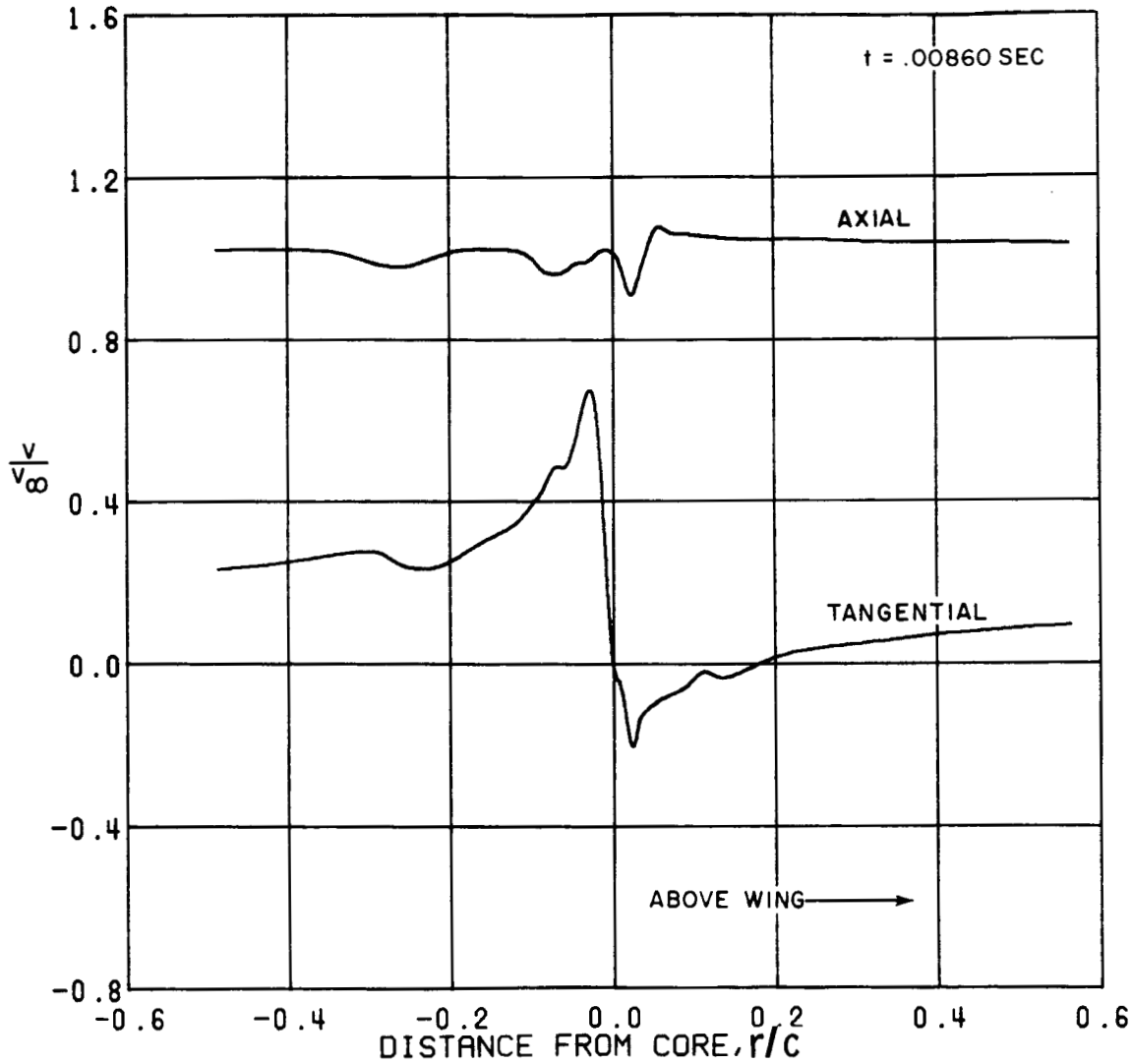

FIGURE 46. SMALL RECT. TIP, VORTEX VELOCITY DISTRIBUTIONS

5.0 CHORD LENGTHS FROM TRAILING EDGE
TRAVERSE NORMAL TO SPAN
MACH 0.20 6.0 DEG PITCH
REYNOLDS NUMBER = 440 000.
FREE STREAM VELOCITY = 72. M/SEC = 237. FT/SEC

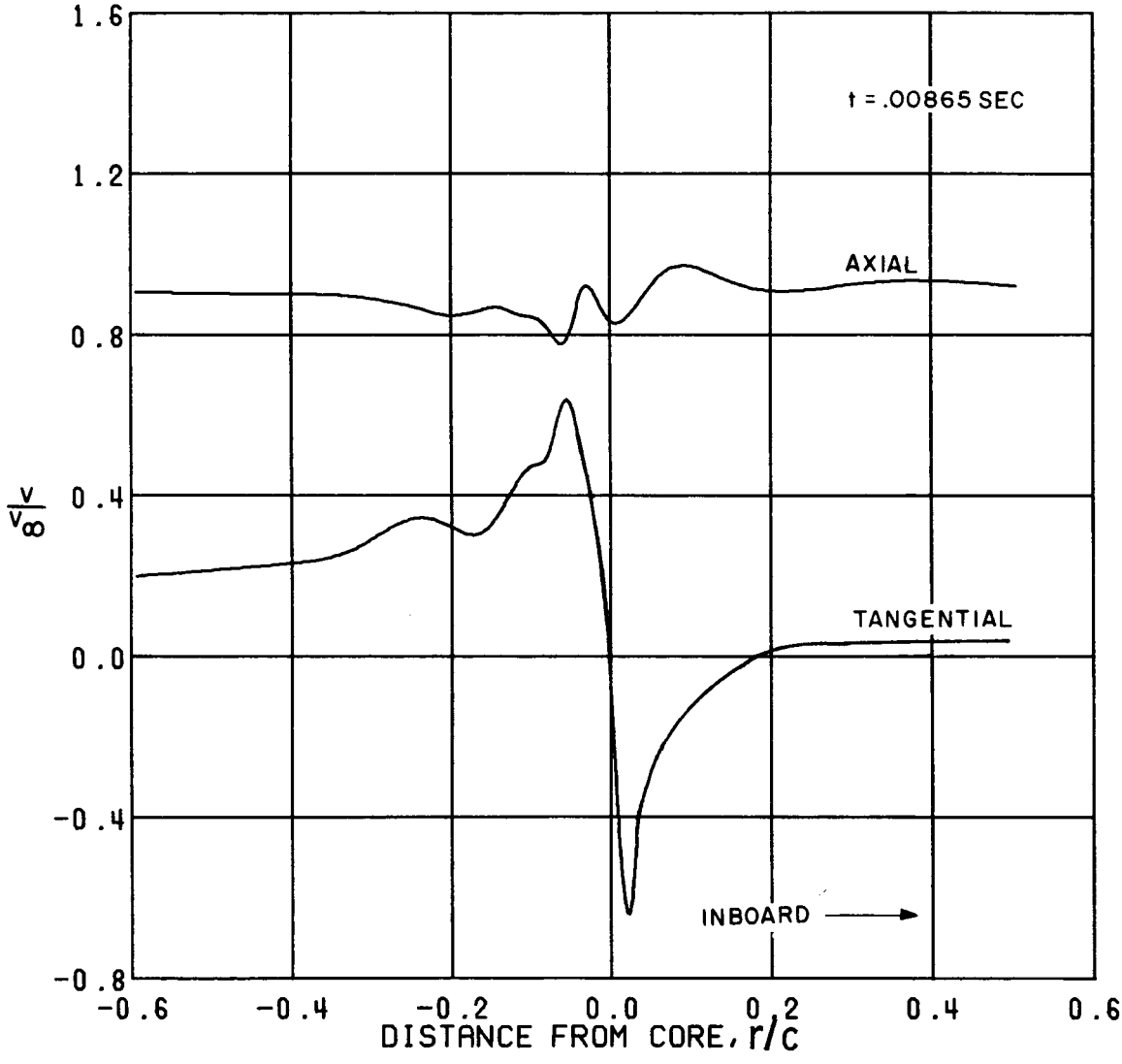

FIGURE 47. SMALL RECT. TIP, VORTEX VELOCITY DISTRIBUTIONS

6.0 CHORD LENGTHS FROM TRAILING EDGE
TRAVERSE PARALLEL TO SPAN
MACH 0.20 6.0 DEG PITCH
REYNOLDS NUMBER = 450 000.
FREE STREAM VELOCITY = 72. M/SEC = 236. FT/SEC

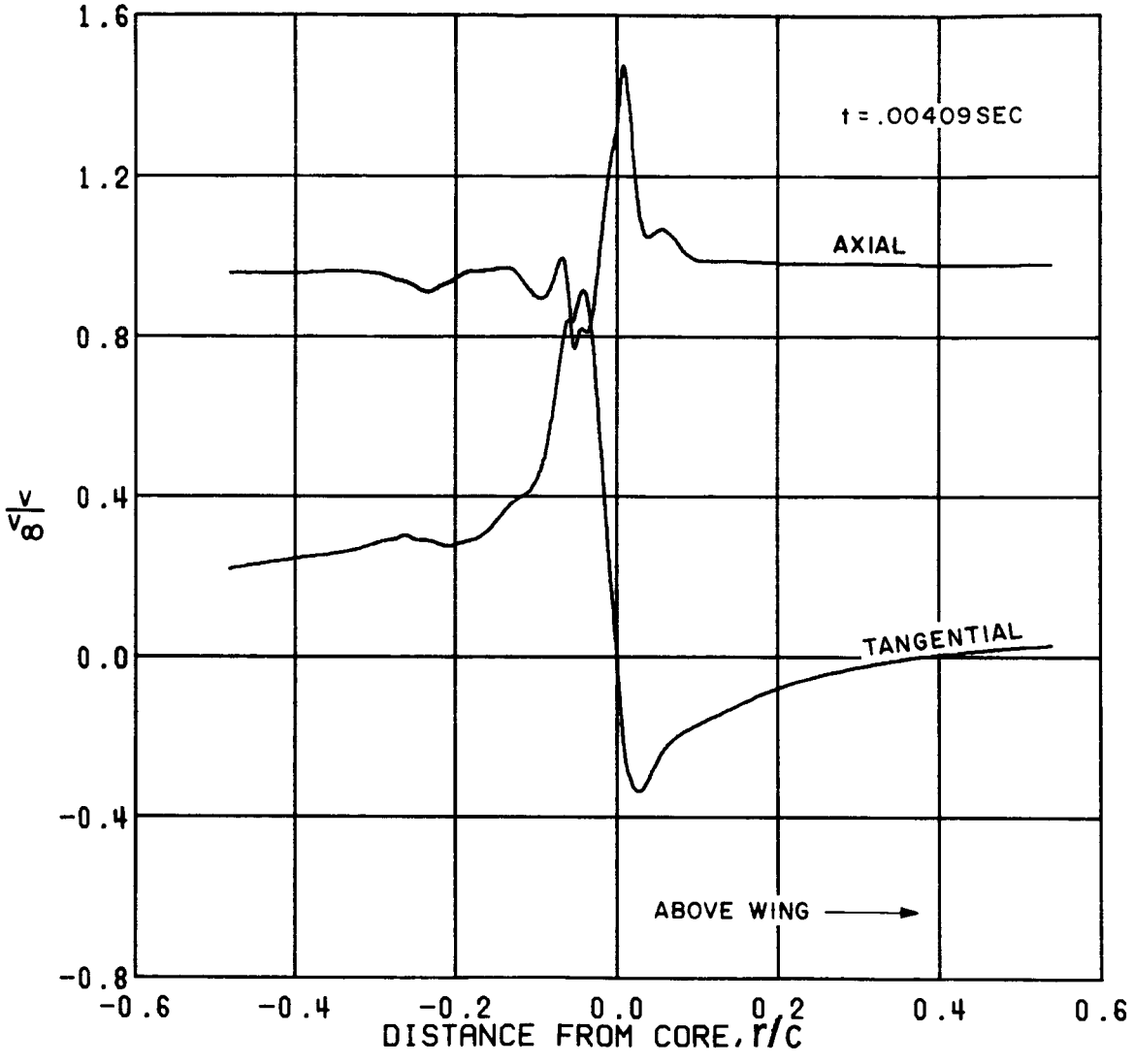

FIGURE 48. SMALL RECT. TIP, VORTEX VELOCITY DISTRIBUTIONS

2.0 CHORD LENGTHS FROM TRAILING EDGE
TRAVERSE NORMAL TO SPAN
MACH 0.20 8.0 DEG PITCH
REYNOLDS NUMBER = 460 000.
FREE STREAM VELOCITY = 73. M/SEC = 238. FT/SEC

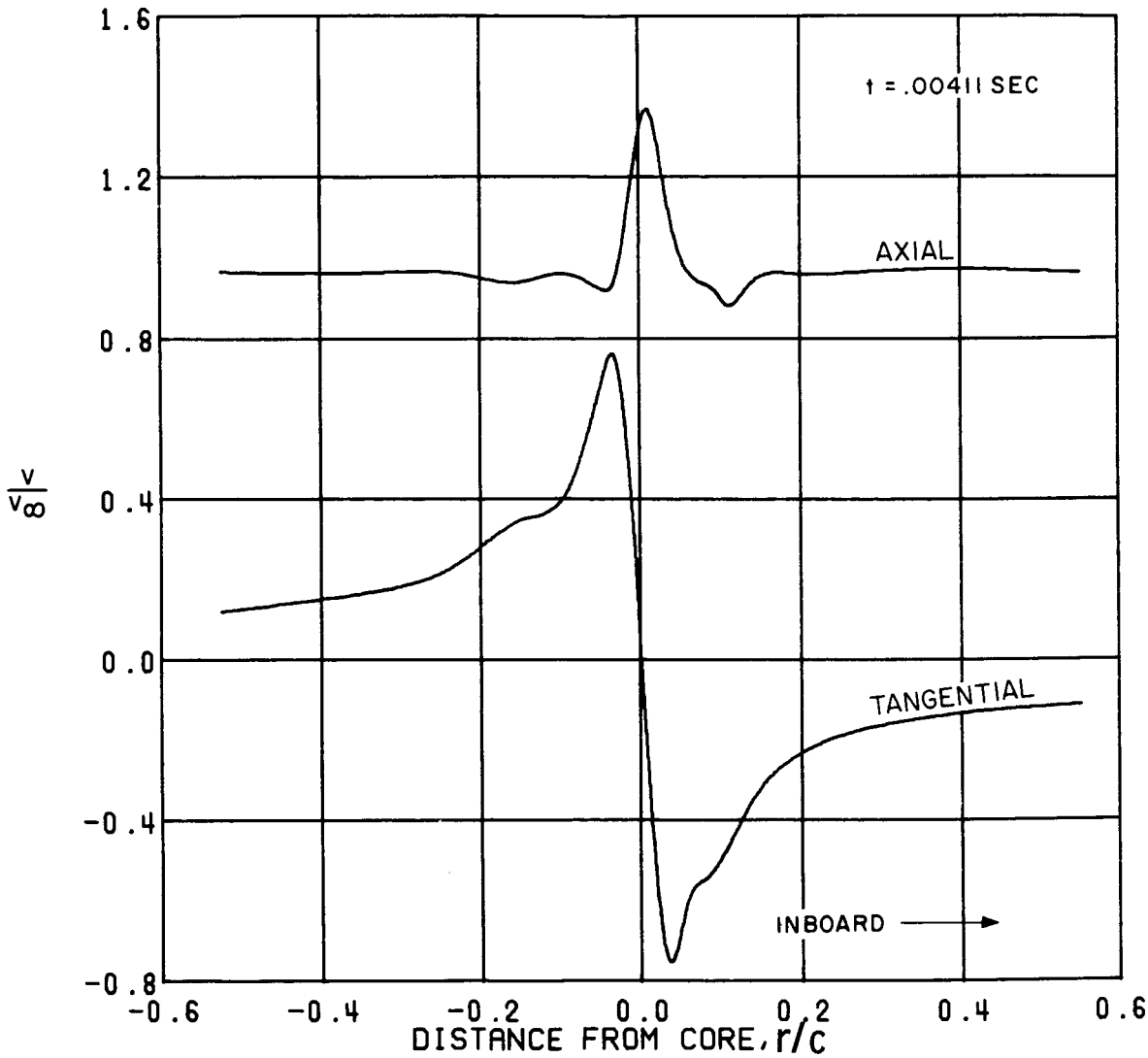

FIGURE 49. SMALL RECT. TIP, VORTEX VELOCITY DISTRIBUTIONS

2.0 CHORD LENGTHS FROM TRAILING EDGE
TRAVERSE PARALLEL TO SPAN
MACH 0.20 9.0 DEG PITCH
REYNOLDS NUMBER = 460 000.
FREE STREAM VELOCITY = 72. M/SEC = 237. FT/SEC

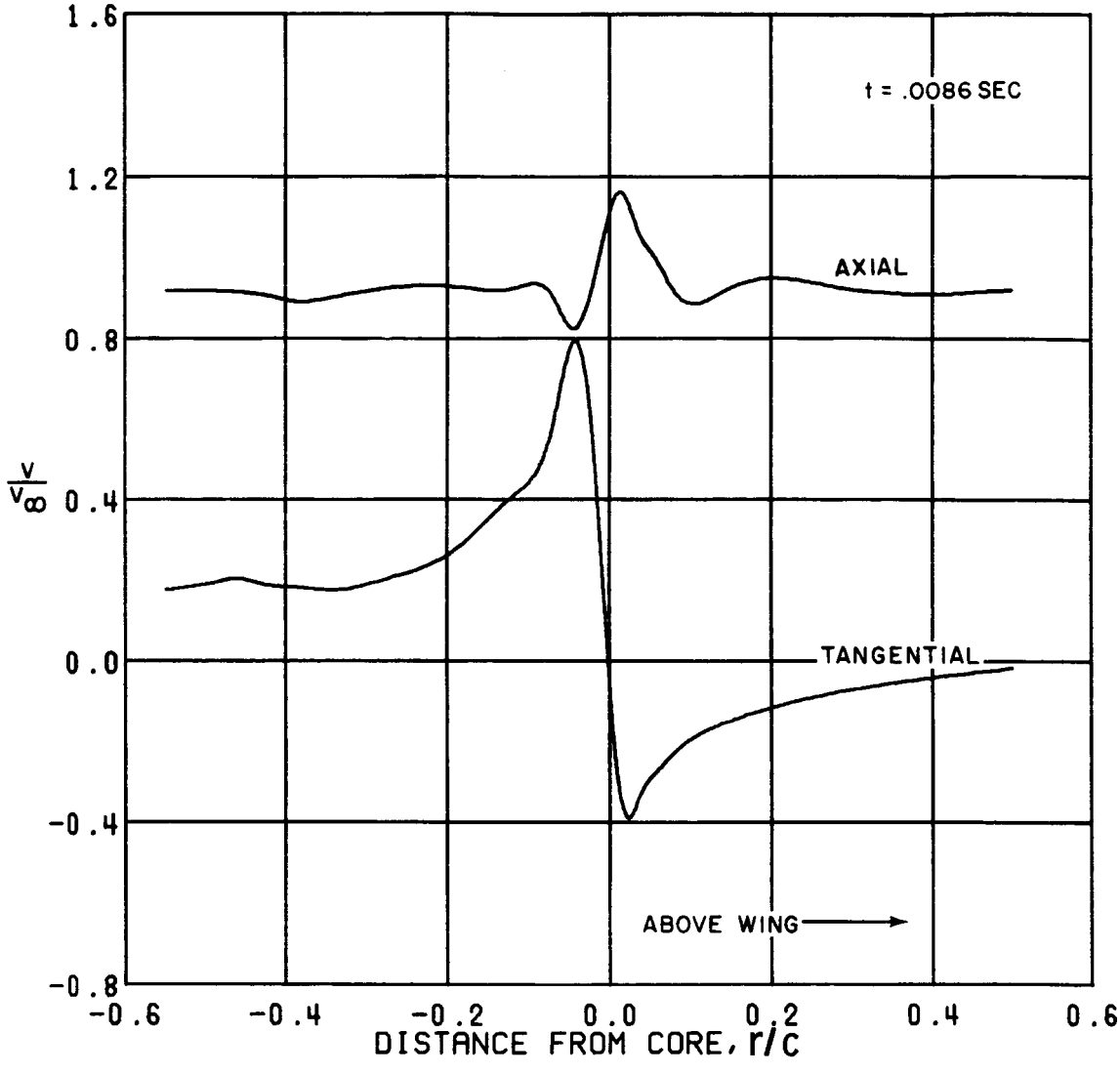

FIGURE 50. SMALL RECT. TIP, VORTEX VELOCITY DISTRIBUTIONS

5.0 CHORD LENGTHS FROM TRAILING EDGE
TRAVERSE NORMAL TO SPAN
MACH 0.20 8.0 DEG PITCH
REYNOLDS NUMBER = 450 000.
FREE STREAM VELOCITY = 72. M/SEC = 236. FT/SEC

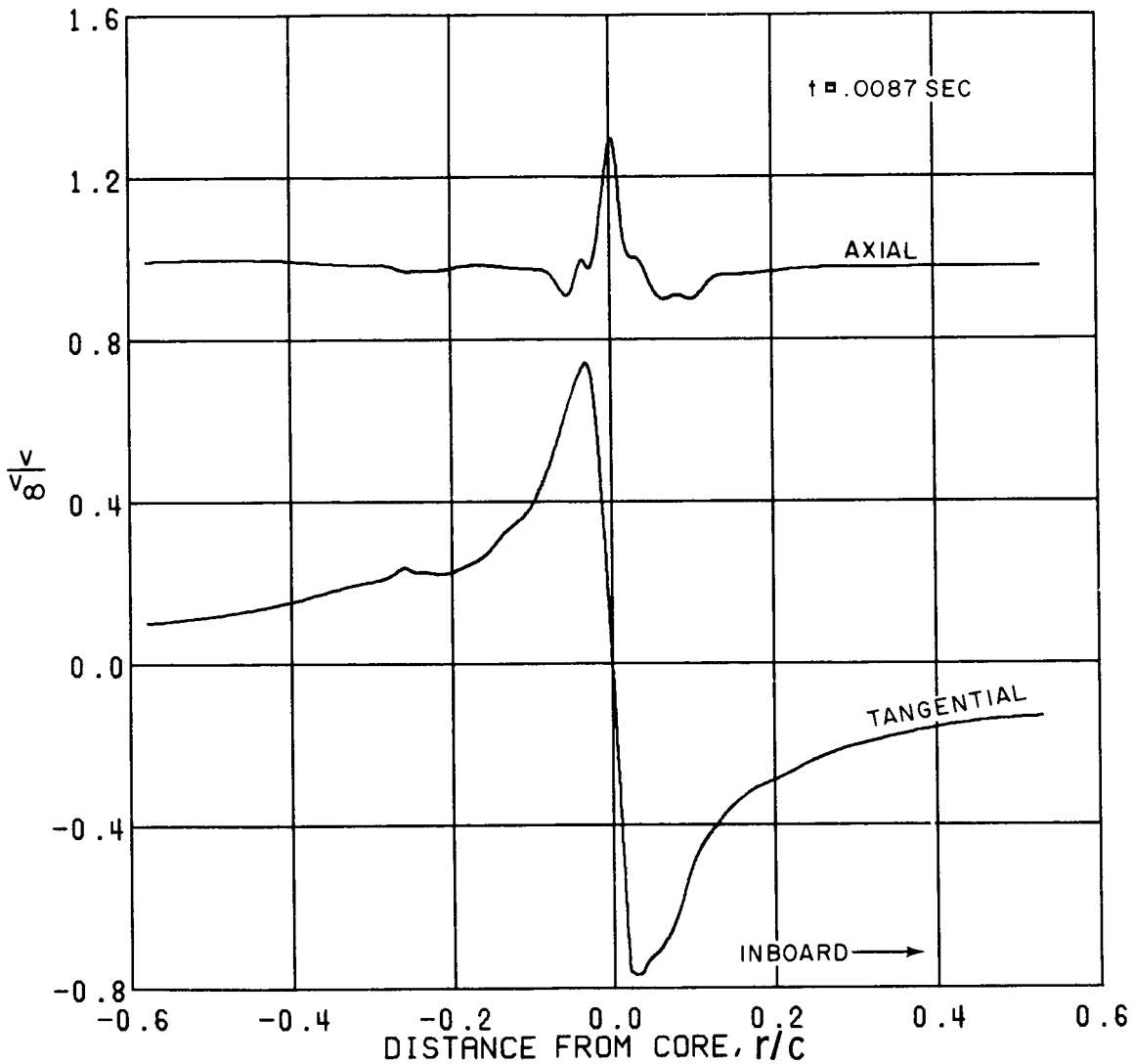

FIGURE 51. SMALL RECT. TIP, VORTEX VELOCITY DISTRIBUTIONS

5.0 CHORD LENGTHS FROM TRAILING EDGE
TRAVERSE PARALLEL TO SPAN
MACH 0.20 9.0 DEG PITCH
REYNOLDS NUMBER = 450 000.
FREE STREAM VELOCITY = 71. M/SEC = 234. FT/SEC

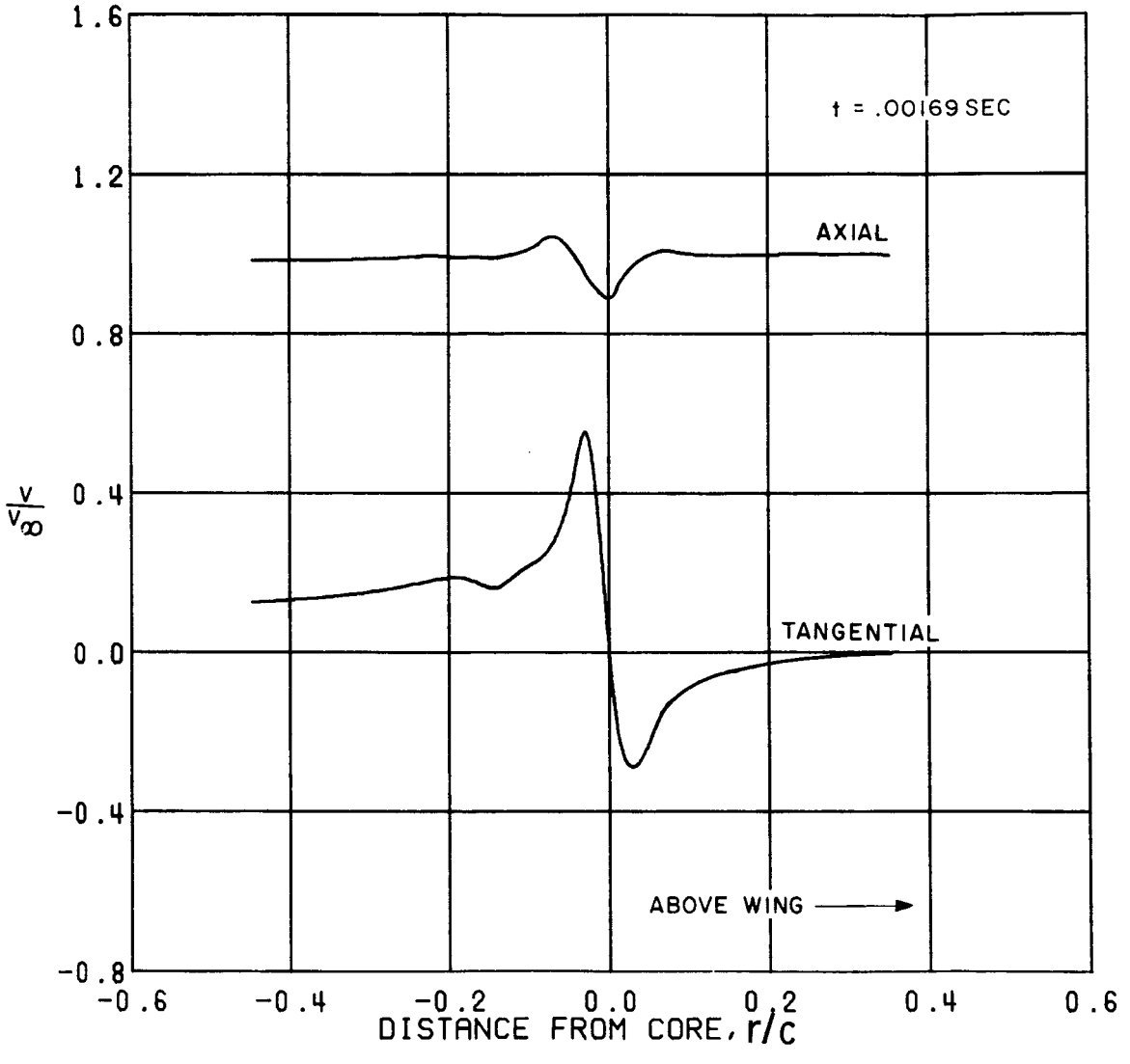

FIGURE 52. SMALL RECT. TIP, VORTEX VELOCITY DISTRIBUTIONS

2.0 CHORD LENGTHS FROM TRAILING EDGE
TRAVERSE NORMAL TO SPAN
MACH 0.50 8.0 DEG PITCH
REYNOLDS NUMBER = 1 000 000.
FREE STREAM VELOCITY = 175. M/SEC = 574. FT/SEC

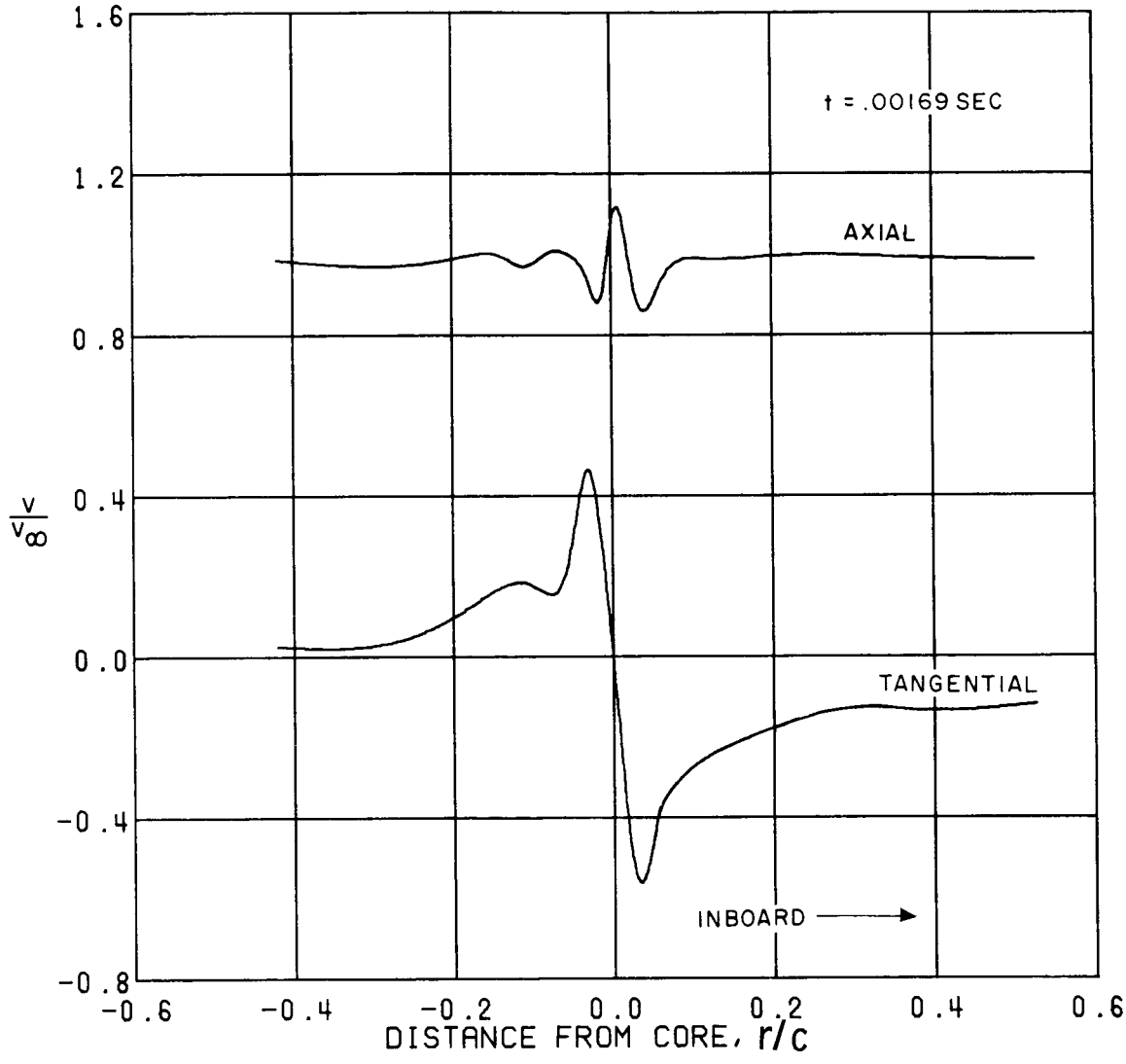

FIGURE 53. SMALL RECT. TIP, VORTEX VELOCITY DISTRIBUTIONS

2.0 CHORD LENGTHS FROM TRAILING EDGE
TRAVERSE PARALLEL TO SPAN
MACH 0.50 6.0 DEG PITCH
REYNOLDS NUMBER = 990 000.
FREE STREAM VELOCITY = 175. M/SEC = 574. FT/SEC

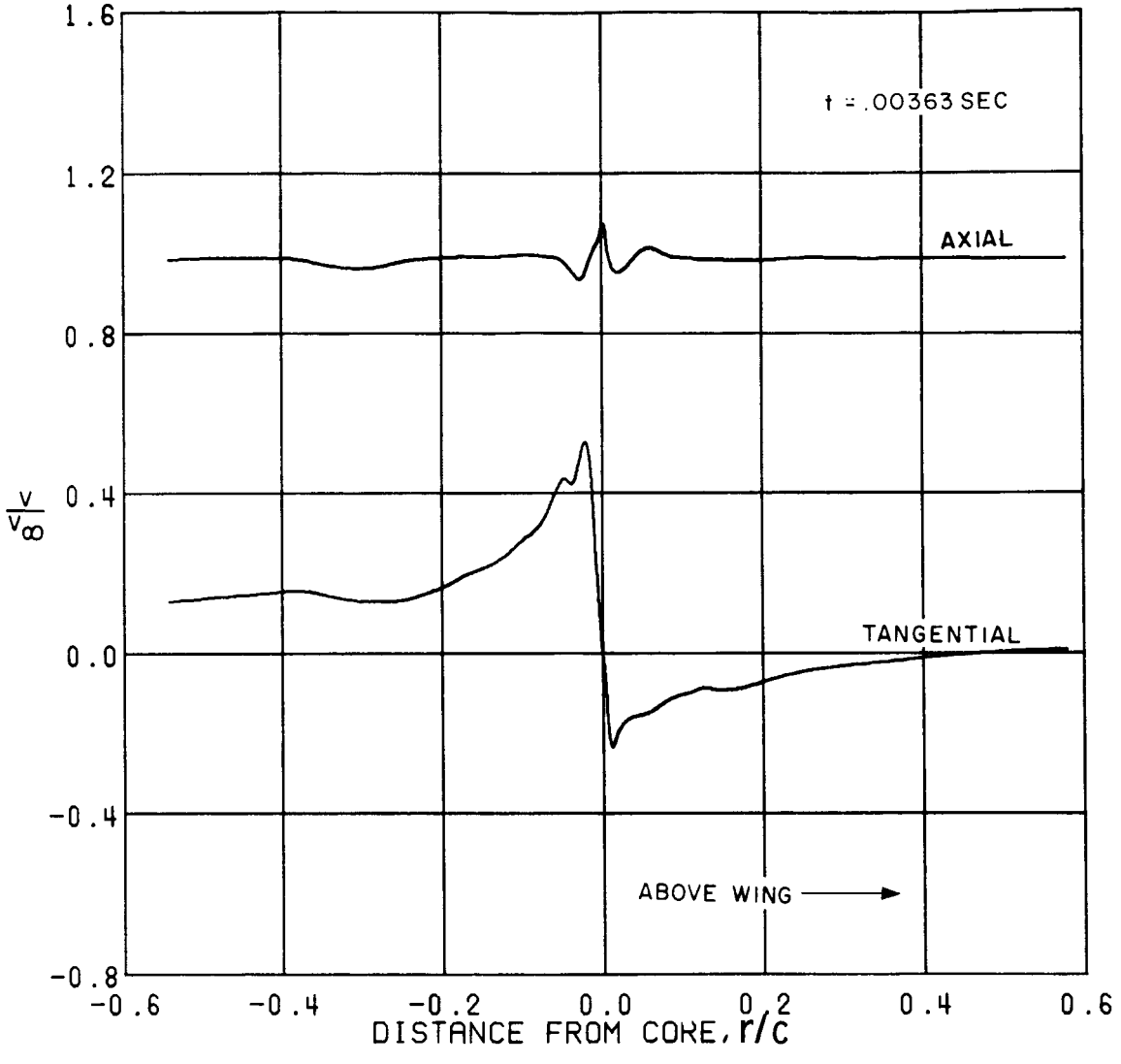

FIGURE 54 . SMALL RECT. TIP, VORTEX VELOCITY DISTRIBUTIONS

5.0 CHORD LENGTHS FROM TRAILING EDGE
TRAVERSE NORMAL TO SPAN
MACH 0.50 6.0 DEG PITCH
REYNOLDS NUMBER = 960 000.
FREE STREAM VELOCITY = 171. M/SEC = 561. FT/SEC

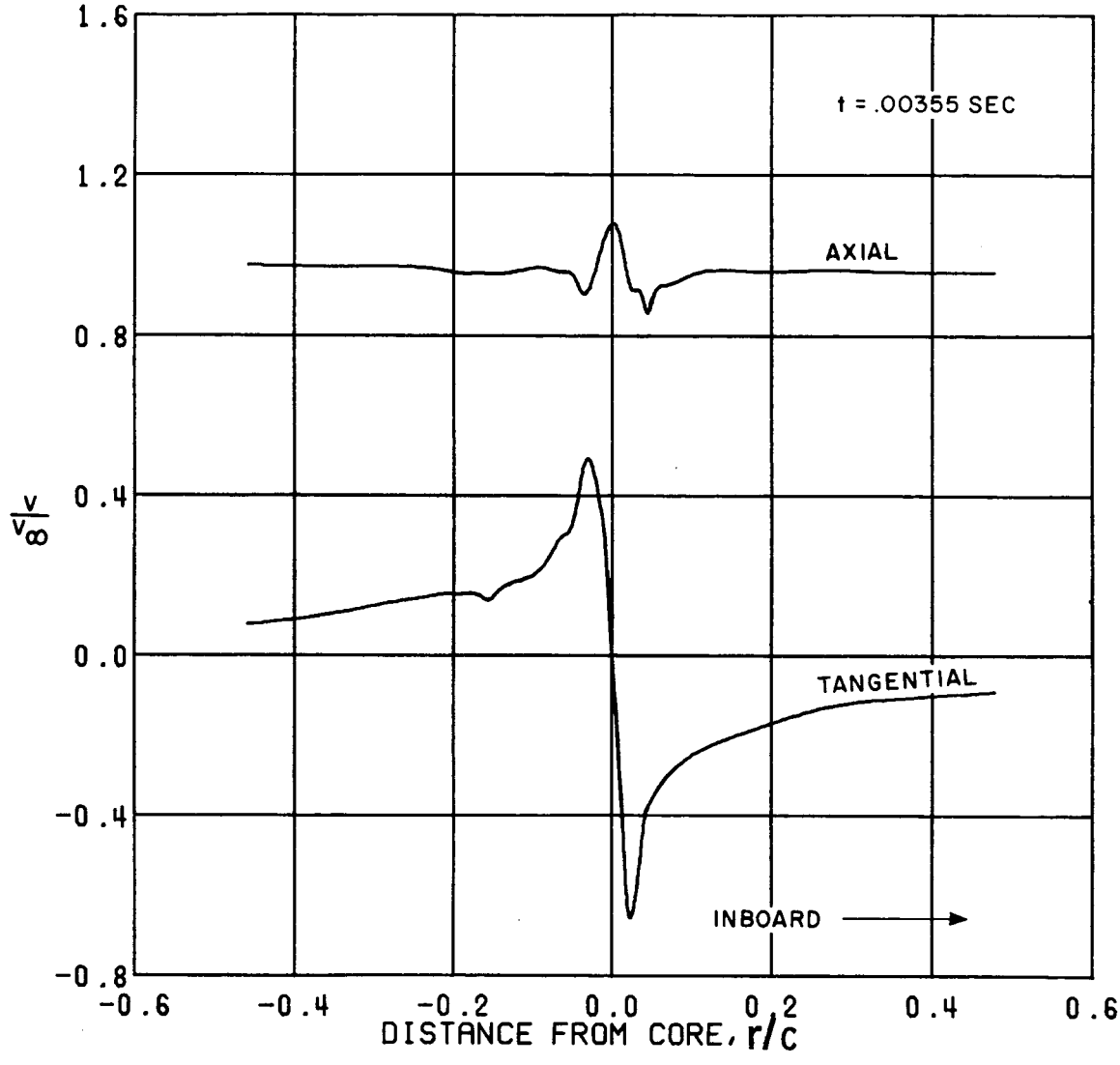

FIGURE 55. SMALL RECT. TIP, VORTEX VELOCITY DISTRIBUTIONS

5.0 CHORD LENGTHS FROM TRAILING EDGE
TRAVERSE PARALLEL TO SPAN
MACH 0.50 6.0 DEG PITCH
REYNOLDS NUMBER = 900 000.
FREE STREAM VELOCITY = 175. M/SEC = 575. FT/SEC

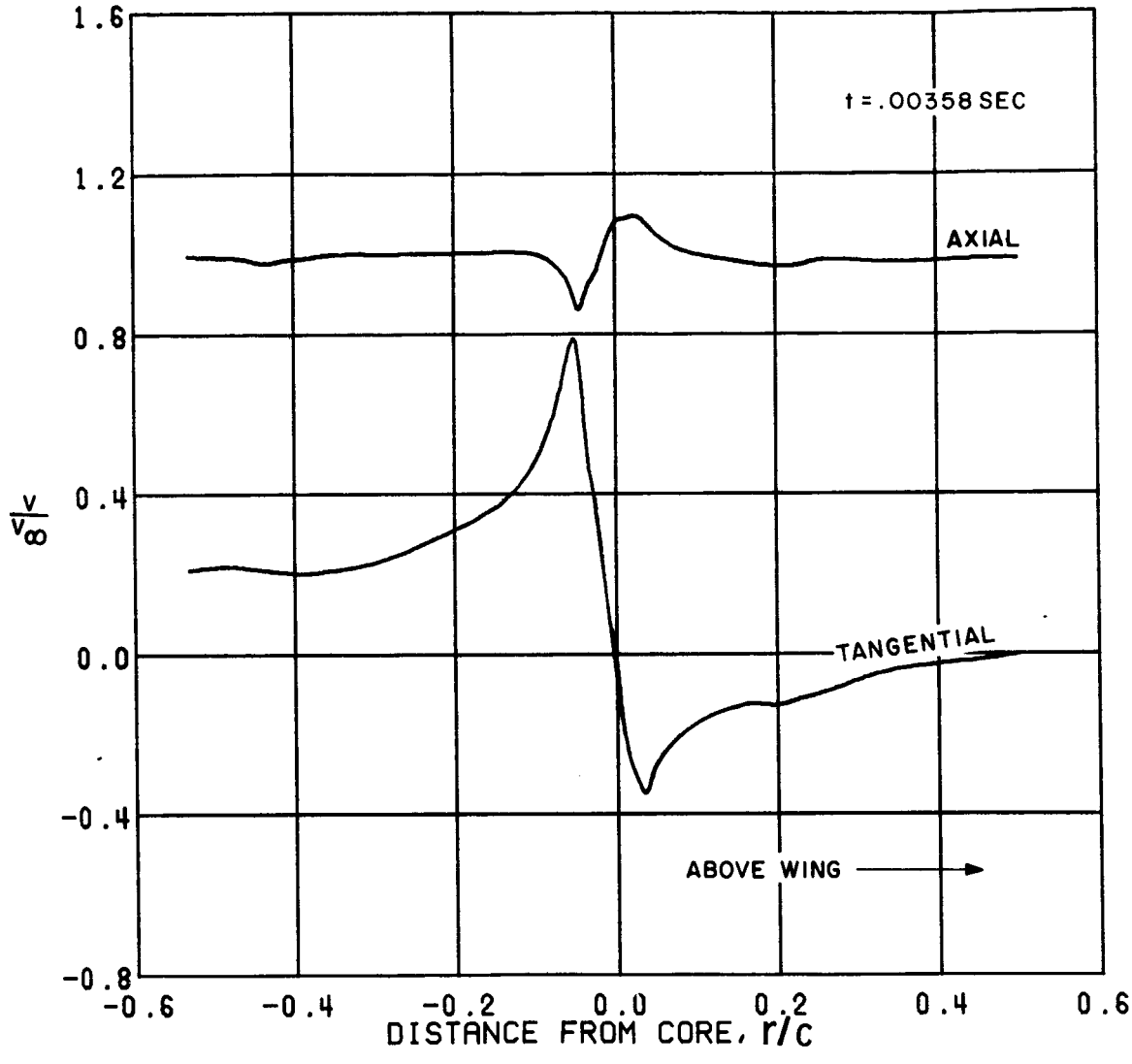

FIGURE 56. SMALL RECT. TIP, VORTEX VELOCITY DISTRIBUTIONS

5.0 CHORD LENGTHS FROM TRAILING EDGE
TRAVERSE NORMAL TO SPAN
MACH 0.50 9.0 DEG PITCH
REYNOLDS NUMBER = 930 000.
FREE STREAM VELOCITY = 174. M/SEC = 569. FT/SEC

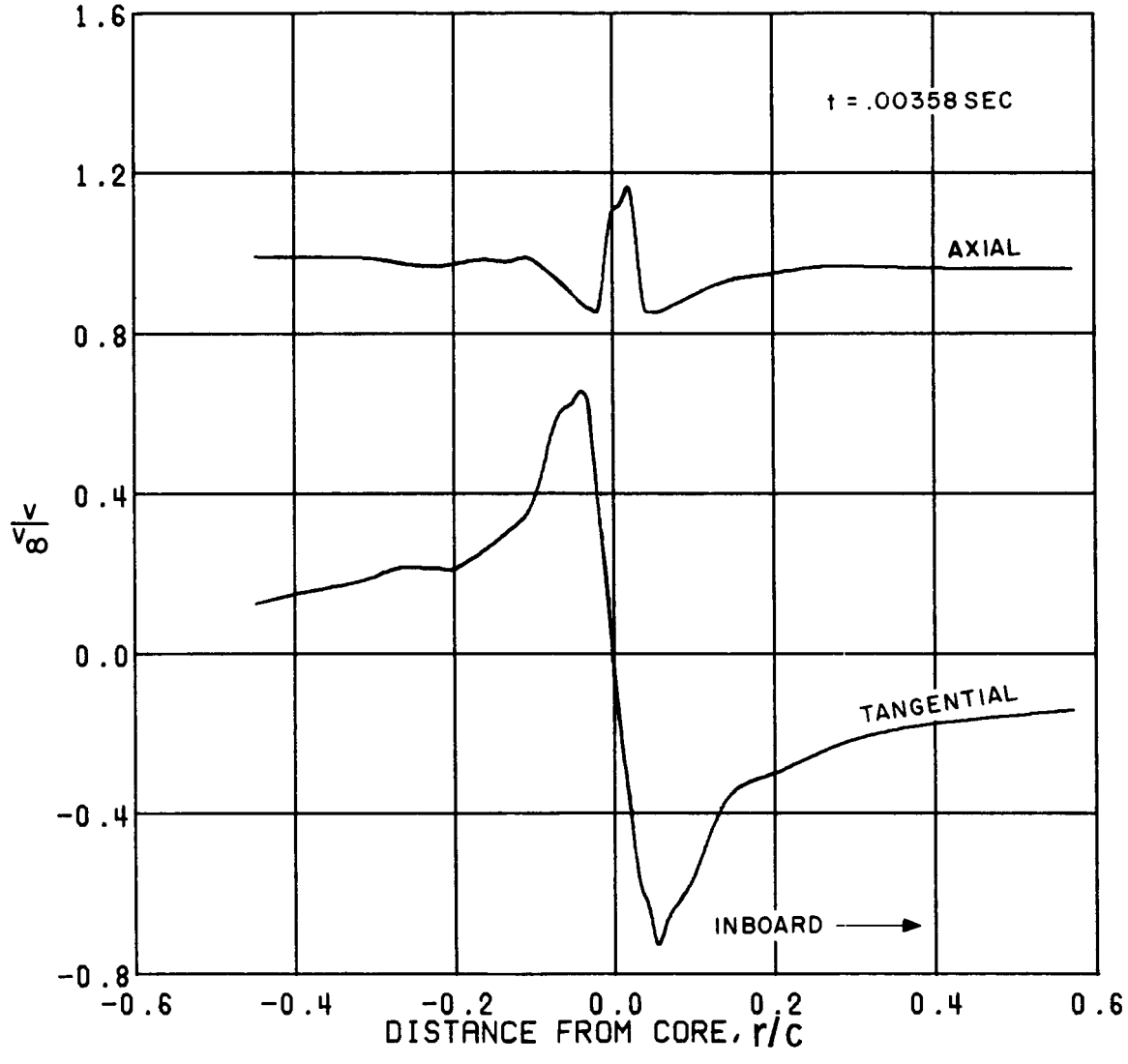

FIGURE 57. SMALL RECT. TIP, VORTEX VELOCITY DISTRIBUTIONS

5.0 CHORD LENGTHS FROM TRAILING EDGE
TRAVERSE PARALLEL TO SPAN
MACH 0.50 9.0 DEG PITCH
REYNOLDS NUMBER = 990 000.
FREE STREAM VELOCITY = 174. M/SEC = 569. FT/SEC

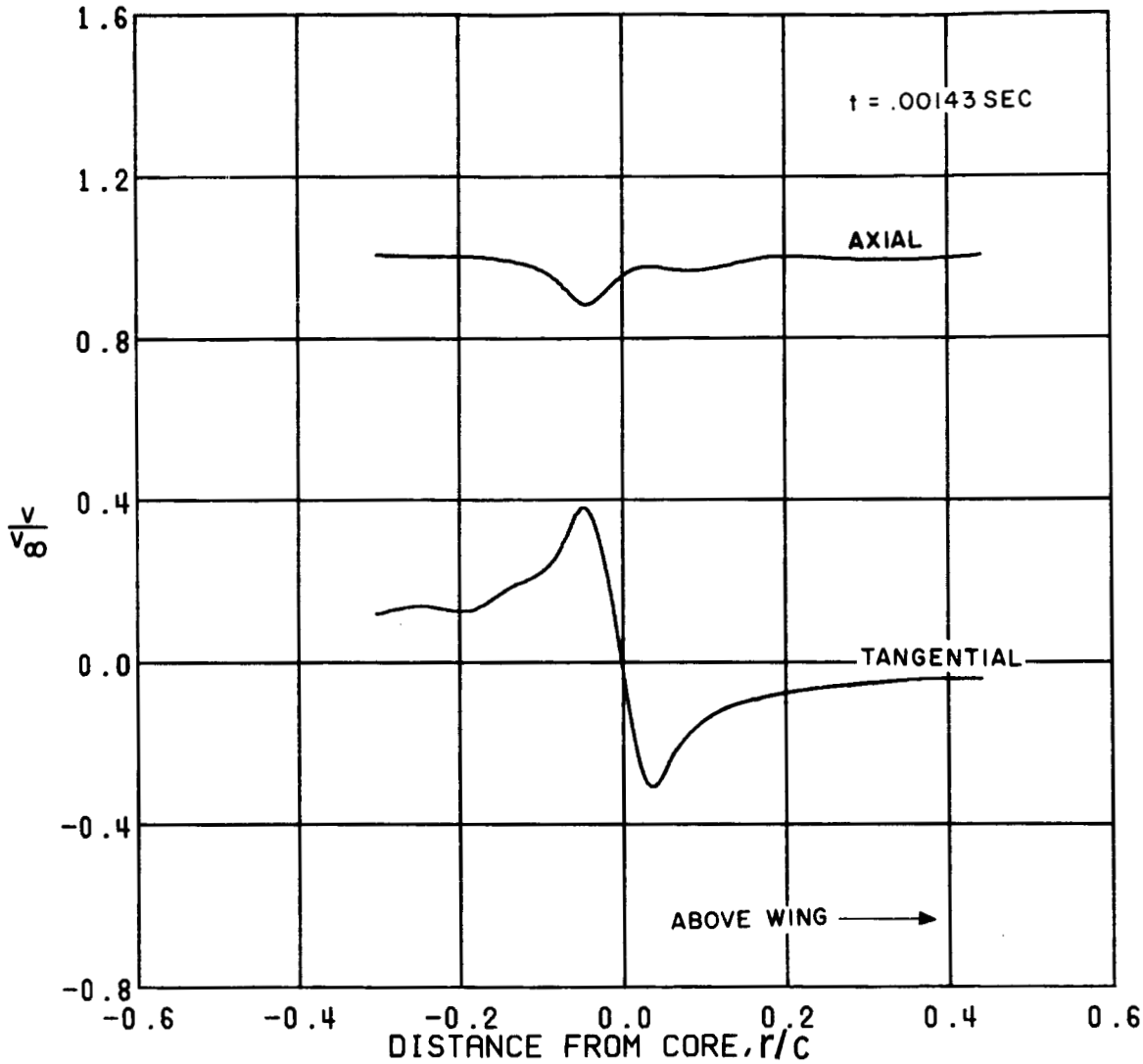

FIGURE 58. SMALL RECT. TIP, VORTEX VELOCITY DISTRIBUTIONS

2.0 CHORD LENGTHS FROM TRAILING EDGE
TRAVERSE NORMAL TO SPAN
MACH 0.60 8.0 DEG PITCH
REYNOLDS NUMBER = 1 100 000.
FREE STREAM VELOCITY = 207. M/SEC = 680. FT/SEC

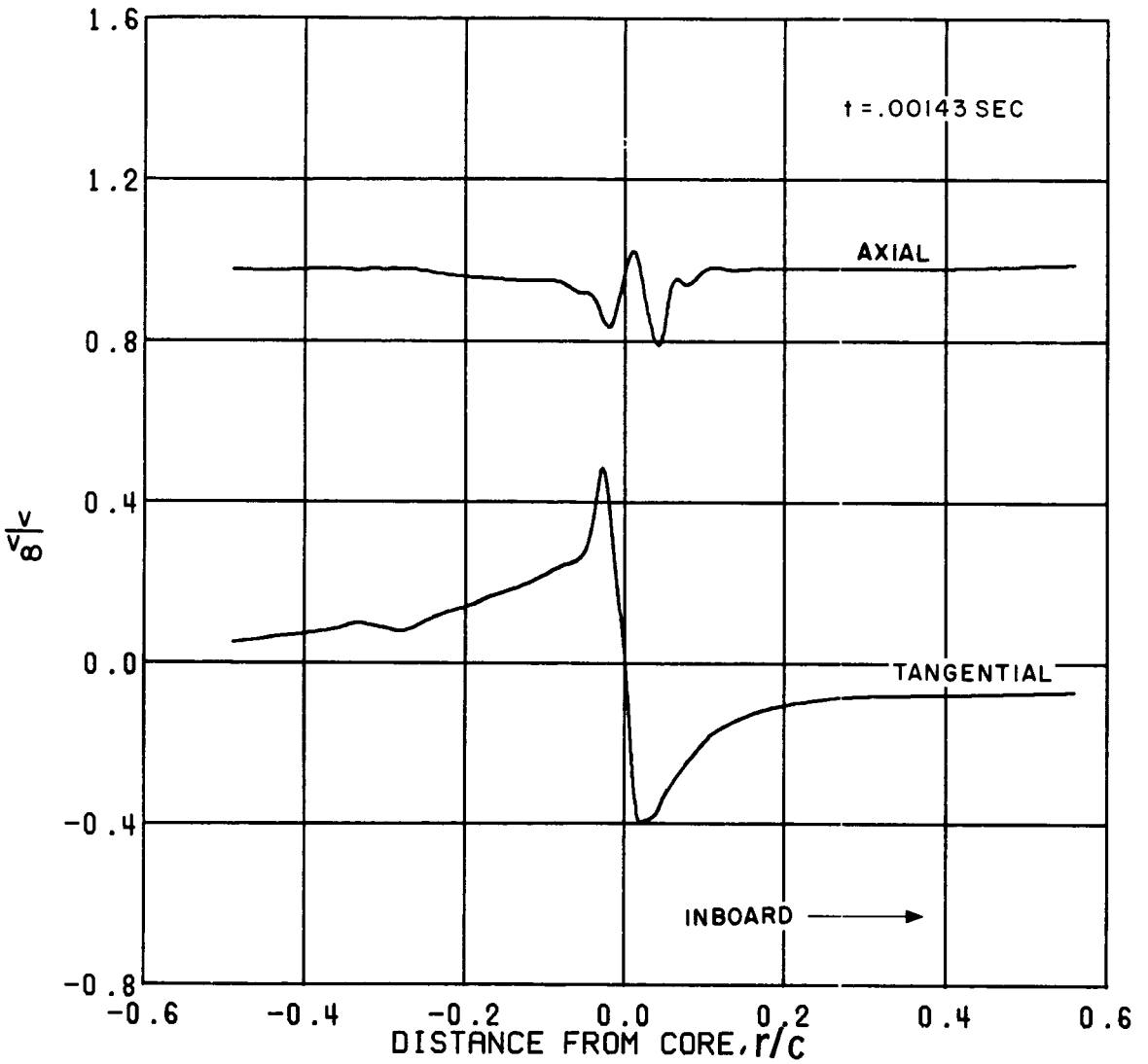

FIGURE 59. SMALL RECT. TIP, VORTEX VELOCITY DISTRIBUTIONS

2.0 CHORD LENGTHS FROM TRAILING EDGE
TRAVERSE PARALLEL TO SPAN
MACH 0.60 6.0 DEG PITCH
REYNOLDS NUMBER = 1 100 000.
FREE STREAM VELOCITY = 207. M/SEC = 680. FT/SEC

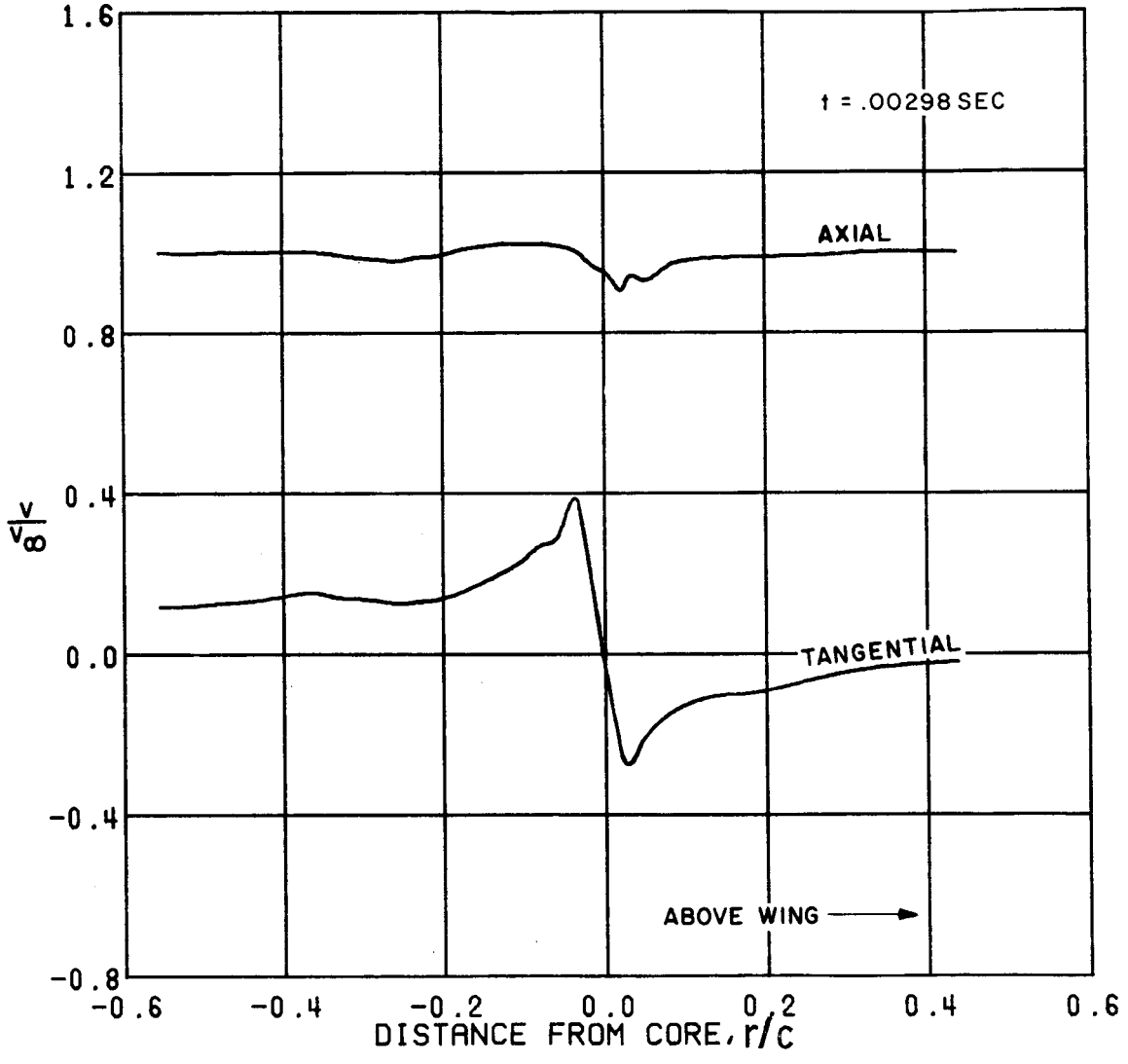

FIGURE 60. SMALL RECT. TIP, VORTEX VELOCITY DISTRIBUTIONS

5.0 CHORD LENGTHS FROM TRAILING EDGE
TRAVERSE NORMAL TO SPAN
MACH 0.60 6.0 DEG PITCH
REYNOLDS NUMBER = 1 100 000.
FREE STREAM VELOCITY = 209. M/SEC = 683. FT/SEC

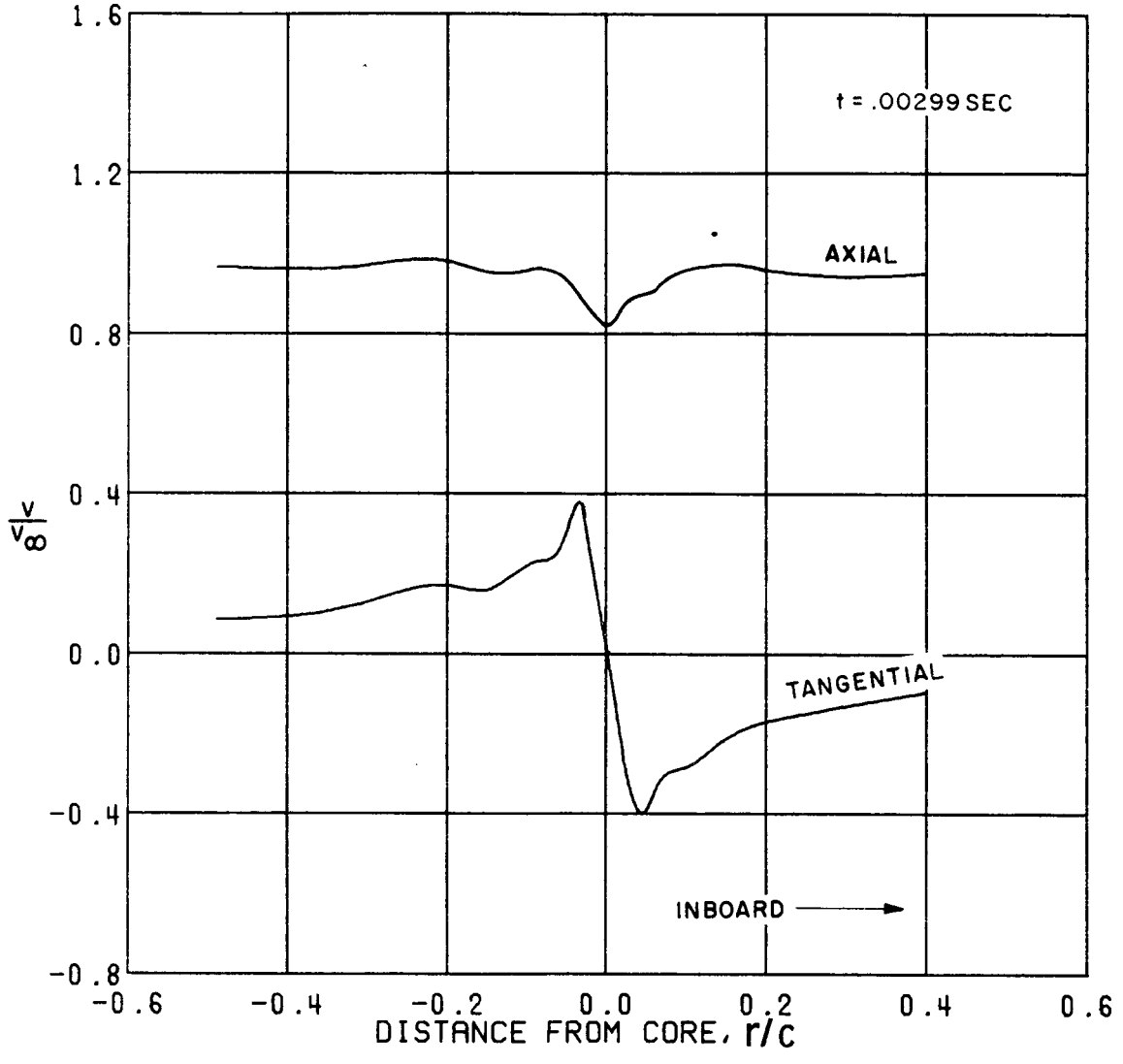

FIGURE 61. SMALL RECT. TIP, VORTEX VELOCITY DISTRIBUTIONS

5.0 CHORD LENGTHS FROM TRAILING EDGE
TRAVERSE PARALLEL TO SPAN
MACH 0.60 6.0 DEG PITCH
REYNOLDS NUMBER = 1 100 000.
FREE STREAM VELOCITY = 207. M/SEC = 681. FT/SEC

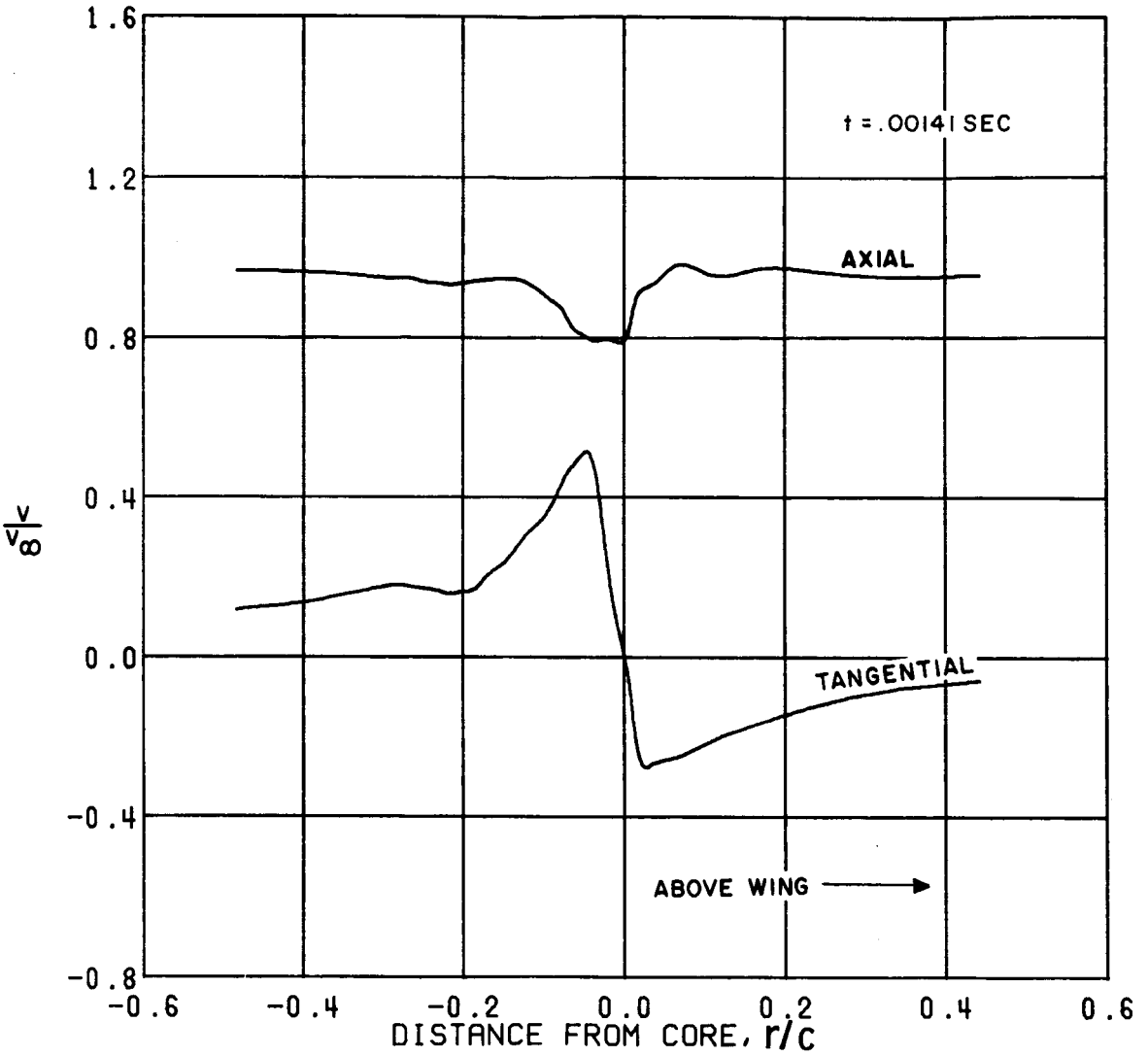

FIGURE 62. SMALL RECT. TIP, VORTEX VELOCITY DISTRIBUTIONS

2.0 CHORD LENGTHS FROM TRAILING EDGE
TRAVERSE NORMAL TO SPAN
MACH 0.60 9.0 DEG PITCH
REYNOLDS NUMBER = 1 100 000.
FREE STREAM VELOCITY = 203. M/SEC = 666. FT/SEC

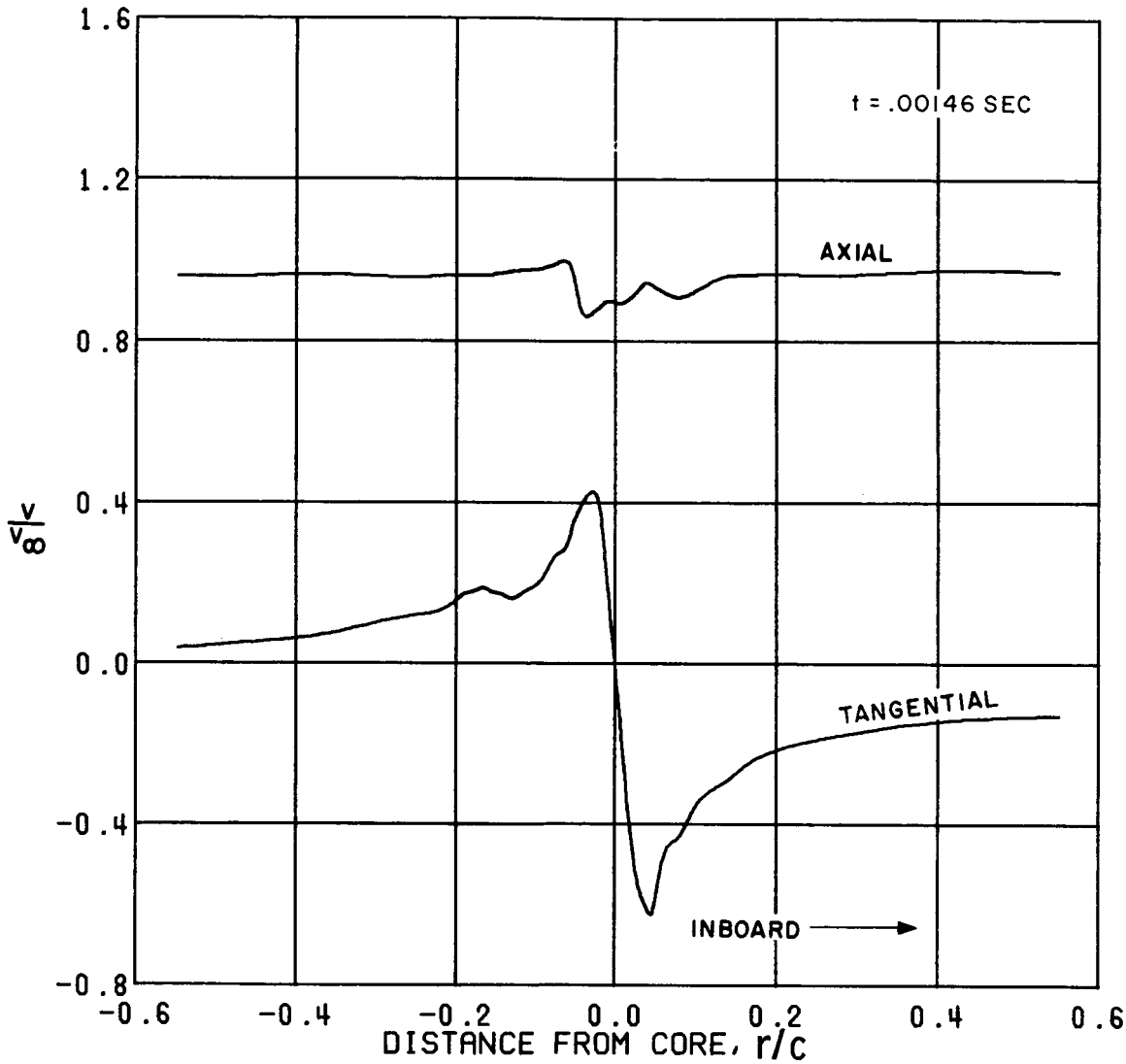

FIGURE 63. SMALL RECT. TIP, VORTEX VELOCITY DISTRIBUTIONS

2.0 CHORD LENGTHS FROM TRAILING EDGE
TRAVERSE PARALLEL TO SPAN
MACH 0.60 9.0 DEG PITCH
REYNOLDS NUMBER = 1 100 000.
FREE STREAM VELOCITY = 204. M/SEC = 669. FT/SEC

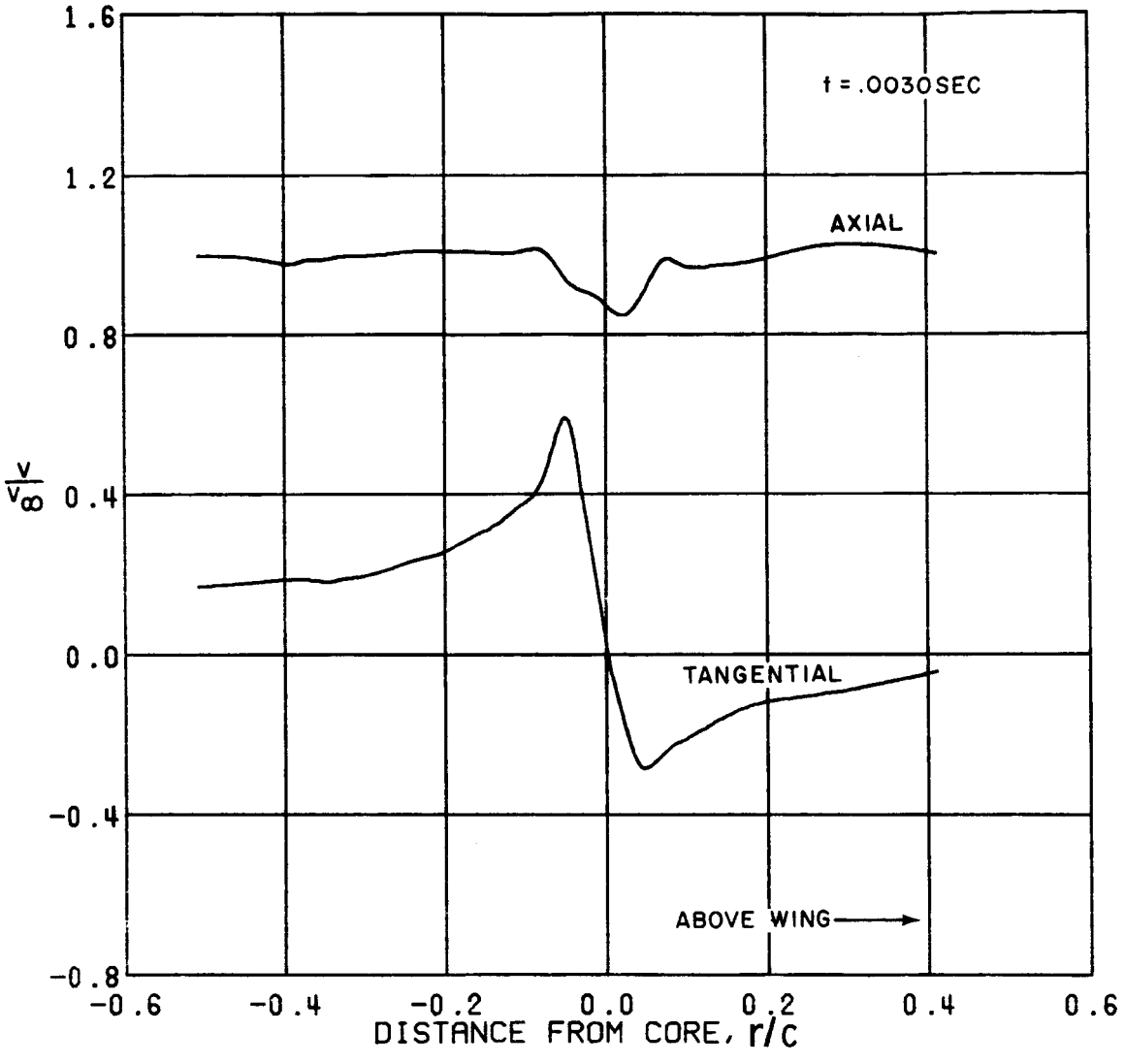

FIGURE 64. SMALL RECT.TIP, VORTEX VELOCITY DISTRIBUTIONS

5.0 CHORD LENGTHS FROM TRAILING EDGE
TRAVERSE NORMAL TO SPAN
MACH 0.60 9.0 DEG PITCH
REYNOLDS NUMBER = 1 100 000.
FREE STREAM VELOCITY = 208. M/SEC = 684. FT/SEC

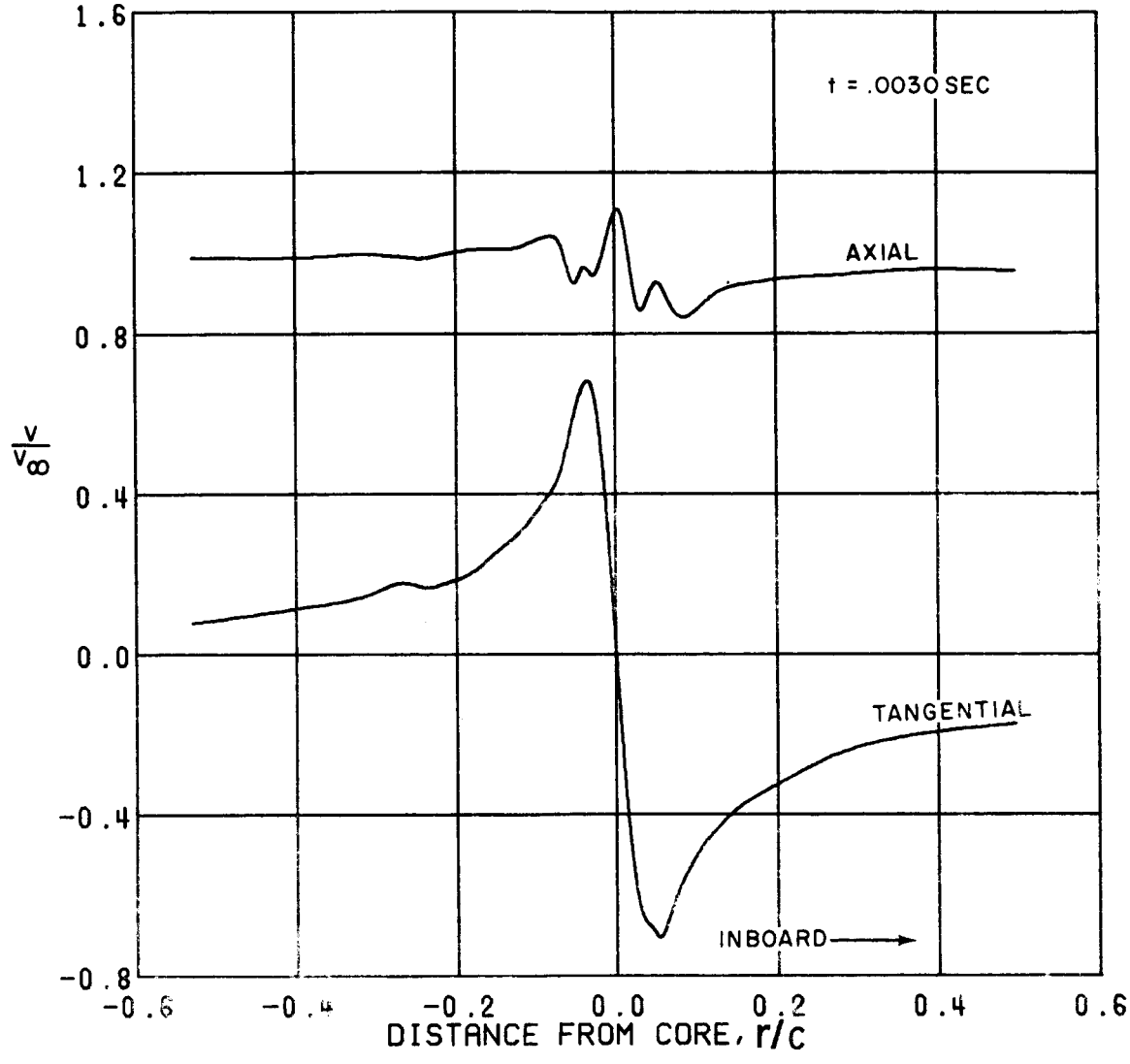

FIGURE 65. SMALL RECT. TIP, VORTEX VELOCITY DISTRIBUTIONS

5.0 CHORD LENGTHS FROM TRAILING EDGE
TRAVERSE PARALLEL TO SPAN
MACH 0.60 9.0 DEG PITCH
REYNOLDS NUMBER = 1 100 000.
FREE STREAM VELOCITY = 203. M/SEC = 667. FT/SEC

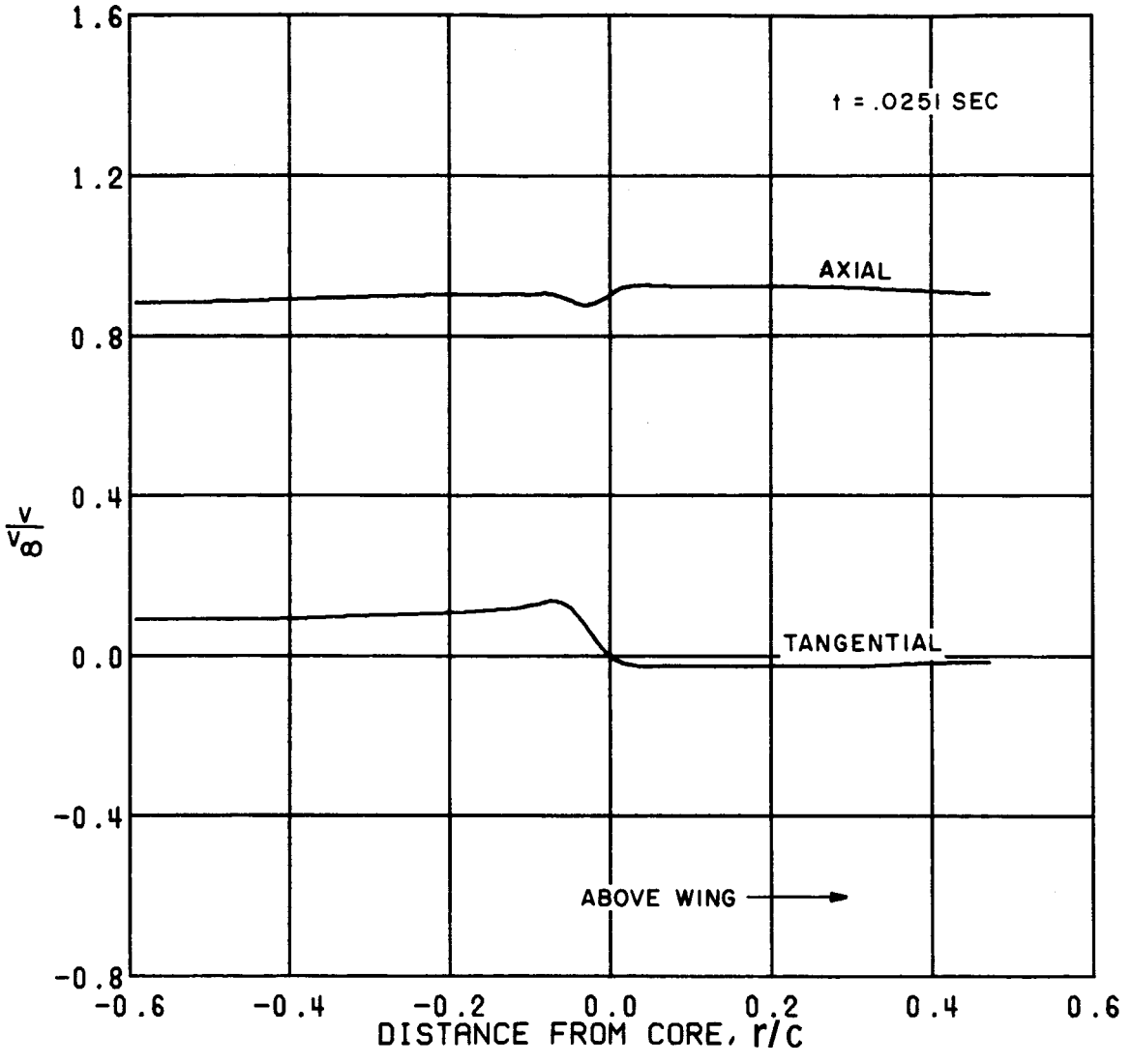

FIGURE 66. REVERSE OGEE TIP, VORTEX VELOCITY DISTRIBUTIONS

2.0 CHORD LENGTHS FROM TRAILING EDGE
TRAVERSE NORMAL TO SPAN
MACH 0.20 6.0 DEG PITCH
REYNOLDS NUMBER = 2 000 000.
FREE STREAM VELOCITY = 73. M/SEC = 238. FT/SEC

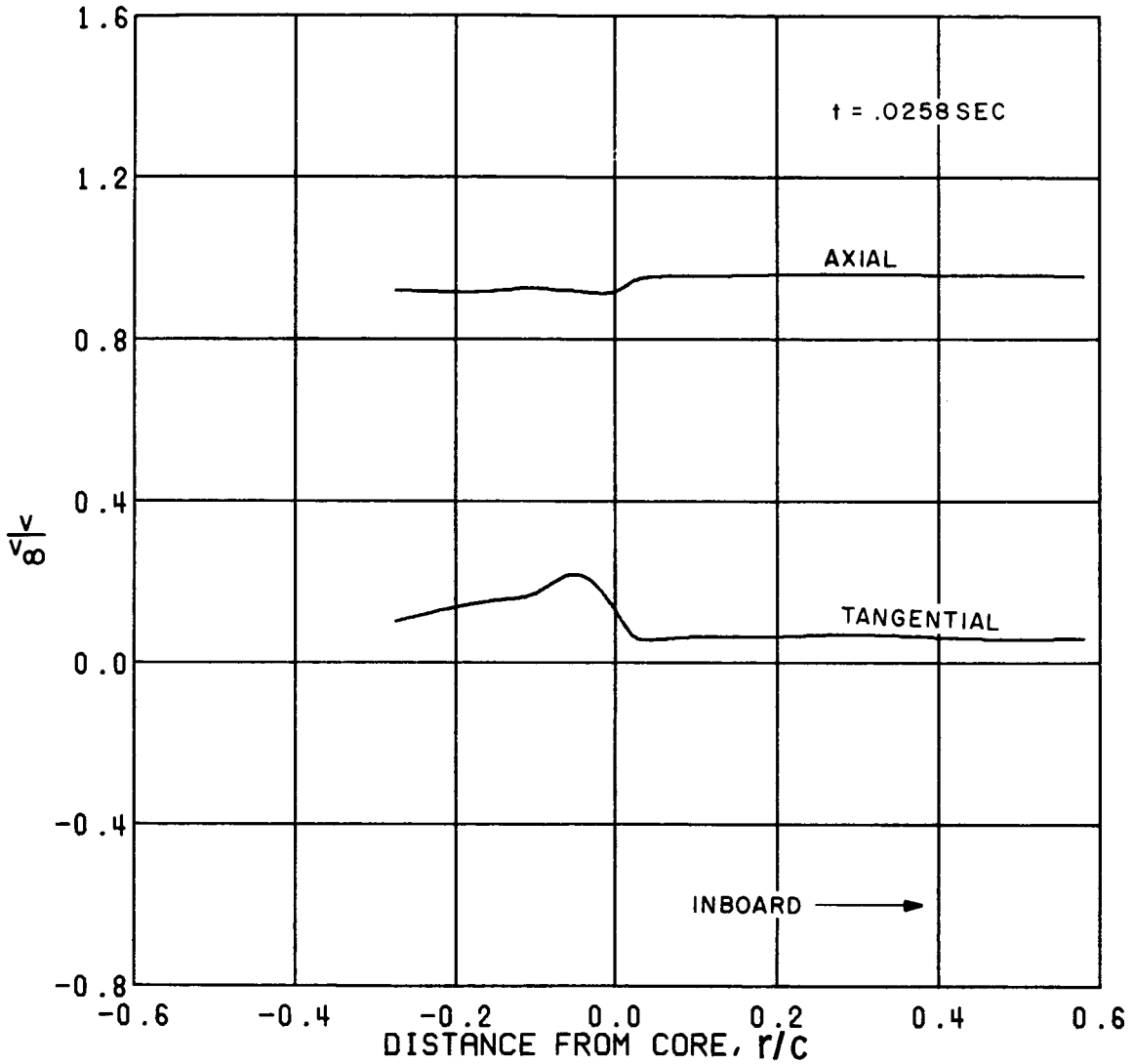

FIGURE 67. REVERSE OGEE TIP, VORTEX VELOCITY DISTRIBUTIONS

2.0 CHORD LENGTHS FROM TRAILING EDGE
TRAVERSE PARALLEL TO SPAN
MACH 0.20 8.0 DEG PITCH
REYNOLDS NUMBER = 2 780 000.
FREE STREAM VELOCITY = 71. M/SEC = 231. FT/SEC

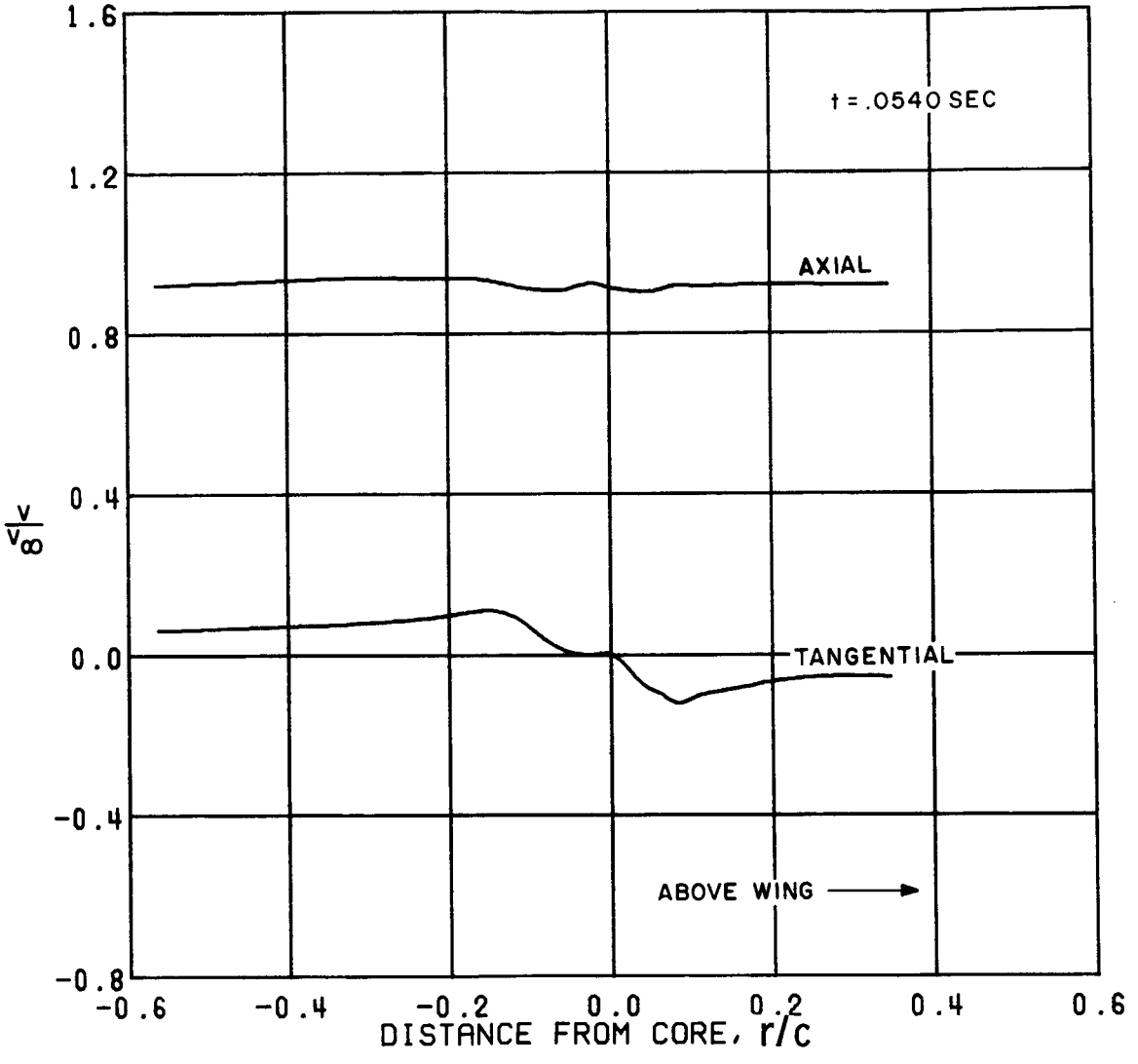

FIGURE 68. REVERSE OGEE TIP, VORTEX VELOCITY DISTRIBUTIONS

5.0 CHORD LENGTHS FROM TRAILING EDGE
TRAVERSE NORMAL TO SPAN
MACH 0.20 6.0 DEG PITCH
REYNOLDS NUMBER = 2 000 000.
FREE STREAM VELOCITY = 72. M/SEC = 235. FT/SEC

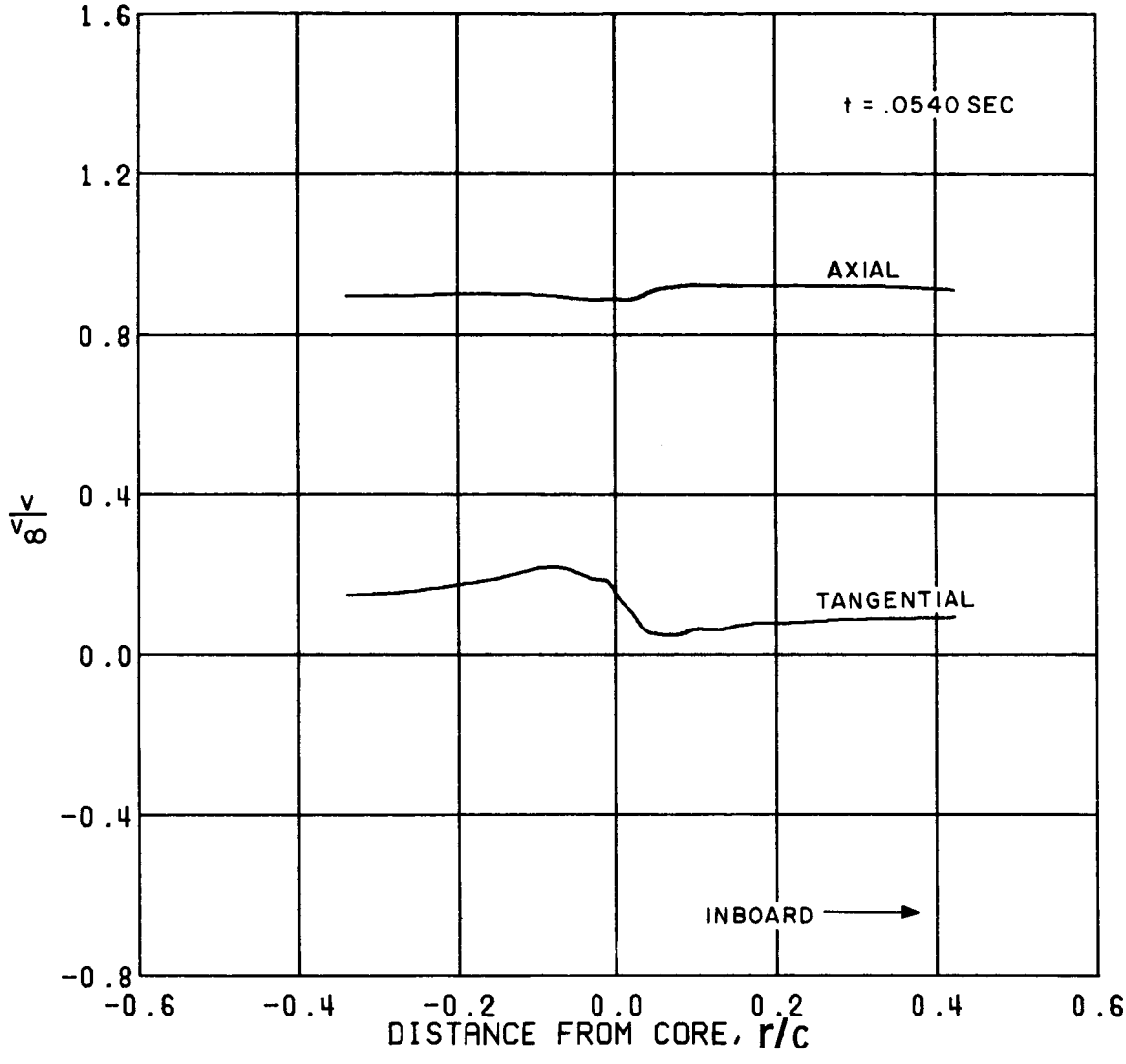

FIGURE 69. REVERSE OGEE TIP, VORTEX VELOCITY DISTRIBUTIONS

5.0 CHORD LENGTHS FROM TRAILING EDGE
TRAVERSE PARALLEL TO SPAN
MACH 0.20 6.0 DEG PITCH
REYNOLDS NUMBER = 2 000 000.
FREE STREAM VELOCITY = 72. M/SEC = 235. FT/SEC

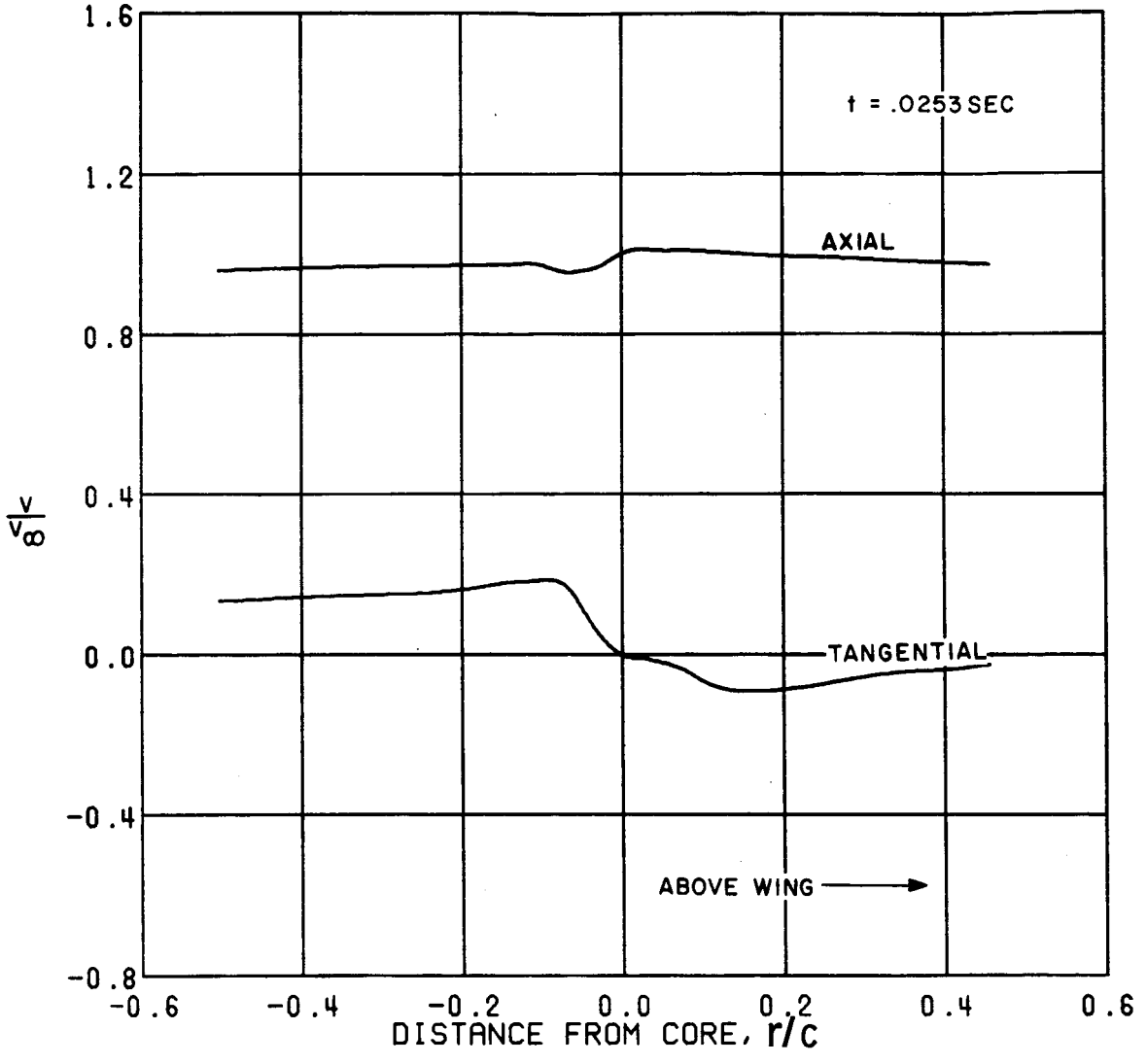

FIGURE 70. REVERSE OGEE TIP, VORTEX VELOCITY DISTRIBUTIONS

2.0 CHORD LENGTHS FROM TRAILING EDGE
TRAVERSE NORMAL TO SPAN
MACH 0.20 8.0 DEG PITCH
REYNOLDS NUMBER = 2 000 000.
FREE STREAM VELOCITY = 72. M/SEC = 236. FT/SEC

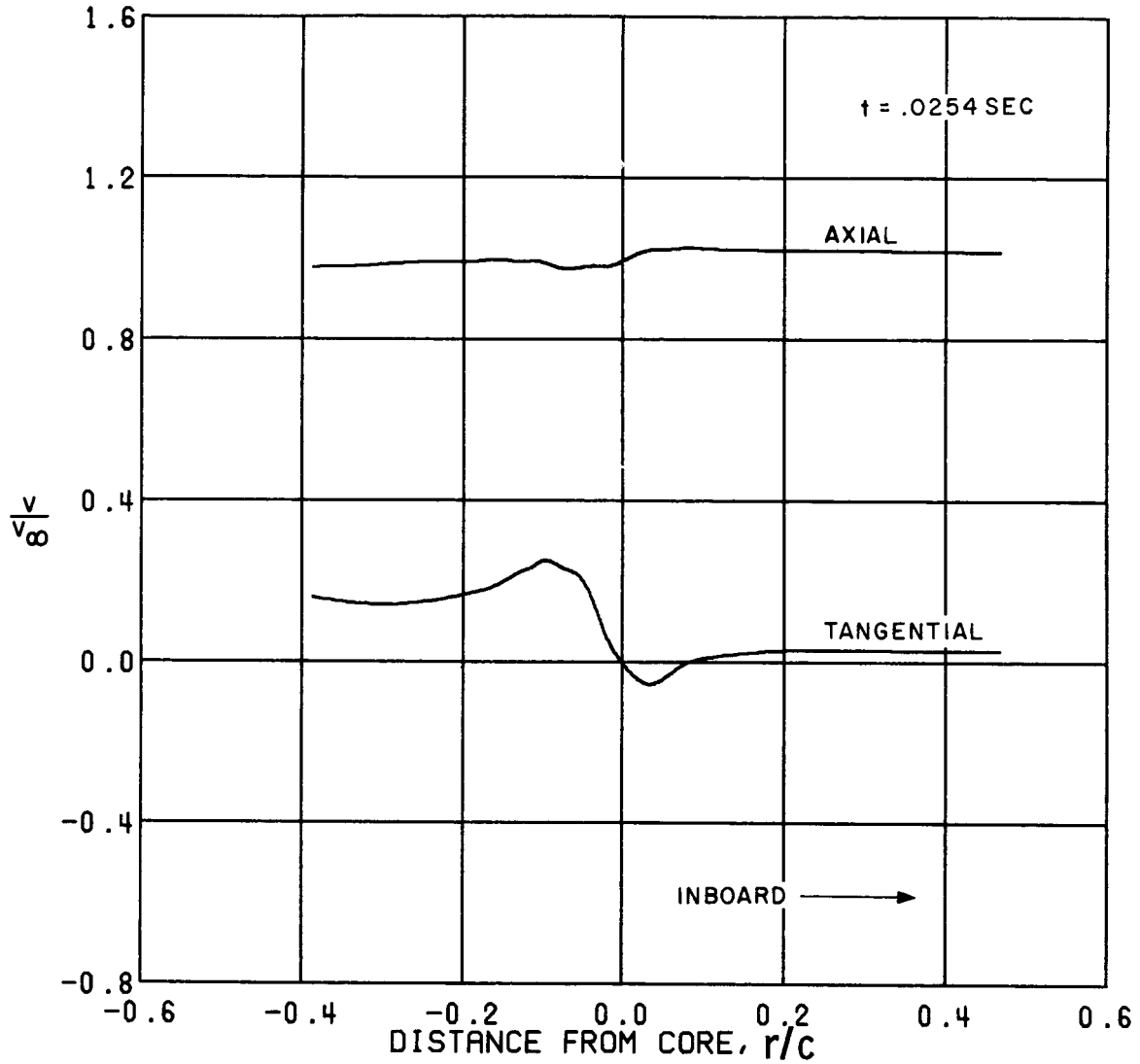

FIGURE 71. REVERSE OGEE TIP, VORTEX VELOCITY DISTRIBUTIONS

2.0 CHORD LENGTHS FROM TRAILING EDGE
TRAVERSE PARALLEL TO SPAN
MACH 0.20 9.0 DEG PITCH
REYNOLDS NUMBER = 2 000 000.
FREE STREAM VELOCITY = 72. M/SEC = 235. FT/SEC

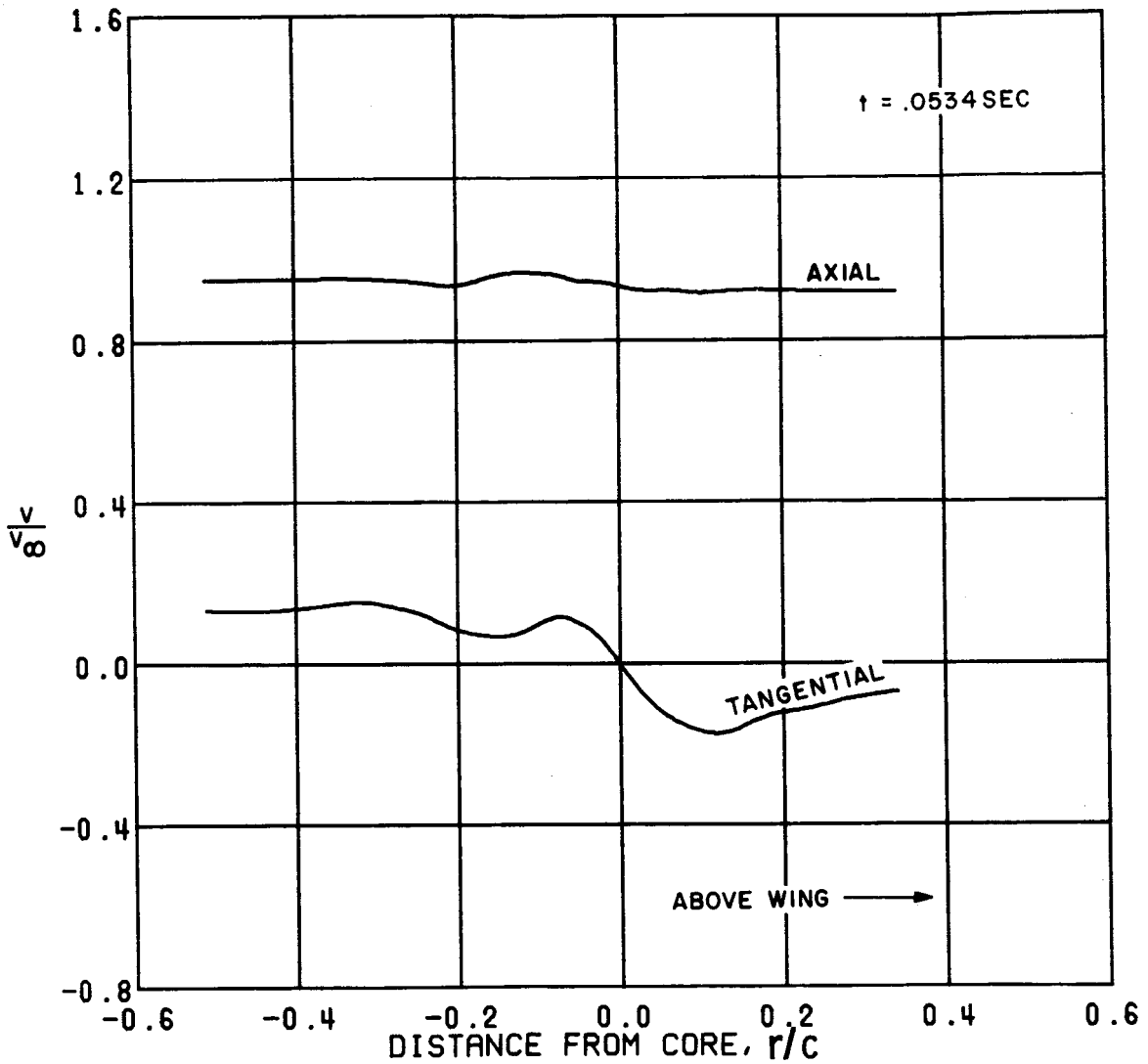

FIGURE 72. REVERSE OGEE TIP, VORTEX VELOCITY DISTRIBUTIONS

9.0 CHORD LENGTHS FROM TRAILING EDGE
TRAVERSE NORMAL TO SPAN
MACH 0.28 9.0 DEG PITCH
REYNOLDS NUMBER = 2 000 000.
FREE STREAM VELOCITY = 71. M/SEC = 234. FT/SEC

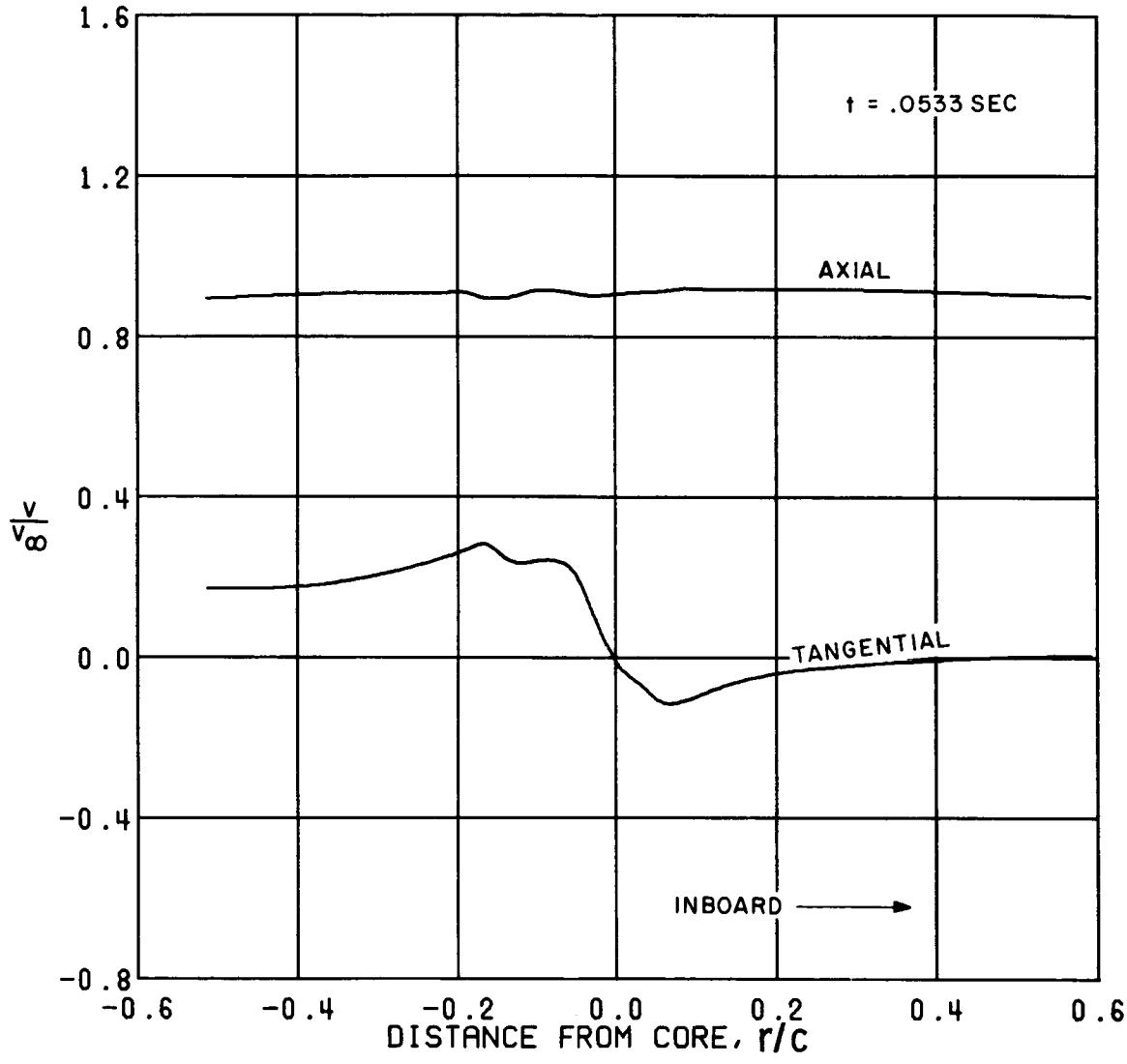

FIGURE 73. REVERSE OGEE TIP, VORTEX VELOCITY DISTRIBUTIONS

5.0 CHORD LENGTHS FROM TRAILING EDGE
TRAVERSE PARALLEL TO SPAN
MACH 0.20 9.0 DEG PITCH
REYNOLDS NUMBER = 2 000 000.
FREE STREAM VELOCITY = 71. M/SEC = 234. FT/SEC

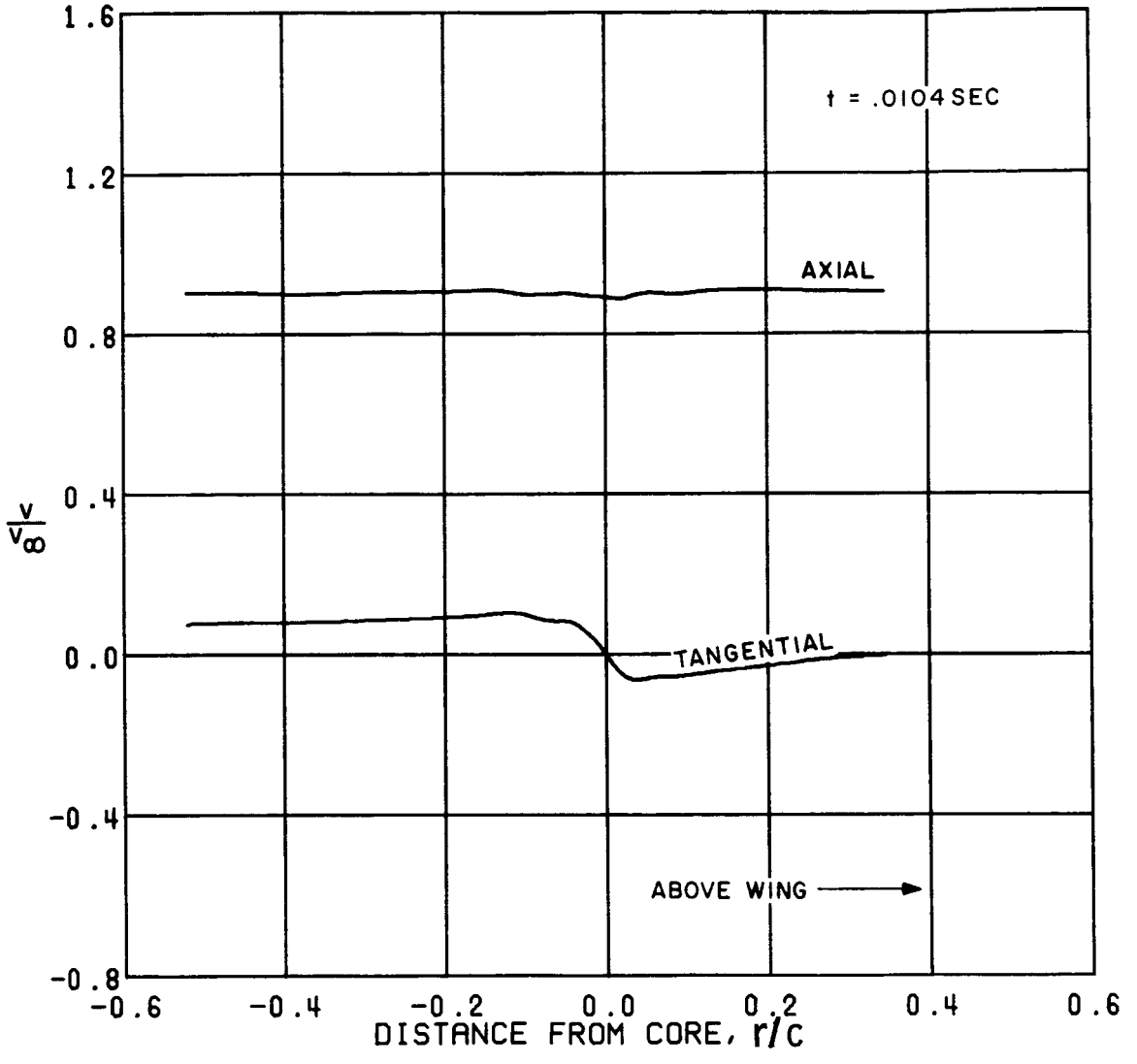

FIGURE 74. REVERSE OGEE TIP, VORTEX VELOCITY DISTRIBUTIONS

2.0 CHORD LENGTHS FROM TRAILING EDGE
TRAVERSE NORMAL TO SPAN
MACH 0.60 6.0 DEG PITCH
REYNOLDS NUMBER = 6 000 000.
FREE STREAM VELOCITY = 175. M/SEC = 573. FT/SEC

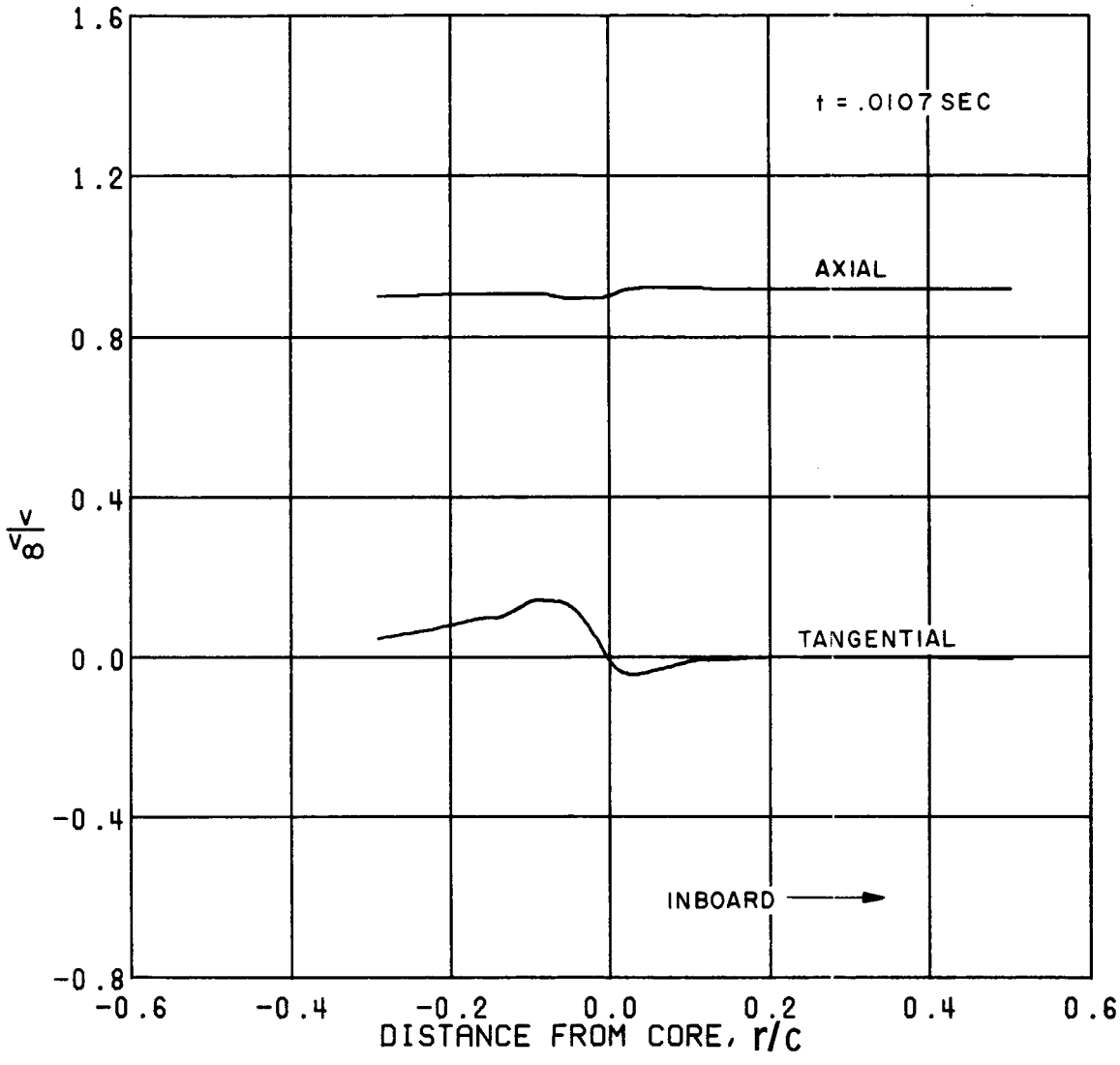

FIGURE 75. REVERSE OGEE TIP, VORTEX VELOCITY DISTRIBUTIONS

2.0 CHORD LENGTHS FROM TRAILING EDGE
TRAVERSE PARALLEL TO SPAN
MACH 0.60 6.0 DEG PITCH
REYNOLDS NUMBER = 6 000 000.
FREE STREAM VELOCITY = 170. M/SEC = 558. FT/SEC

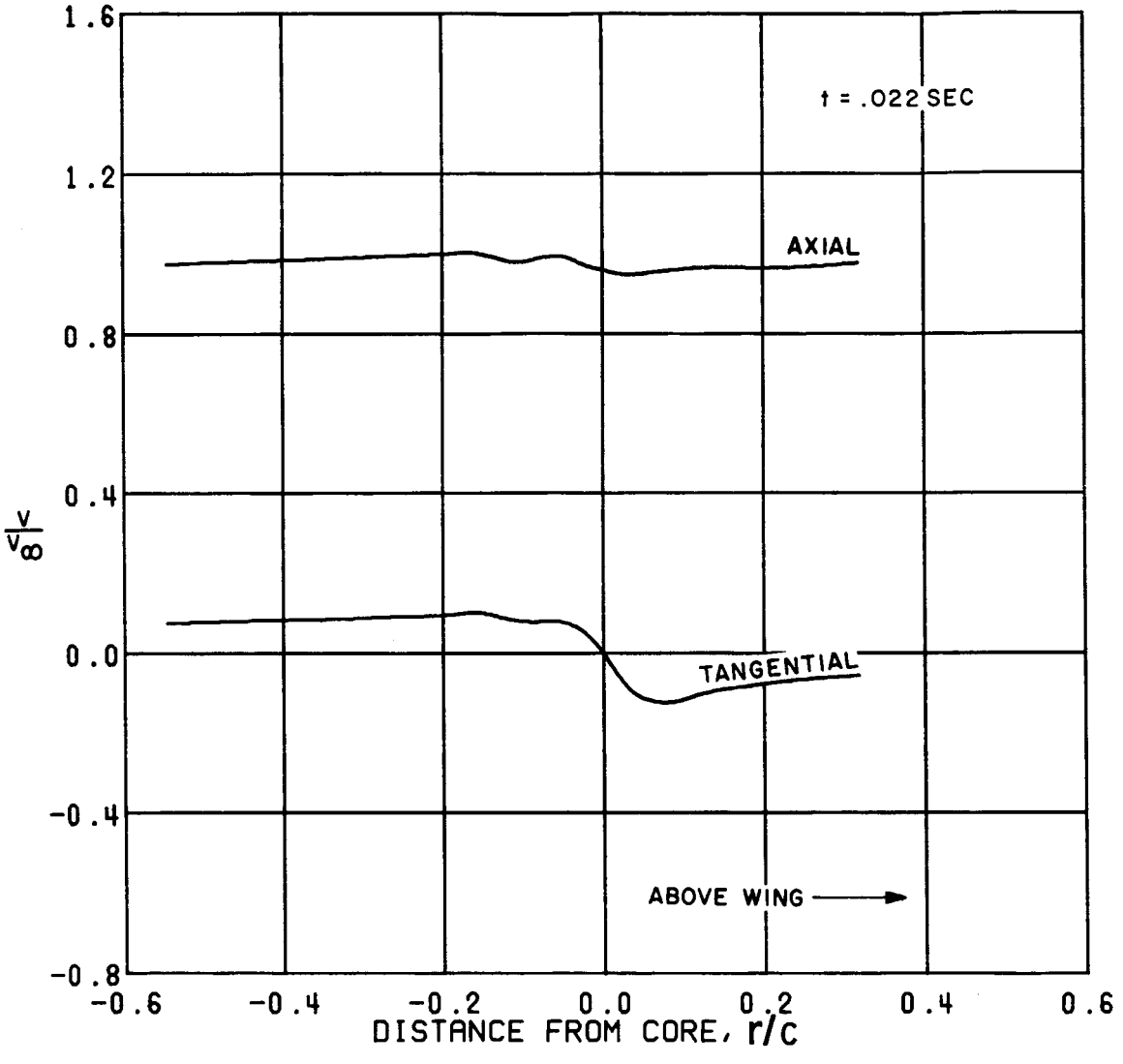

FIGURE 76. REVERSE OGEE TIP, VORTEX VELOCITY DISTRIBUTIONS

5.0 CHORD LENGTHS FROM TRAILING EDGE
TRAVERSE NORMAL TO SPAN
MACH 0.50 6.0 DEG PITCH
REYNOLDS NUMBER = 6 100 000.
FREE STREAM VELOCITY = 173. M/SEC = 567. FT/SEC

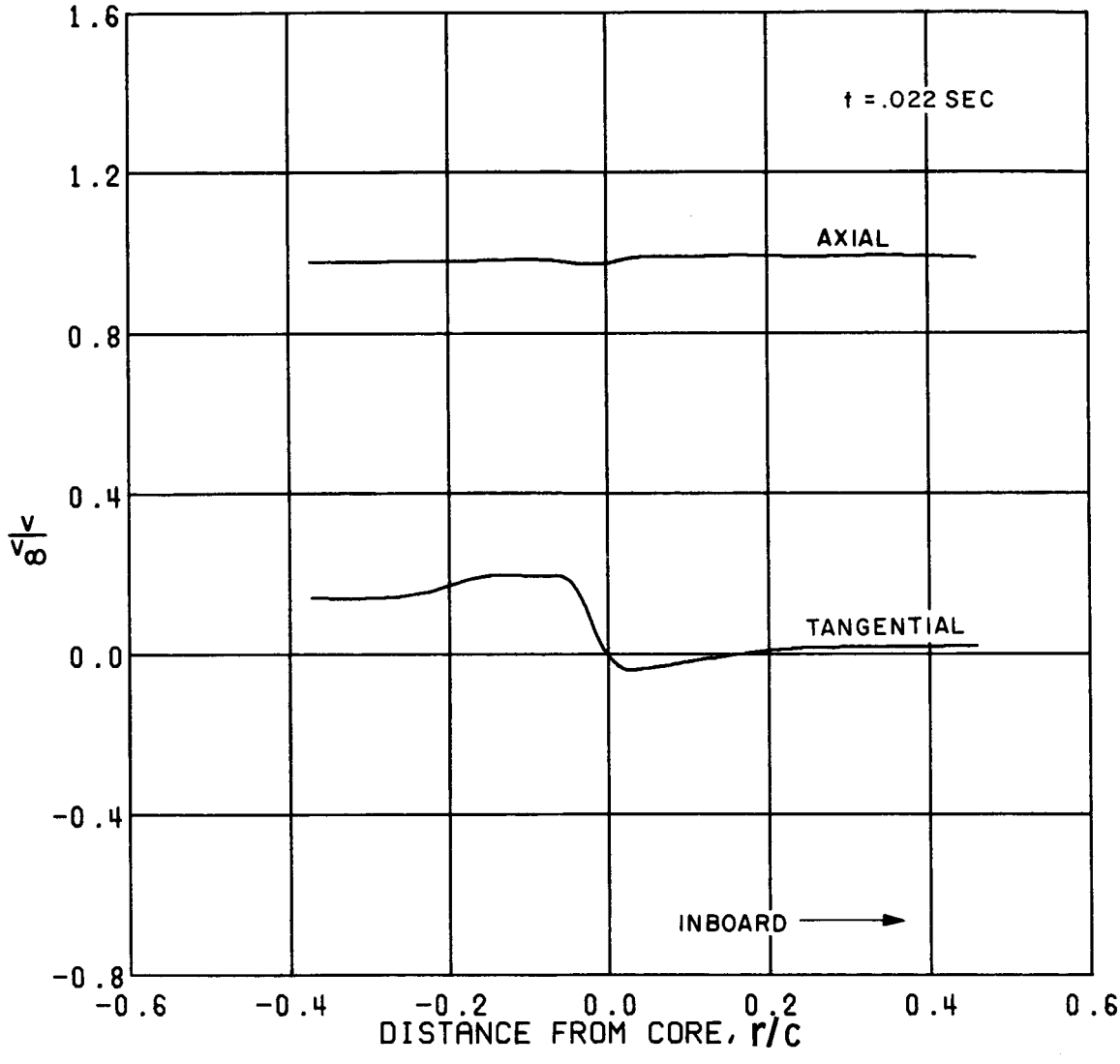

FIGURE 77. REVERSE OGEE TIP, VORTEX VELOCITY DISTRIBUTIONS

5.0 CHORD LENGTHS FROM TRAILING EDGE
TRAVERSE PARALLEL TO SPAN
MACH 0.50 6.0 DEG PITCH
REYNOLDS NUMBER = 6 200 000.
FREE STREAM VELOCITY = 173. M/SEC = 568. FT/SEC

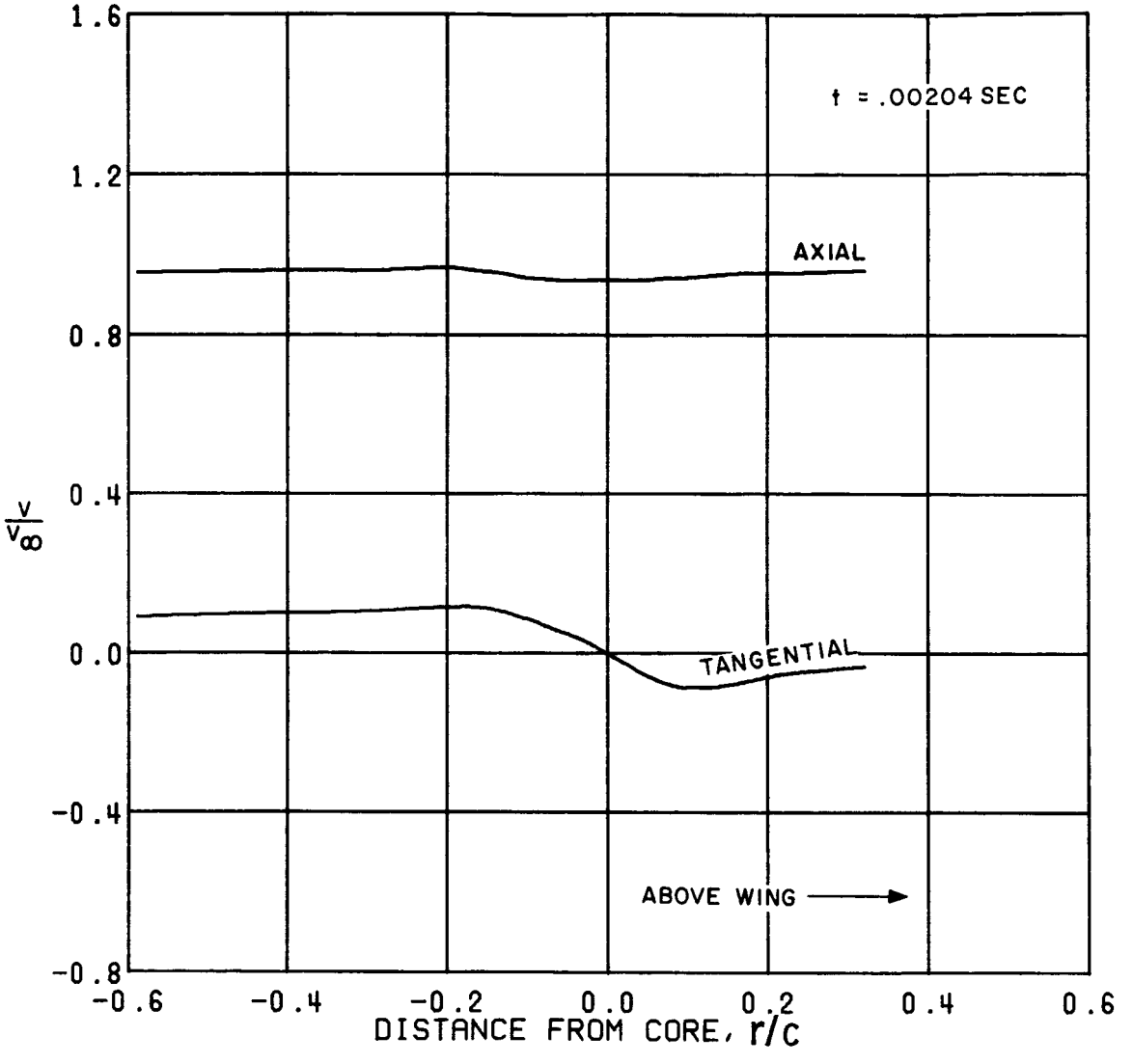

FIGURE 78. REVERSE OGEE TIP, VORTEX VELOCITY DISTRIBUTIONS

2.0 CHORD LENGTHS FROM TRAILING EDGE
TRAVERSE NORMAL TO SPAN
MACH 0.50 8.0 DEG PITCH
REYNOLDS NUMBER = 6 000 000.
FREE STREAM VELOCITY = 176. M/SEC = 578. FT/SEC

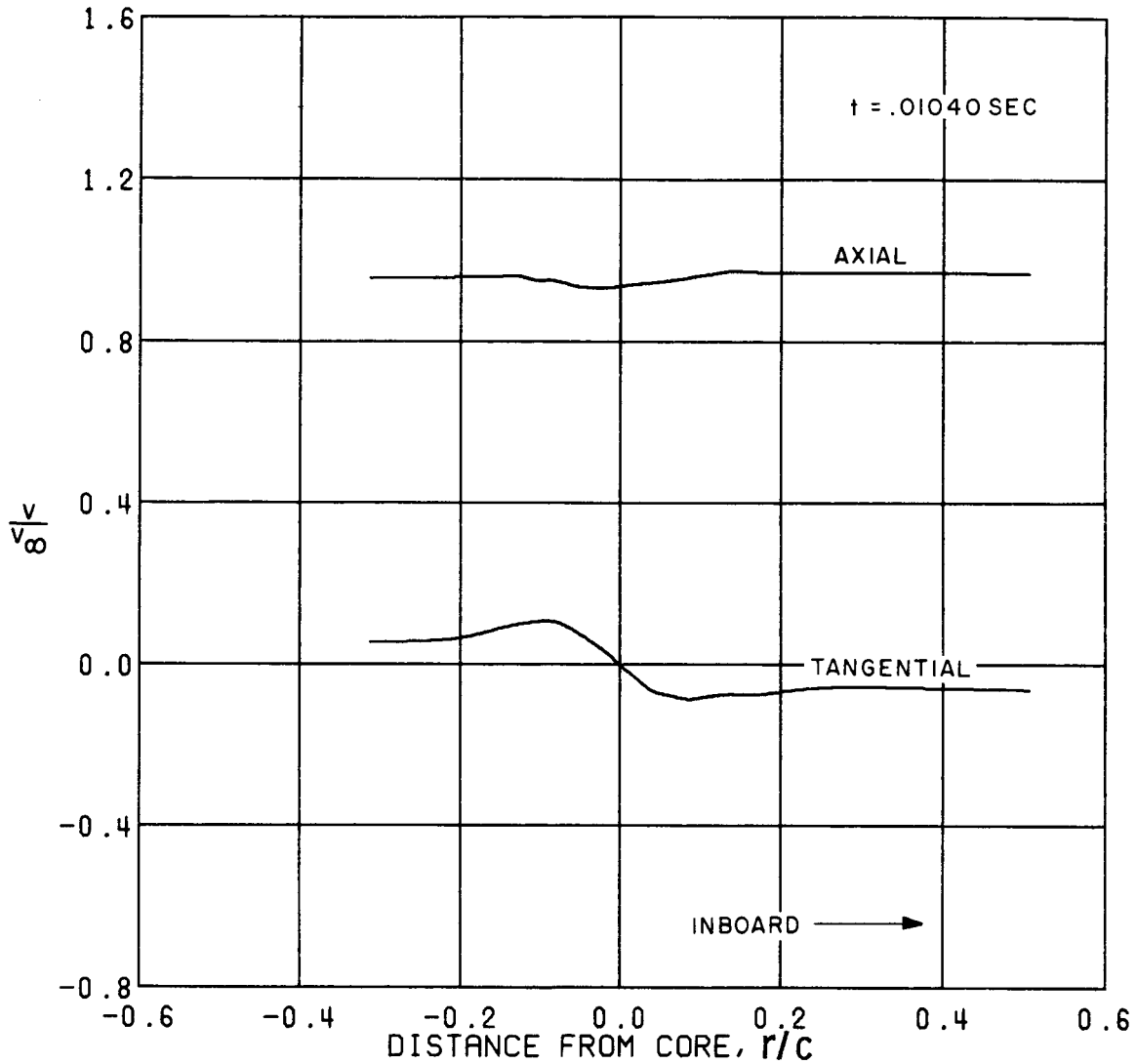

FIGURE 79. REVERSE OGEE TIP, VORTEX VELOCITY DISTRIBUTIONS

2.0 CHORD LENGTHS FROM TRAILING EDGE
TRAVERSE PARALLEL TO SPAN
MACH 0.50 9.0 DEG PITCH
REYNOLDS NUMBER = 6 000 000.
FREE STREAM VELOCITY = 174. M/SEC = 571. FT/SEC

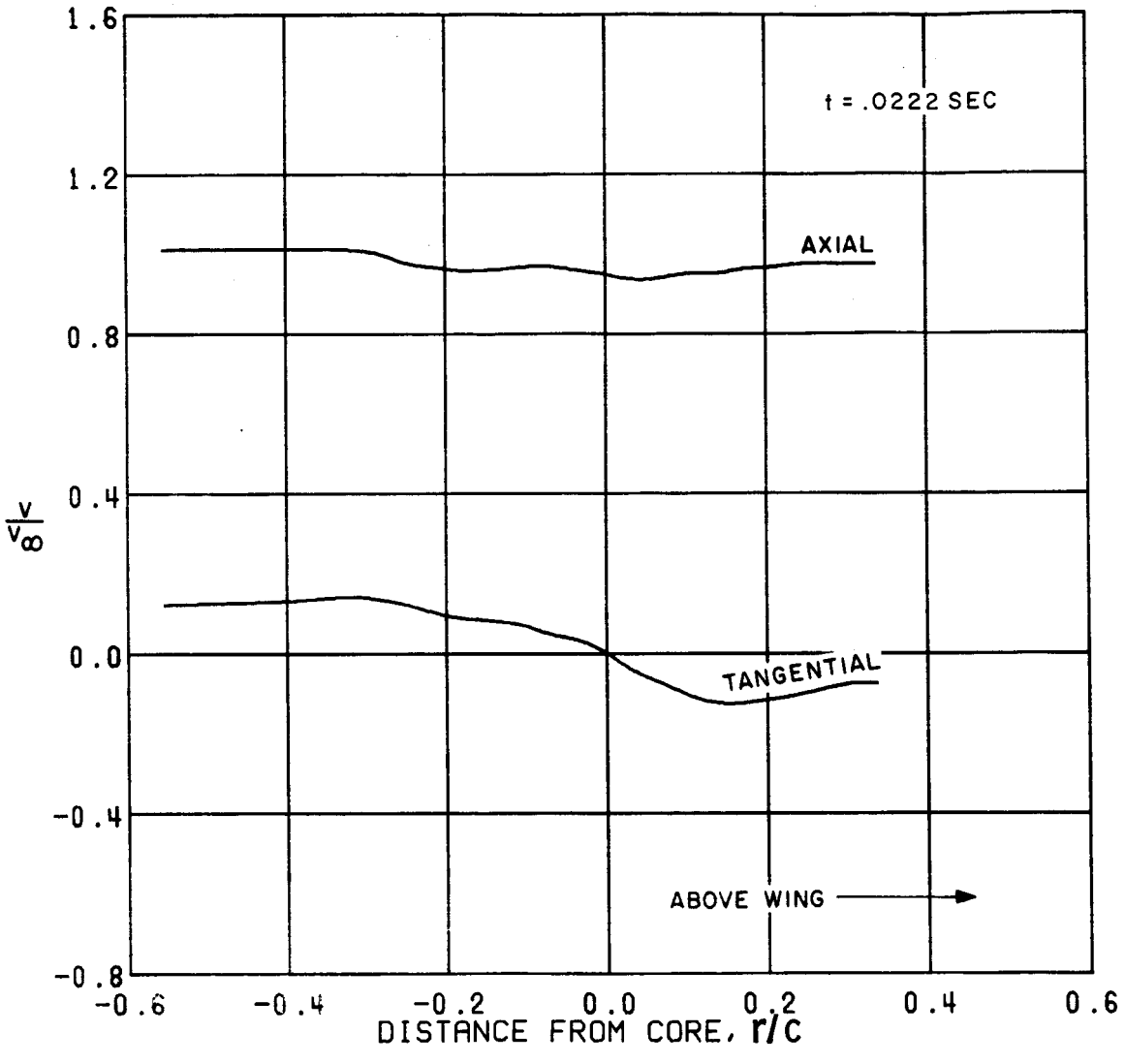

FIGURE 80. REVERSE OGEE TIP, VORTEX VELOCITY DISTRIBUTIONS

8.0 CHORD LENGTHS FROM TRAILING EDGE
TRAVERSE NORMAL TO SPAN
MACH 0.50 8.0 DEG PITCH
REYNOLDS NUMBER = 6 100 000.
FREE STREAM VELOCITY = 172. M/SEC = 564. FT/SEC

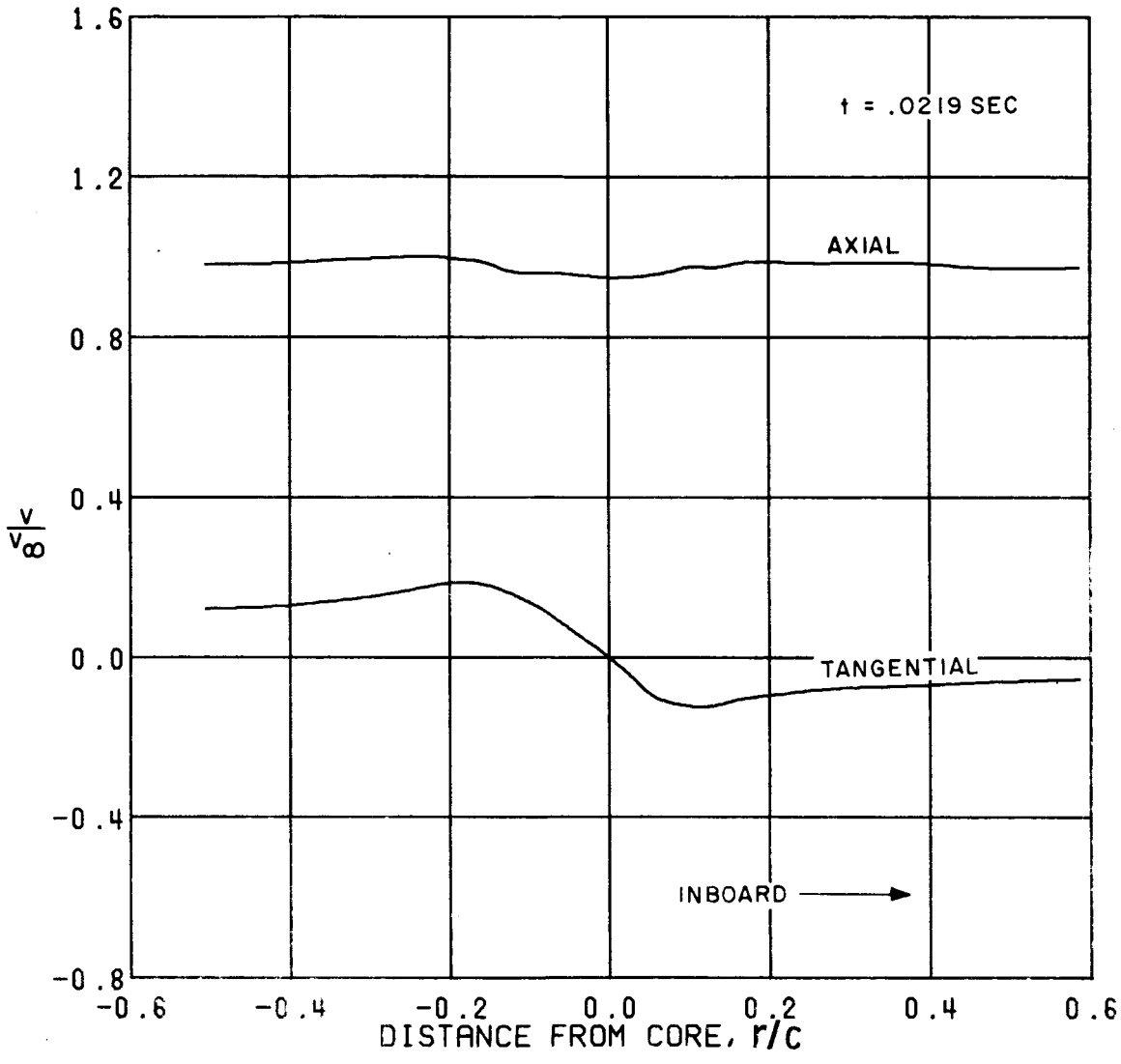

FIGURE 81. REVERSE OGEE TIP, VORTEX VELOCITY DISTRIBUTIONS

5.0 CHORD LENGTHS FROM TRAILING EDGE
TRAVERSE PARALLEL TO SPAN
MACH 0.50 9.0 DEG PITCH
REYNOLDS NUMBER = 6 100 000.
FREE STREAM VELOCITY = 174. M/SEC = 570. FT/SEC

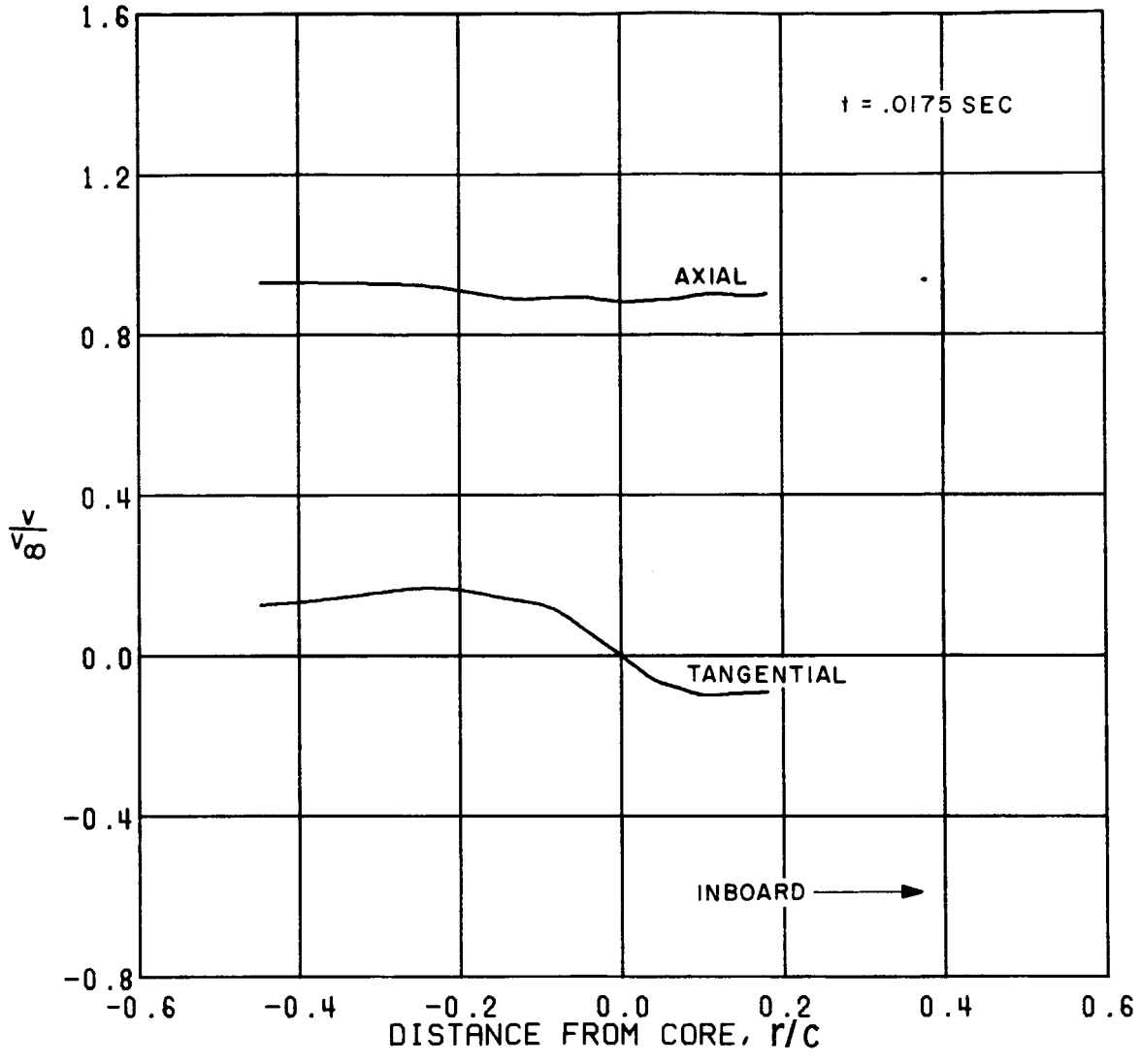

FIGURE 82. REVERSE OGEE TIP, VORTEX VELOCITY DISTRIBUTIONS

5.0 CHORD LENGTHS FROM TRAILING EDGE
TRAVERSE PARALLEL TO SPAN
MACH 0.60 9.0 DEG PITCH
REYNOLDS NUMBER = 7 100 000.
FREE STREAM VELOCITY = 218. M/SEC = 714. FT/SEC

☆ U. S. GOVERNMENT PRINTING OFFICE: 1973—736-352